Master's thesis

NTNU
Norwegian University of Science and Technology
Faculty of Natural Sciences
Department of Materials Science and Engineering

Sebastian Sakshaug Angelsen

Effect of alkaline ionomer on oxygen-reduction and evolution on electrodes

Master's thesis in Chemical Engineering and Biotechnology
Supervisor: Svein Sunde
Co-supervisor: Thulile Khoza
June 2023

NTNU
Norwegian University of
Science and Technology

Sebastian Sakshaug Angelsen

Effect of alkaline ionomer on oxygen-reduction and evolution on electrodes

Master's thesis in Chemical Engineering and Biotechnology
Supervisor: Svein Sunde
Co-supervisor: Thulile Khoza
June 2023

Norwegian University of Science and Technology
Faculty of Natural Sciences
Department of Materials Science and Engineering

NTNU
Norwegian University of
Science and Technology

Preface

This master's thesis was written during the spring semester of 2023 as a part of the course TMT4900 materials chemistry and energy technology. The thesis is the final examination of the 5 years master's degree program Chemical Engineering and Biotechnology (MTKJ) at the Norwegian University of Science and Technology. This project was created by NTNU and SINTEF as a part of the CHANNEL project which is funded by the European Union's Horizon 2020 program.

I would like to thank my supervisor Svein Sunde and co-supervisor Thulile Khoza for their guidance and expertise. In addition, I would also like to extend my thanks to Magdalena Müller for her assistance in both the experimental work and the writing process. Furthermore, I would like to show my gratitude to the electrochemistry group. A huge thanks to all my fellow students at chemistry building 2, especially "Mattek gang". I would also like to thank Rebecca and my family for all the support and motivation.

Abstract

There is a growing global initiative to enhance the utilization of renewable energy sources, with water electrolysis emerging as a promising solution for effectively harnessing excess renewable energy by producing green hydrogen. Among the various types of electrolyzers, anion exchange membrane water electrolyzer stands out for its potential to offer a combination of high efficiency and low cost. However, this relatively new technology faces certain challenges, such as unsatisfactory performance of the solid electrolyte, ionomer, which necessitates the use of an alkaline electrolyte feed. The aim of this thesis is therefore to investigate if reactants and products are able to diffuse through the ionomer and if it conducts hydroxide ions efficiently. This enables us to study whether the electrochemical reactions occur through the ionomer or if the ionomer inhibits the reactions. To achieve this, we conducted oxygen reduction reaction at ionomer-covered platinum rotating disk electrodes. Furthermore, the effect of two different ionomer contents was tested in a real anion exchange membrane water electrolyzer. The morphology of the catalyst layers utilized in the electrolyzer was analyzed by scanning electron microscopy and mercury porosimetry.

It was found that the ionomer is able to diffuse reactants and products through it, but at a low rate. This indicates that the electrochemical reactions occur more efficiently at active sites outside the ionomer. Furthermore, it was observed that a lower ionomer content outperformed a higher ionomer content (10 wt% versus 20 wt%) in the actual electrolyzer cell. A reason for this is due to the ionomer not being able to conduct hydroxide ions efficiently. However, the higher ionomer content showed more promising durability. From these findings, one can assume that the ionomer conducts hydroxides, but not efficient enough to be considered as a stand-alone electrolyte. The electrochemical reactions are therefore occurring at a faster rate at active sites outside the ionomer, while the ionomer works as a binder to enhance the durability of the electrolyzer.

Sammendrag

Det er et økende global initiativ for å forbedre utnyttelsen av fornybare energikilder, hvor vannelektrolyse fremstår som en lovende løsning for effektiv utnyttelse av overskudds fornybar energi ved å produsere grønn hydrogen. Blant de ulike typene elektrolysører skiller vannelektrolysør med anion utvekslingsmembran seg ut for sitt potentiale til å tilby en kombinasjon av høy effektivitet og lav kostnad. Imidlertid står denne relativt nye teknologien ovenfor visse utfordringer, som for eksempel utilfredsstillende ytelse av den faste elektrolytten, ionomer, noe som krever tilførsel av en alkalisk elektrolytt i tillegg. Målet med dette prosjektet er derfor å undersøke om reaktanter og produkter kan diffundere gjennom ionomeren og om den effektivt leder hydroksidioner. Dette gjør det mulig for oss å undersøke om de elektrokjemiske reaksjonene skjer gjennom ionomeren, eller om ionomeren hemmer reaksjonene. For å undersøke dette utførte vi en reduksjonsreaksjon av oksygen ved platina roterende disk-elektroder belagt med ionomer. Videre ble effekten av to forskjellige ionomerinnhold testet i en anion utvekslingsmembran vannelektrolysør. Morfologien til katalysatorlagene som ble brukt i elektrolysøren ble analysert ved hjelp av elektronmikroskop og kvikksølvporosimetri.

Det ble funnet at ionomeren er i stand til å diffundere reaktanter og produkter, men ved lav hastighet. Dette indikerer at de elektrokjemiske reaksjonene skjer mer effektivt ved aktive områder utenfor ionomeren. Videre ble det observert at et lavere ionomerinnhold presterer bedre enn høyere ionomerinnhold (10 wt% versus 20 wt%) i den faktiske elektrolysecellen. Imidlertid viste det seg at et høyere ionomerinnhold hadde en mer lovende holdbarhet. Basert på disse funnene kan man anta at ionomeren leder hydroksid-ioner, men ikke effektivt nok til å betraktes som en selvstendig elektrolytt. De elektrokjemiske reaksjonene antas derfor å skje mer effektivt på aktive områder utenfor ionomeren, mens ionomeren fungerer som en bindemiddel for å forbedre holdbarheten til elektrolysøren.

Abbreviation

Abbreviation	Description
AC	Alternating current
AEMWE	Anion exchange membrane water electrolysis
AWE	Alkaline water electrolysis
BSE	Back-scattered electrons
CCM	Catalyst coated membrane
CPE	Constant phase element
CCS	Catalyst coated substrate
CV	Cyclic voltammetry
DI	Deionized
DMSO	Dimetyl sulfoxide
ECSA	Electrochemical surface area
EIS	Electrochemical impedance spectroscopy
GDL	Gas diffusion layer
HER	Hydrogen evolution reaction
IPA	2-propanol
LSV	Linear sweep voltammetry
MEA	Membrane electrode assembly
OER	Oxygen evolution reaction
ORR	Oxygen reduction reaction
PEMWE	Proton exchange membrane water electrolysis
PGM	Platinum group metal
PTL	Porous transport layer
SE	Secondary electrons
SEM	Scanning electron microscopy
TPB	Triple phase boundary
WE	Water electrolysis

Nomenclature

Variable	Description	Unit
η	overpotential	V
a	charge transfer coefficient	-
b	Tafel slope	V dec^{-1}
i	current density	Acm^{-2}
E_0	starting potential	V
υ	scan rate	Vs^{-1}
t	time	s
i_L	current density	Acm^{-2}
n	number of electrons	-
A	area	cm^2
D	diffusion constant	m^2s^{-1}
ν	kinematic viscosity	m^2s^{-1}
C	concentration	mol dm^{-3}
ω	angular rotation	$rads^{-1}$
f	rotation rate	rpm
i_k	kinetic current	Acm^{-2}
F	Faradays constant	C mol^{-1}
γ	partition coefficient	-
r	reaction rate	mol $m^{-2}s^{-1}$
R	resistance	Ω
Z	impedance	Ω
j	imaginary number	$\sqrt{-1}$
Y	capacitance for CPE	F s
n	deviation from ideal behavior	-
θ	angle	degrees
D	pore diameter	m
ζ	surface tension	N/m
P	pressure	bar
a	activity	-
z	charge number	-
μ	ionic strength	mol m^{-3}
$\gamma_\pm$	mean ionic activity coefficient	-

Contents

List of Figures

List of Tables

1 Introduction

In the present era, there is a growing global focus on achieving a more environmentally friendly and sustainable future. A key aspect of this endeavor involves reducing carbon emissions in the transportation and industrial sectors to meet the escalating energy demand [1]. Numerous initiatives worldwide are focused on increasing the utilization of renewable energy sources. The European Union Commission has set several climate targets for 2030, including a goal of sourcing at least 32% of energy from renewable sources [2]. As the demand for renewable energy continues to grow, there is a pressing need to effectively utilize excess renewable energy. One promising solution to this challenge is the utilization of electrolysis to produce green hydrogen [3, 4, 5].

Green hydrogen serves as a clean energy carrier, offering the advantages of being non-toxic, non-metallic, and possessing high specific energy. Although various electrolyzers can generate green hydrogen, they differ in terms of cost and efficiency [4, 6]. Among them, the anion exchange membrane water electrolyzer (AEMWE) stands out as a promising option, offering a combination of low cost and high efficiency. This relatively new technology capitalizes on the advantages of two more established electrolyzers, the proton exchange membrane water electrolyzer (PEMWE) and the alkaline water electrolyzer (AWE). The AEMWE integrates the compact stack design and high efficiency of the PEMWE, along with the cost-effective materials of the AWE [5]. Figure 1.1 depicts how excess energy generated from renewable sources such as solar cells and wind turbines powers an electrolyzer to produce hydrogen fuel.

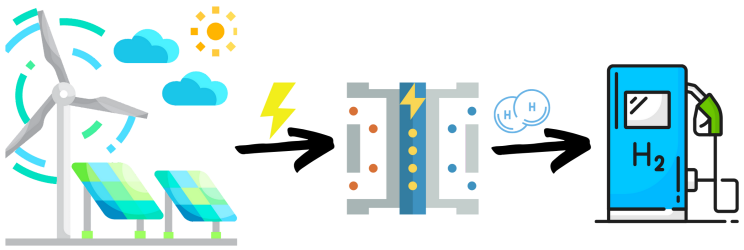

Figure 1.1: Illustration of green hydrogen fuel which originates from electrolysis of water powered by excess renewable energy.

The AEMWE consists of a membrane electrode assembly that can compare to a sandwich consisting of an anode and a cathode at either side of an anion exchange membrane in the middle [1]. Current efforts to improve the overall performance of AEMWE focus on different components of the cell and includes e.g. stability-related issues of the anion exchange membrane, catalyst development, or investigation of the structure within the catalytic

layer. The catalyst layers contain catalyst particles mixed with an anion-conducting polymeric binder, the ionomer. The ionomer therefore serves as a solid electrolyte within the catalytic layer. Besides conducting OH^-, it should be permeable to gaseous products and obtain good swelling properties [7, 8]. In PEMWE, this purpose is fully fulfilled by the well-studied proton conducting material Nafion. PEMWE is therefore fed with ultrapure water. In AEMWE, however, alkaline solutions are still required to achieve satisfactory performance [9]. This raises the question of what role the anion-conducting ionomer serves within the catalytic layer.

This thesis therefore aims to understand the issues related to the ionomer within the catalytic layer of an AEMWE cell by investigating the following research question:

1. Are reactants and products able to diffuse through the ionomer?
2. Does the ionomer conduct hydroxide ions efficiently?

By doing so, we can investigate whether the electrochemical reactions can occur through the ionomer. If so, the ionomer should be able to work as an electrolyte and the reactions should be able to occur without additional KOH electrolyte in addition to increase the number of active sites. If the ionomer inhibits the reactions, it is likely that the reactions occur at active sites without ionomer in the catalytic layer. Figure 1.2 illustrates oxygen reaction occurring through the ionomer and outside it.

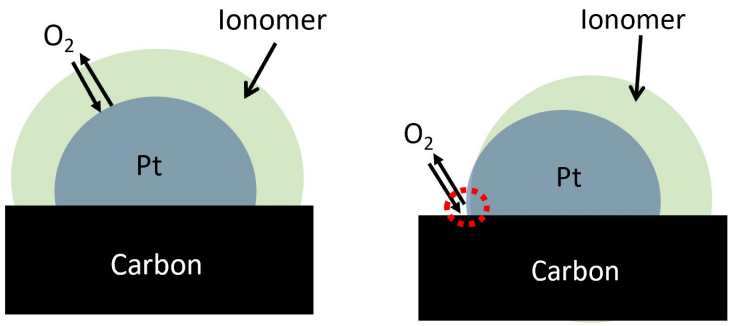

(a) Oxygen reaction occurring through ionomer

(b) Oxygen reaction occurring outside of ionomer

Figure 1.2: Simple sketch of oxygen reaction occurring through the ionomer (a) or outside it (b).

In this work, the reaction kinetics of the ionomer is investigated by performing oxygen reduction reaction as an example reaction at ionomer-covered platinum rotating disk electrodes. Duraion (a polymer containing heterocyclic quaternary ammonium groups provided by Evonik) is used as an exemplary anion-conducting ionomer. Additionally, the effect of the ionomer content on the performance of a real AEMWE cell is investigated at different electrolyte concentrations. The effect the ionomer content has on the morphology of the catalyst layers is also studied by mercury porosimetry and scanning electron microscopy.

2 Theory

The initial part of the theory section provides an overview of low-temperature water electrolysis, followed by a more comprehensive exploration of anion exchange membrane water electrolysis. The emphasis is placed on the catalytic layers, anion conducting polymer, and morphology. Subsequently, the theoretical aspects of electrochemical measurement techniques are explained. Furthermore, a short theoretical segment is included explaining surface characterization methods. Some sections are based on earlier work done by the author (Section 2.1-2.7) [10].

2.1 Water electrolysis

The general term water electrolysis (WE) can shortly be explained as splitting water by applying electricity. The technique was first applied by the English scientists William Nicholson and Anthony Carlisle in 1800. This initiated the start of electrochemistry, but it would take almost a hundred years for WE to be utilized on an industrial scale to produce hydrogen. Norsk Hydro Electrolyzer developed the first alkaline water electrolyser in 1927 to produce hydrogen to use in the synthesis of ammonia [11]. Today, there are several different water electrolysis technologies [11]. Two parameters to consider when classifying WE technologies are the temperature and pH of the electrolyte. The thermodynamic voltage decreases at increasing temperatures. Therefore is it necessary to classify WE electrolyzers at high temperature (T>600°C), medium temperature (200-600°C), and low temperature (T<150°C). The pH dictates the half-cell reactions where hydroxides carry the current in alkaline electrolytes (high pH) and protons in acidic electrolytes (low pH). [12, 11]

Two mature low-temperature water electrolyzer technologies are alkaline water electrolysis (AWE) and proton exchange membrane water electrolysis (PEMWE). AWE operates in alkaline electrolytes while PEMWE operates in an acidic environment [5]. The largest difference between these two technologies is that alkaline is a finite-gap electrolyzer and PEMWE is a zero-gap electrolyzer [5]. A finite gap AWE separates the cathode and anode using a porous diaphragm to hinder recombination of oxygen and hydrogen to water. The porous diaphragm results in a large distance between the anode and cathode. The large distance (>2mm)[1] leads to high ohmic resistance due to the dependency of ionic resistance on the electrolyte thickness. Thereby finite AWE is limited to low current densities. To achieve higher current densities, zero-gap WE has been developed. This is achieved by utilizing thin membranes that can exchange either cations or anions. For PEMWE, a thin proton conductor polymeric membrane (50-200 μm perfluorosulfonic acid membranes) acting as a solid electrolyte, is utilized to achieve a zero-gap cell configuration [1, 13]. Thereby one can utilize a compact stack design. The dense proton exchange membrane enables high-pressure operations and high kinetic activity for the catalysts in

acidic environments. In addition, the membrane ensures high gas purity [14, 15].

Due to the acidic environment for PEMWE, platinum-graded metal (PGM) is needed for the catalyst. This is a problem due to the high prices of scarce PGM, such as platinum and iridium. However, for the alkaline environment for AWE, there is no need for PGMs. AWE can utilize transition metals such as cobalt and nickel [13]. Therefore, a lot of research and effort over the last decade has been made to find a low-temperature WE to utilize the benefits of both AWE and PEMWE. By combining the high efficiency and stack design of PEMWE and the low-cost materials from AWE, anion exchange membrane water electrolysis (AEMWE) has been developed [1]. Table 2.1 gives an overview of the three mentioned low-temperature WEs.

Table 2.1: An overview of some key characteristics for proton exchange membrane water electrolysis, alkaline water electrolysis and anion exchange membrane water electrolysis.

	PEMWE	**AWE**	**AEMWE**
Electrolyte	Proton exchange ionomer [5]	alkaline solution [16]	Anion exchange ionomer + alkaline solution (KOH) [5]
Current density [A/cm^2]	1.0-2.0 [16]	0.2-0.8 [16]	0.2-2 [16]
Temperature [°C]	50-80 [17, 18, 16]	60-90 [5, 16]	40-60 [5, 16]
Pressure [bar]	<70 [5, 18]	1-30 [5, 18]	<35 [5, 18]
Anode	IrO_2 and RuO_2 [5]	Ni and Ni alloys [5]	Ni, Fe and Co [5]
Cathode	PGMs [1]	Ni and Ni alloys [5]	Ni and Ni alloys [5]
Separator	Nafion membrane [1, 5]	diaphragm [1]	AEM [18, 19]
H_2 purity [%]	99.9-99.9999 [16]	99.5-99.9998 [16]	99.9-99.9999 [16]
Lifetime [h]	50 000-80 000 [18, 16]	60 000-80 000 [18, 5, 16]	>30 000 [16]

2.2 Anion exchange membrane water electrolysis

AEMWE capitalizes on the positive aspects of the more mature low-temperature WEs, but there are still some challenges to solve before the WE can be utilized on an industrial scale. AEMWE has a lower electrochemical efficiency compared to PEMWE. This is due to PEMWE using a more efficient cation exchange membrane compared to AEMWEs anion exchange membrane. The ionic conductivity for cation exchange membranes is higher. In addition to the inferior membrane, the hydrogen evolution reaction (HER) is sluggish in a neutral and alkaline environment compared to an acidic one. However compared to AWE, AEMWE is overall more efficient in addition to a more compact design, lower ohmic loss, simpler gas separation, and improved safety. [14, 15]

Figure 2.1 illustrates an AEMWE cell and its main components. The bipolar plates at each end of the cell are made of a corrosion-resistant metal that ensures good electrical conductivity. Usually, the plates are made of titanium, graphite, or nickel [1]. The plate has an in- and outlet to let H_2, O_2 and H_2O (usually accompanied by an alkaline solution) flow through and conduct current [13]. The fluids flow through the plates in microchannels in the plates of various patterns by capillary effect.

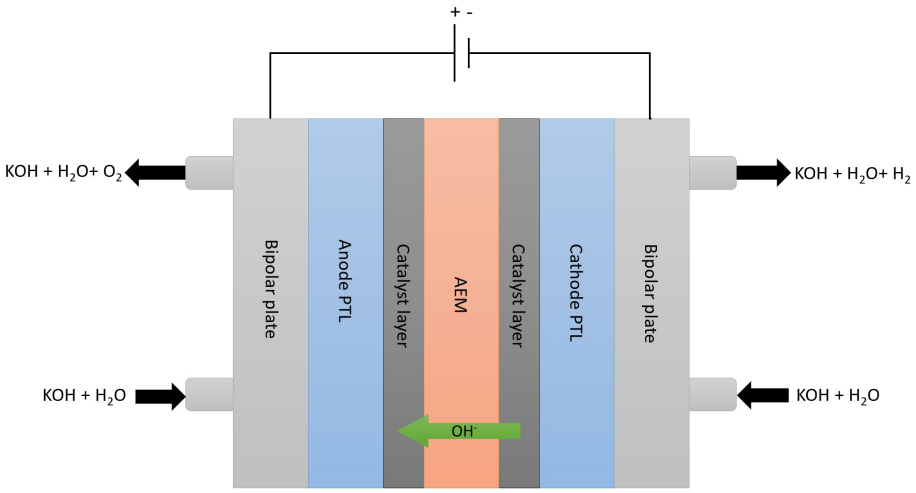

Figure 2.1: Simple illustration of an anion exchange membrane water electrolyzer cell.

In between the bipolar plates is the membrane electrode assembly (MEA) located. The MEA consists of anode- and cathode porous transport layers (PTL), catalyst layers, and an anion exchange membrane (AEM) in the middle. The anode and cathode PTLs provide an electrical connection between the bipolar plates and the MEA. Hydrogen gas diffuses through the cathode PTL and oxygen gas through the anode PTL. This occurs at the same time as electrolyte diffuses in the opposite direction while maintaining a uniform temperature distribution [14]. Due to its porous structure, the PTLs facilitate diffusion of the gaseous products which reduces transport-related overpotentials, thus improving the electrolyzer's performance[20].

The majority of research in improving the performance of AEMWE is focused on the catalyst layers and the AEM. The AEM is made of a polymer backbone with cation sidechains covalently attached [19]. The cation sidechains conducts hydroxide ions through the membrane which is a crucial part of the AEMWE. There are several commercially available AEMs, such as Aemion AEM which is developed from hexamethyl-p-terphenyl poly(benzimidazolium) [19]. The catalyst layers where the water-splitting reactions take place are described in detail in Section 2.5. The reactions that occur in the catalyst layers are given in Equation 2.1 and 2.2. On the right side of the AEM in the cathode catalyst layer seen in Figure 2.1 the following reaction occurs:

$$4\,H_2O + 4\,e^- \longrightarrow 2H_2 + 4\,OH^- \tag{2.1}$$

On the left side of the AEM, where the anode catalyst layer is located, the following reaction takes place:

$$4\,OH^- \longrightarrow O_2 + 2\,H_2O + 4\,e^- \tag{2.2}$$

The reactions and mechanism are further illustrated in Figure 2.2. Hydrogen gas is a product at the cathodic side of the AEM. Electricity is applied to transport the 4 electrons from the anode to the cathode [7].

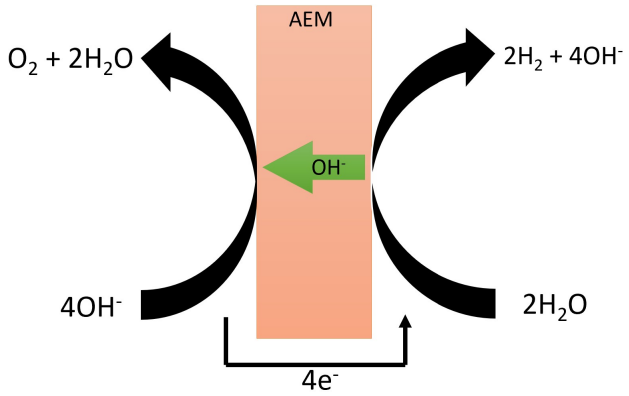

Figure 2.2: Reaction mechanism for an AEM. Anode to the left and cathode to the right. Figure adapted from literature [7]

2.3 Membrane electrode assembly

The MEA is a crucial part of the AEMWE technology in terms of efficiently transporting hydroxide ions (performance) and providing a rigid and sturdy assembly (durability). The main function of the AEM, located in the middle of the AEMWE cell, is to enable ionic transport and inhibit electron- and gas crossover. In addition, the AEM has to be mechanically stable to withstand the compression of the compact design. Ideally, the cost of the AEM is relatively low as well [1, 21]. The AEMs have lower ionic conductivity compared to the proton exchange membranes. This is due to the lower mobility of hydroxide ions compared to protons [22]. One approach to improve ionic conductivity is to incorporate a larger degree of anion exchange groups. However, this could weaken the mechanical strength due to increased swelling and water uptake [13]. Elevated pH and potentials can cause instabilities for the AEM due to the degradation of the ion-exchange group and the polymer backbone. In addition, hydroxide ions and free radicals from oxygen evolution reaction (OER) can attack the cationic groups and polymer backbone which also weakens the stability of the AEMs [22].

There are several configurations of MEAs. The catalyst layer is sandwiched between the AEM and the PTL. The catalyst layer can either be coated onto the PTL (catalyst coated substrate - CCS) or directly onto the membrane (catalyst coated membrane - CCM)

2.3.1 Catalyst coated substrate

For CCS, the catalyst ink is coated on either a PTL or a gas diffusion layer (GDL) substrate. The substrates are easy to coat and control the fabrication of robust and

stable catalyst layers. The substrates enable efficient electron transfer and gas removal. In addition, the substrates works as mechanical support to the catalyst layers. A typical substrate for an AEMWE anode is Ni-felt and carbon paper (Toray paper) for the cathode. [5]

2.3.2 Catalyst coated membrane

There are several advantages for CCMs compared to CCS. Due to the catalyst layers being coated directly on the membrane, CCMs have improved contact between the membrane interface and the catalyst layer. This improves the ionic conductivity due to the lower interfacial contact resistance. As a result of the overall high process efficiency in addition to the effective utilization of the catalyst, there is a lower need for catalysts for CCMs [23]. There are also disadvantages to the intimate contact between the membrane and the catalyst layer. A slightly lower electrical contact with the current collector can be viewed as a trade-off to the improved ionic conductivity of the system as a whole compared to the ionic conductivity of the electrolyte [5]. There are also some concerns of swelling of the membrane that could occur during the coating process. In addition, there are some reported instabilities of the ionomer on the membrane [1]. A possible solution could be a "best of both worlds" hybrid of a CCM cathode and CCS anode. Ito et al. has investigated this hybrid solution [24]. A CCS anode compensates for low cell stability due to delamination of anode catalyst particles when testing CCM configuration using PTFE binder. Ito et al. found that the hybrid solution was effective regardless of type of catalyst [24].

2.4 Electrocatalysts

The objective of a catalyst is to contribute to a reaction by increasing the reaction rate without being consumed in the process [25]. In electrochemical reactions, the rate is increased by lowering the potential of the reaction itself by utilizing other metals or modified surfaces i.e. electrocatalysts. This is especially important for electrochemical reactions that occur at the interface between the electrode material and electrolyte. These reactions usually do not occur close to the thermodynamic potential or at a low rate [26]. An electrocatalyst is heterogeneous and functions across the electrode material. It modifies and increases the reaction rate of the electrochemical reaction. The reaction depends on the temperature, pressure, concentration, etc. [1, 26]

The overall water splitting process which is the objective of the electrocatalysts for alkaline water electrolyzers require a cell voltage of 1.23 V. This is however only a theoretical value. In reality, the reactions require additional overpotentials (η) due to kinetic and ohmic resistance. The reaction mechanism of a catalyst can be evaluated by the Tafel slope given in equation 2.10. The Tafel plot is recorded in the linear portion of voltammograms

at low overpotentials. b is the Tafel slope and i is the current density. Catalysts with a small Tafel slope (b) have a high charge transfer ability due to the Tafel slope being the inverse ratio of the charge transfer coefficient. Ideally, high-performance catalysts for alkaline electrolysis should have a high i and low b. [27]

$$\eta = a + b \cdot log(i) \tag{2.3}$$

The activity of the catalysts can be related to their area. By normalizing the current to the electrochemical surface area (ECSA) is it possible to achieve specific activity which offers an accurate and precise measurement. [27]

2.4.1 Oxygen evolution reaction catalyst

The oxygen evolution reaction (OER) is a sluggish reaction that often leads to high overpotentials [1]. However, OER is faster in alkaline electrolytes compared to the acidic electrolyte used in PEMWE [15]. The reaction is a complex mechanism and is described in equation 2.4-2.7. The mechanism involves 4 charge transfer steps. The species containing (^{ads}) next to it is the absorbed specie on the surface [15].

$$4\,OH^- \rightleftharpoons 3OH^- + e^- + OH^{ads} \tag{2.4}$$

$$OH^{ads} + 3\,OH^- + e^- \rightleftharpoons 2OH^- + e^- + O^{ads} + H_2O \tag{2.5}$$

$$O^{ads} + H_2O + 2\,OH^- + 2\,e^- \rightleftharpoons OH^- + 3\,e^- + OOH^{ads} + H_2O \tag{2.6}$$

$$OOH^{ads} + H_2O + OH^- + 3\,e^- \rightleftharpoons 4e^- + OOH^{ads} + 2\,H_2O + O_2 \tag{2.7}$$

Transition metals such as nickel, cobalt, manganese, and iron are widely employed as OER catalysts due to their favorable activity [28]. Studies have demonstrated that the combination of nickel and iron as a Ni-Fe catalyst exhibits enhanced activity compared to pure nickel catalysts [5]. Ni_2FeB has emerged as a promising candidate for anode OER applications [29]. Borides have demonstrated good performance at high pH, making them well-suited for alkaline electrolysis. This enhanced performance can be attributed to the electronegative nature of boron which facilitates charge transfer and lowers the energy barrier for oxidation reactions. Furthermore, borides possess several advantageous characteristics such as being non-toxic, earth-abundant, stable, ease of preparation, and relatively low energy demand [30].

2.4.2 Hydrogen evolution reaction catalyst

In alkaline electrolytes, HER occurs through several electrochemical reaction steps by adsorption and desorption given in equation 2.8-2.10. The first step is the Volmer reaction

where water is oxidized to hydrogen. The ^{ads} sign next to the hydrogen indicates the adsorbed specie [15].

$$2\,H_2O + 2\,e^- \longrightarrow 2H^{ads} + 2\,OH^- \tag{2.8}$$

Research of alkaline HER has shown an inferior performance compared to acidic HER due to the Volmer step demanding extra energy [27]. Following the Volmer reaction, the adsorbed hydrogen can either bond with another hydrogen from another oxidized water (Heyrovsky reaction 2.9) or bond with another adsorbed hydrogen (Tafel reaction 2.10).

$$H_2O + H^{ads} + e^- \rightleftharpoons H_2 + OH^- \tag{2.9}$$

$$2\,H^{ads} \rightleftharpoons H_2 \tag{2.10}$$

Thereby the general mechanism of alkaline HER is either Volmer-Heyrovsky process or Volmer-Tafel process. [1]

Similar to OER, transition metals are widely utilized as HER catalysts. Earth-abundant transition metals have shown great performance in terms of activity and durability. Nickel-based catalysts are some of the most well-researched catalysts and report low overpotentials and Tafel slopes in addition to high current densities. [1, 15]

2.5 Catalyst layers

The catalyst layers used in electrochemical cells are typically composed of a catalyst powder, such as NiFe, mixed with an anion conducting polymer (ionomer). This mixture is dispersed in appropriate dispersion media to obtain an ink slurry, which can be spray-coated onto a substrate or an AEM. The primary function of the catalyst layer is to provide catalysts that contribute to the electrochemical reactions taking place within the cell. Additionally, the catalyst layer must transport electrons through electronic conducting pathways and maintain a porous structure to allow for the escape of H_2 and O_2 gases. [8]

The design of the catalyst layer has a significant impact on its morphology and composition, ultimately affecting the performance of the cell. The electrochemical reactions occur at active sites called triple-phase boundary (TPB) regions within the catalyst layer, where three phases meet: catalyst particles, electrolyte, and gas pores. The catalyst particle represents the solid phase, while the ionomer electrolyte acts as the conductor, and H_2 and O_2 gases serve as the gaseous phases. The three-dimensional interfaces within the TPBs are critical in determining both the rate and efficiency of the electrolysis process. [8]

The pores within the catalyst layer play a vital role in the transport of reactants and products, while the catalyst particle facilitates optimum reaction kinetics and electron transport. The ionomer electrolyte provides anion transport at the TPBs, as illustrated in Figure 2.3. Overall, the performance of the electrochemical cell is significantly influenced by the design and composition of the catalyst layer. [31, 15]

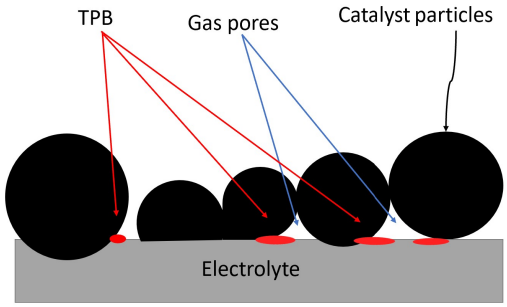

Figure 2.3: Simple sketch of triple phase boundaries in a catalyst layer. Figure adapted from [10].

2.6 Anion conducting polymer

The anion-conducting polymer i.e. ionomer, is a polymeric organic molecule that is mixed in the catalyst ink. The function of the ionomer is to improve the hydroxide conductivity in the catalyst layer/AEM interface in a through-plane direction. The ionomer can thereby extend the TPB region, and by that increase the number of active sites for the catalyst layer. In addition to improving the conductivity, it also works as a binder to stabilize the ink to improve ink uniformity and coating quality. The ionomer transports hydroxide ions between the AEM and the catalytic active sites without blocking them. It is important that the ionomer does not block the active sites to ensure H_2 and O_2 gases easily can escape through a porous catalytic layer. [32, 1]

Ionomers utilized in AEMWE such as Fumion FAA-3 from FumaTech and Aemion from Ionomr Innovations Inc, have quaternary ammonia covalently bonded to the polymer backbone. It is found to be an optimal functional group in terms of chemical- and mechanical stability in addition to good hydroxide conductivity. The quaternary groups are positively charged and therefore conduct hydroxide ions (negatively charged ions), which is an important function of the ionomer [13, 15, 33]. However, research on Pt HER catalyst ionomer interactions has shown that the anion ionomer impacts the activity of the catalyst at high pH. For transporting hydroxide ions in the AEM, the quaternary ammonium functional group poisons the Pt surface which decreases the activity of the catalyst [33].

Durability tests of quaternized biphenylene ionomer and quaternized polyphenylene AEM reports of performance loss due to degradation of the ionomer. The degradation was identified as phenyl oxidation of the ionomer during operation. The oxidation rate was observed as quite high and was likely to occur at the interface between the catalyst and the ionomer (active TPB sites). The oxidated phenyl group, phenol, is quite difficult to remove from the interface due to being covalent bound to the ionomer. The phenol group is acidic, which in return reduces the local pH. Lowering the local pH leads to a decrease in catalyst activity. These results were found using IrO_2 catalysts and it is believed that non-PGM perovskite oxide catalysts such as nickel oxides will perform better due to lower phenyl group absorption. [34]

As mentioned in Section 2.3, the catalyst layers for CCMs have challenges with instability and swelling. The ionomer can stabilize the catalyst layer on the membranes due to it working as a binder in the catalyst ink. By utilizing the binding characteristics of the ionomer, there is a possibility to reinforce the membrane [1, 8]. Vincent et al. studied the effect of different amounts of ionomer content [35]. It was found that too low ionomer loadings lead to the formation of cracks in the catalyst layers. However, too high amounts resulted in voltage drops [35].

Research has shown that there is no standard in terms of ionomer loading in catalyst inks. The optimal amount of ionomer depends on the catalysts and the MEA and is usually found experimentally [13]. A study done by Koch et al. on the morphology of IrO_x anode catalyst layer coated on Aemion$^+$ membrane found that areas containing high amounts of ionomer weakened the homogeneous pore structure [8]. It was found that 7 wt% of ionomer performed the best for the anode catalyst layer in terms of performance and durability [8]. In comparison, Park et al. found the optimal Fumatech FAA-3-Br ionomer content to be at 20 wt% with an IrO_2 anode catalyst and Pt/C cathode catalyst [3].

The dispersion solvent such as DMSO, EtOH, and IPA for the ionomer can have an impact on the structure of the ionomer in the solution due to polarity [36]. This can affect the morphology of the catalyst layer in terms of pore distribution. A study found that the distribution of ionomer lead to a variation in pore structure in which influenced the physical state of the ionomer aggregates. A smaller size of ionomer aggregates resulted in a more uniform distribution of ionomer and a large ECSA. [36]

2.7 Morphology of catalyst layers

The morphology of the catalyst layer plays a role in the performance of the AEMWE. An important part of preparing a catalyst ink is to break up large agglomerates. This is to provide a good homogeneously dispersed catalyst layer on either an electrode or membrane [37]. A well-used and researched HER catalyst, Pt/C, consists of Pt particles supported on carbon blacks. The conductive carbon support facilitates high utilization of active sites [37]. The Pt/C catalyst exhibits two distinct pore distributions: primary pores and secondary pores. The primary pores, approximately 0.1 µm in size are found inside agglomerates between the Pt/C particles, while the secondary pores are larger pores located between the agglomerates [38, 39]. Figure 2.4 provides an illustration of the morphology of a Pt/C catalyst layer.

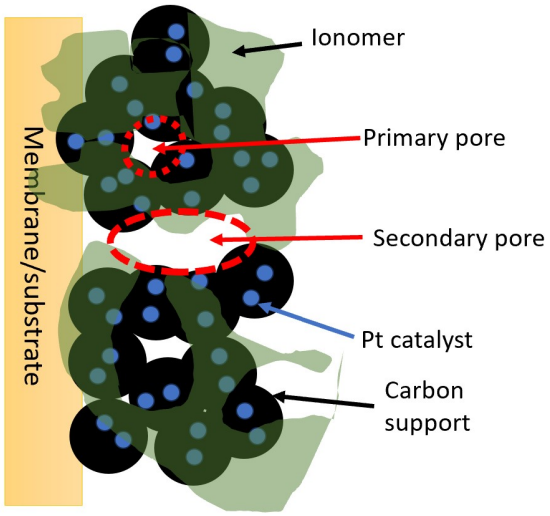

Figure 2.4: Illustration of a porous Pt/C catalyst layer. The black circles are the carbon support and the smaller blue circles are the Pt catalyst particles. The light green mass covering the particles is the ionomer. The secondary pore is located between the agglomerates and the primary pore is located inside the agglomerate between the Pt/C catalysts. Figure inspired by [37]

In a study conducted by Watanabe et al. [40] two crucial structural requirements were identified for a Pt/C catalyst layer. Firstly, it was found that the majority of platinum clusters should be situated within an electrolyte network. Secondly, a fulfilling amount of reactant gas should be efficiently supplied to the clusters via the shortest path [40]. It has been reported that an excessively thick ionomer that forms the electrolyte network, can negatively impact the secondary pores hindering gas transfer and by that increased gas transfer resistance. However, a thick ionomer layer can enhance anion conductivity [41]. Furthermore, a study done by Suzuki et al. [41] found that too high amount of ionomer leads to a filling of secondary pores.

In a study conducted by Min Wang et al. [42] the impact of ultrasonic dispersing of Pt/C agglomerates in catalyst inks was investigates. Insufficient sonication led to the formation of large agglomerates where the ionomer only made contact with the outer surface area. As a result, a significant portion of the active sites, represented by Pt particles, remained unexposed to the ionomer. This led to a decrease in activity and an increase in gas mass transport resistance. However, excessive sonication caused the detachment of Pt particles from the carbon support. To optimize the utilization of the conductive ionomer, it was found a moderate level of sonication was ideal. This effectively broke down the agglomerates to smaller-moderate sized particles allowing the ionomer to access the active sites. Smaller agglomerates exhibited lower gas resistance, as the gases had improved access to the active sites due to fewer secondary pores.

2.8 Electrolyte

The performance of an AEMWE depends on the supporting electrolyte and the operating temperature. High operating temperatures increase the electrode kinetics in addition to facilitating the separation of the oxygen- and hydrogen gases. Ideally, the electrolyzer should be able to work only by feeding it water, but it results in low performance compared to hydroxide solutions such as KOH. The low performance is likely to be a result of inefficient hydroxide ion pathways in the catalyst layer. In addition, there is a possibility for CO_2 contamination from the air in the KOH electrolyte at low concentrations. CO_3^{2-} and HCO_3^- decreases the ionic conductivity of the electrolyzer by contaminating the AEM. [43, 44]

Typically, various concentrations of KOH are used for AEMWE. There are no standards in terms of concentration due to the large variety of materials such as AEM and ionomer. The performance of the electrolyzer increases in relation to the increasing concentration of the KOH electrolyte. This is a result of decreasing polarization resistance for both the cell and electrodes. However, too high concentrations of alkaline electrolytes reduce the durability of the electrolyzer due to the high corrosion rate [15, 5].

As mentioned, using deionized water (DI water) is the preferred option to make it competitive compared to other low-temperature electrolyzers. However, there are challenges due to nickel-based catalysts having low OER and HER activity in neutral electrolytes with a pH of less than 9. In addition, research has found that iron impurities in KOH increase the OER activity for nickel catalysts [45]. Similar to low concentrations of KOH, pure water suffers CO_2 contamination resulting in decreased ionic conductivity for the AEM and the catalyst layers [46].

Studies show that dissolved ionic electrolytes outperform water. Hydroxide electrolytes show the best performance at an average current density of 220 mA/cm^2 at 1.8 V. Bicarbonate solutions such as K_2CO_3 report an average of 160 mA/cm^2 at 1.8V and water in comparison has an average of 95 mA/cm^2. There are studies that outperform the average values, but they are usually done so at high operating temperatures and PGM catalysts. [5]

2.9 Electrochemical measurements

2.9.1 Voltammetry

Voltammetry is an electrochemical technique to understand how materials behave and interact electrochemically. It is usually carried out in a three-electrode cell controlled by a potentiostat. High-purity reagent gases are utilized to exclude electronegative species other than the ones of interest. An applied potential with respect to the reference electrode

is carefully chosen to avoid unwanted oxidation or reduction. A potential program is often generated, e.g a step program or a ramp program, to record an accurate potential. The result of voltammetry is voltammograms, a plot of current versus potential. [47]

Linear sweep voltammetry (LSV) and cyclic voltammetry (CV) are two well-used voltammetry techniques for studying redox reactions. For LSV, a linear potential is applied at a constant rate as followed:

$$E(t) = E_0 \pm vt \tag{2.11}$$

E(t) is the potential at a given time, E_0 is the starting potential, v is the scan rate, and t is the time. vt is either negative or positive depending on if it is a cathodic sweep (negative) or anodic sweep (positive). CV on the other hand, as the name indicates, cycles back and forth in a given potential range. [48, 47]

A typical oxygen reduction reaction (ORR) LSV at a platinum electrode is illustrated in Figure 2.5. The figure illustrates some information one can obtain from the voltammogram. The different regions are indicated in the figure as well as the limiting current (i_{lim}), overpotential at specific current density (η_i), and the onset potential (E_{onset}). [49, 50]

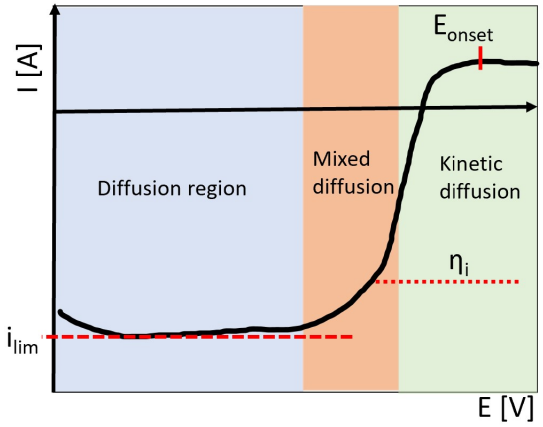

Figure 2.5: Illustration of a typical ORR LSV of platinum saturated with oxygen.[49, 50]

Voltammograms can also be investigated as Tafel plots to further study the kinetics of the reaction. For oxidation, the following proportionality exists [47]:

$$i_{ox} \propto \exp\left(\frac{a_{ox}\mathrm{F}}{\mathrm{R}T}E\right) \tag{2.12}$$

To be able to evaluate the rate of the reaction, Ω_j, a derivative of equation 2.12 can be found as equation 2.13 [47].

$$\frac{\partial \log(i_j)}{\partial \log(a_j)} = \Omega_j \tag{2.13}$$

The activity, a, can be found by utilizing equation 2.14 [47].

$$a = \gamma_{\pm} \left(\frac{c}{c^{\circ}} \right) \tag{2.14}$$

γ can be found by utilizing the Debye-Hückel limiting law found as equation 2.15. For the limiting Debye-Hückel, μ_{DH} is equal to 727 mM at 25°C. Debye-Hückel predicts mean ionic activity coefficients accurately for low concentrations, but not for higher concentrations [47].

$$\gamma_{\pm} = \exp\left(z_{+} z_{-} \sqrt{\frac{\mu}{\mu_{\mathrm{DH}}}} \right) \tag{2.15}$$

μ is the ionic strength and is described by the following equation [47]:

$$\mu = 0.5 \sum_{i=1} z_j^2 c_j \tag{2.16}$$

2.9.2 Rotating disk electrode

A rotating disk electrode (RDE) is an electrode used to measure hydrodynamic and convective-diffusion equations for electrochemical steady-state systems. It is a useful electrochemical technique to study electrode reaction kinetics and mechanisms. The electrode consists of a disk of an electronic conductor sealed in an insulating material such as Teflon. Figure 3.2 shows a rotating disk electrode schematically. The electrode is connected to a rod that is attached to a motor vertically and submerged in a bulk electrolyte solution. A laminar flow at the rotating disk enables mass transport from the electrolyte to the electrode surface. The rotation from the electrode stirs the electrolyte far away from the electrode while the electrolyte close to the electrode tends to rotate with the electrode. This is due to the spinning disk dragging the fluid along its surface. The centrifugal force flings the solution from the center in a radial direction. See Figure 2.6 for an illustration of how the electrolyte is interacting with the RDE. [47, 51, 52, 53]

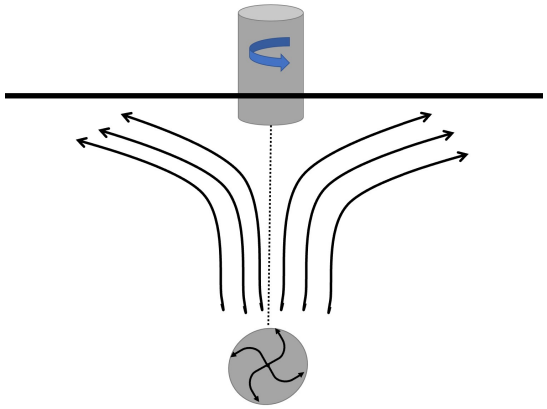

Figure 2.6: Sketch of how the electrolyte flow near the rotating disk electrode. Illustration adapted from literature [54].

For an electrolyte solution containing excess supporting electrolytes, one can neglect ionic migration. The processes left to transport material are diffusion and convection. When the solution is stirred by rotating the electrode, steady-state current density is achieved. This is because the thickness of the diffusion layer is fixed and controlled by convection. The transport rate of reactants through the diffusion layer is controlled by diffusion. For RDE measurements, the rotation rate can be varied, which allows control over the diffusion layer thickness. [47, 51, 52, 53]

The mathematician, Levich, found a mathematical relation between convection and diffusion for RDE. Under steady-state conditions a limiting current can be found by utilizing the Levich equation [54]:

$$i_{\mathrm{L}} = 0.62 n \mathrm{F} A D^{2/3} \nu^{1/6} C \omega^{1/2} \tag{2.17}$$

n is the number of electrons transferred, F is Faradays constant, A is the area of the electrode, D is the diffusion coefficient, ν is the kinematic viscosity of the electrolyte and C is the concentration of oxygen. ω is the angular rotation rate and relates to the experimental rotation rate of rounds per minute (f) as follows [54]:

$$\omega = \frac{2\pi f}{60} \tag{2.18}$$

The Levich equation is used to perform a Levich study of voltammograms at different rotation rates. The Levich study plots the limiting current versus the square root of the rotation rate. As seen in the Levich equation (equation 2.17), the plot will have a linear limiting current where the slope will be $0.62 n \mathrm{F} A D^{2/3} \nu^{1/6} C$. Extrapolation will intercept in origo. Another method to present the data from a Levich study is to do a Koutecky-Levich study. [51, 54]

2.9.3 Koutecky-Levich study

A common RDE experiment is to record a series of voltammograms at different rotation rates. A Koutecky-Levich study is quite similar to a Levich study, but rearranges the Levich equation to a reciprocal current versus the reciprocal square root of the rotation rate. The Koutecky-Levich equation is given below as equation 2.19. [51]

$$\frac{1}{I} = \frac{1}{I_k} + \frac{1}{I_L} \tag{2.19}$$

Rearranging the equation results in the following Koutecky-Levich equation:

$$\frac{1}{i} = \frac{1}{i_k} + \left(\frac{1}{0.62n\mathrm{F}AD^{2/3}\nu^{-1/6}C}\right)\omega^{-1/2} \tag{2.20}$$

The kinetic limitation current (i_k) is involved in the electron-transfer reaction. The current is defined in equation 2.21. It represents the current that flows if the mass transfer was efficient enough to maintain a similar concentration at the bulk and the electrode surface. Thereby, if extrapolation to the y-axis does not yield a zero intercept, the rate of the reaction is limited by slow kinetics at the surface of the electrode.[51, 54]

$$i_k = \mathrm{F}Ak_fC \tag{2.21}$$

Figure 2.7 illustrates how a typical Koutecky-Levich plot looks. The two regression lines are recorded at two different potentials, but have the same slope. The slope is $(0.62n\mathrm{F}AD^{2/3}\nu^{-1/6}C)^{-1}$ and the intercept for the extrapolation is i_k^{-1}. [47, 51]

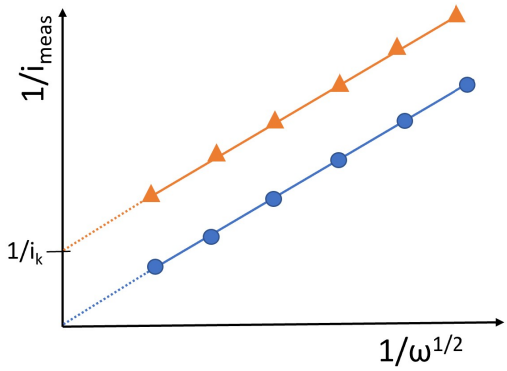

Figure 2.7: An illustration of a Koutecky-Levich plot. The solid line is a linear regression and the dotted line is the extrapolation to an infinite rotation rate. The blue regression line extrapolates to zero due to electron transfer being slow. A more rapid electron transfer can be observed for the red regression line. [51]

Koutecky-Levich study can be a useful technique when studying thin films on electrodes. By applying a thin film on a rotating disk electrode, one can find how it affects the kinetics of a given reaction such as the ORR of platinum with an ionomer thin film. At any point

at the voltammogram for the platinum ionomer film, the measured current is found to be as followed [55]:

$$\frac{1}{i_{\text{measured}}} = \frac{1}{i_L} + \frac{\delta}{n\text{F}D_{\text{film}}C_{\text{film}}} + \frac{1}{i_k} \tag{2.22}$$

By plotting $\text{i}_{\text{measured}}{}^{-1}$ versus $\omega^{-1/2}$, a linear plot should be obtained. The intercept is then given as $\frac{\delta}{n\text{F}D_{\text{film}}C_{\text{film}}} + \frac{1}{i_k}$ [55]. For the limiting current density, the equation will be given below in equation 2.22 [55].

$$\frac{1}{i_{\text{lim}}} = \frac{1}{i_L} + \frac{\delta}{n\text{F}D_{\text{film}}C_{\text{film}}} \tag{2.23}$$

The limiting current assures that the intercept of the linear regression to an infinite number of rotations will be equal to $\frac{\delta}{n\text{F}D_{\text{film}}C_{\text{film}}}$. The limiting current for a clean electrode without thin film is the Levich current (i_L). By utilizing the given equations, one can obtain $D_{\text{film}}C_{\text{film}}$ product of the different thin films [55].

2.9.4 Oxygen reduction reaction on thin film coated electrode

The use of RDE with a thin film presents a viable approach for modeling electrochemical reactions in a half-cell system. The technique focuses on the diffusion of O_2 across a thin ionomer film towards the surface of a platinum catalyst. Figure 2.8 provides a visual representation of how the limiting currents and oxygen concentration change within the thin film and electrolyte [56]. In the area of oxygen reduction reaction (ORR), which occurs in the potential range of 1.2V to 0 V vs. RHE for platinum, oxygen will diffuse through the thin film. The reason for performing ORR instead of OER is to ensure the integrity of the thin film where gas evolution may dislodge the thin film from the electrode surface. The four electron pathway for ORR is given as the following reaction [50]:

$$\text{O}_2 + 2\,\text{H}_2\text{O} + 4\,\text{e}^- \rightleftharpoons 4\,\text{OH}^- \tag{2.24}$$

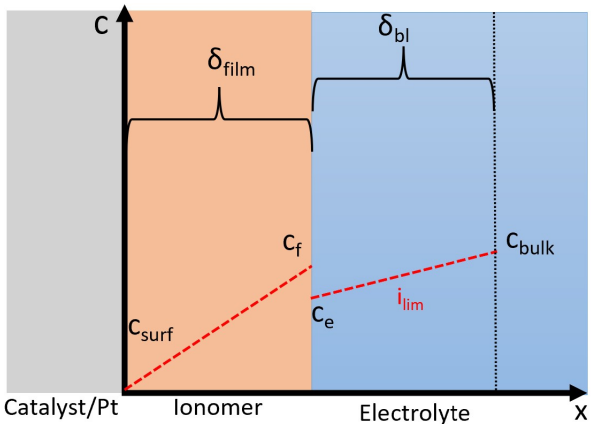

Figure 2.8: Illustrates the concentration change of oxygen through a thin film coated on a Pt electrode or catalyst. Figure is adapted from literature [56]

The difference between the concentration of oxygen in film (C_f) and the concentration of oxygen in the electrolyte (C_e) is given in equation 2.25. γ is a partition coefficient between the bulk electrolyte and the thin film. [56]

$$C_f = \gamma C_e \tag{2.25}$$

For hydrodynamic methods, such as RDE, the O_2 flux is controlled and kinetic currents can be extracted by applying the Koutecky-Levich equation.

2.9.5 Polarization

To analyze electrode reactions, i-E curves are commonly uses, where the current is measured as a function of potential [51]. When a current flows through an electrode, it triggers a series of side reactions that impede the electrode processes, which is known as electrode polarization [47]. Heterogeneous electrode reactions can be characterized by their reaction rate using equation 2.26, where i represents the current density, n is the number of electrons consumed in the reaction and F is the Faraday's constant [51].

$$r = \frac{i}{n\mathrm{F}} \tag{2.26}$$

The reaction rate is influenced by factors such as mass transfer, kinetics, and surface-related effects. In a cell, there is an equilibrium potential that serves as a reference potential. The overpotential, denotes as η, indicates the degree of polarization [51].

$$\eta = E - E_{\mathrm{eq.}} \tag{2.27}$$

The current in electrode reactions are influenced by various factors, including mass transfer, electron transfer at the surface of the electrode, chemical reactions, and other surface-

related reactions such as adsorption, desorption, and crystallization [51]. Electrode polarization, which results from these factors, can be categorized into three types: Ohmic-, kinetic- and transport polarization. Each type contributes to the overall polarization observed in polarization curves. These curves can be obtained using a two-electrode or three-electrode setup with a potentiostat that controls the applied current or potential in the cell. Figure 2.9 illustrates a typical polarization curve for alkaline water electrolysis, with different areas of polarization overpotentials marked on the curve. [47, 31]

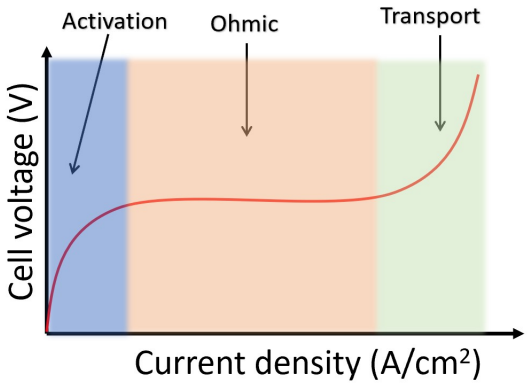

Figure 2.9: A simple sketch of a typical polarisation curve for alkaline electrolysis. The different regions marked in the figure illustrate different polarisation overpotentials. Figure adapted from literature [57].

The initial portion of the polarization curve, referred to as activation polarization, is often denoted as the kinetic region. This is due to the sluggish kinetics of the OER at the anode, which has a significant impact on the electrochemical reactions. The activation region is primarily influenced by the properties of the catalyst layer, including the type of catalyst, its loading, active area, and stability. [47, 31]

The ohmic region, which represents the largest portion of the polarization curve, is a crucial area for investigation. The main factors responsible for ohmic losses are the AEM conductivity. The conductivity of the bipolar plates and GDLs are also relevant when determining the extent of the ohmic region. [31]

Finally, the transport region is also known as the concentration polarization or mass transfer region. This region is observed at high current densities and is limited by the mass transfer of gas diffusion and water transport within the porous catalyst layers. [31]

2.9.6 Electrochemical impedance spectroscopy

Electrochemical impedance spectroscopy (EIS) is a technique to measure resistance in a circuit by applying a sinusoidal alternating current (AC). The definition of resistance, R, is given as the following equation:

$$R = \frac{V}{i} \tag{2.28}$$

V is the voltage and i is the current density. For impedance, Z, the definition is as follows [58]:

$$Z = \frac{V(\omega)}{i(\omega)} \tag{2.29}$$

The sinusoidal current is applied at a given frequency resulting in the voltage and current density being dependent on the frequency. For EIS experiments either a sinusoidal current or potential is applied to an electrochemical system in which the current or potential out of the system is recorded at varying frequencies [58]. The amplitude of the signal remains constant. For potentiostatic EIS (applied potential) the potential is applied as followed:

$$E(t) = E_0 \sin(\omega t) \tag{2.30}$$

Equation 2.30 shows the potential that is applied to the system. A current signal with the same frequency is recorded. However, the output current is phase shifted and exhibits an amplitude different from i_0, given by the system's impedance. The output current is given below in equation 2.31 [58].

$$i(t) = i_0 \cos(\omega t - \varphi) \tag{2.31}$$

The sinusoidal signal can be expressed as a complex number. The complex number will consist of a real part and an imaginary part which is described in equation 2.32. [58]

$$Z = Z_{re} - jZ_{im} \tag{2.32}$$

By plotting Z_{re} on the x-axis and Z_{im} on the y-axis a Nyquist plot is obtained. A typical Nyquist plot is illustrated in Figure 2.10 in which a Randles circuit with a constant phase element (CPE) is implied as the circuit model. [58]

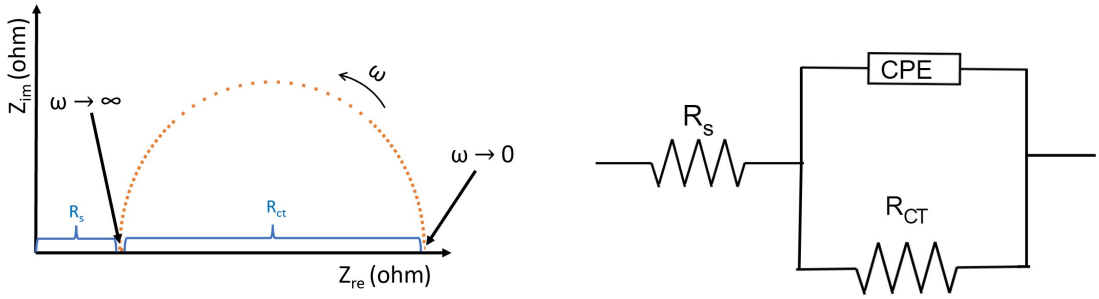

(a) Illustration of a typical Nyquist plot.

(b) Simple equivalent circuit containing constant phase element

Figure 2.10: Nyquist plot and a circuit model [58]

R_{CT} is the charge transfer resistance and is related to the kinetics of the electrochemical process. R_s indicates the ohmic resistance.

When analyzing EIS data, one typically utilizes software to compute fitting curves and equivalent circuits. For depressed Nyquist semicircles, it is possible to use a CPE instead of an ideal capacitor. This results in impedance described as follows:

$$Z_{CPE} = \frac{1}{Y(j\omega)^n} \tag{2.33}$$

The constant Y gives the capacitance and is given in Fs^{n-1}. n indicates the deviation from ideal behavior from 0 to 1. It is related to the angle of the semicircle fitting which indicates the behavior of the CPE. Equation 2.34 gives the relation for the angle and the constant n. A simple equivalent circuit containing CPE is given in Figure 2.10(b).[58]

$$\theta = 90^\circ(1 - n) \tag{2.34}$$

For AEMWE, a commonly used equivalent circuit is depicted in Figure 2.11. In this case, $\mathrm{R_s}$ describes the internal ohmic resistance which includes the electrodes, membrane, and PTLs. It is common to ascribe the two time constants to the process at the anode and the cathode, respectively. [59, 60]

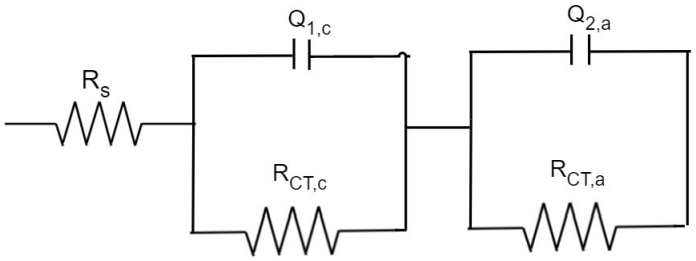

Figure 2.11: A typical circuit model for AEMWE with time constants scribed to cathode and anode.

2.10 Surface characterization

In order to measure the thicknesses of the thin films and investigate the surface topography, two different scanning probe techniques were utilized. For the catalyst layers, a scanning electron microscope (SEM) was used to visualize the morphology. Mercury porosimetry was utilized to investigate pore distribution.

2.10.1 Stylus profilometry

Stylus profilometry is a method to study the morphology and topography of samples such as the height of thin films. The instrument consists of a stylus probe that is in contact with the sample which measures the height variations by moving the probe across the sample. The mechanical movement is recorded and converted to electrical signals. These signals can be converted to topography graphs to acquire height differences and surface morphology. [61]

2.10.2 Scanning electron microscopy

A scanning electron microscope (SEM) is a microscope able to generate high-resolution images by focusing a beam of electrons on a surface. The electrons interact with the atoms on the surface of the sample and dislodge electrons from the sample. These electrons are called secondary electrons (SE) attracted to a positive detector. SE give information about the surface topography. Primary electrons that are bounced back off the sample surface are also possible to analyze by SEM. The energy of the back-scattered electrons (BSE) is related to the density of the atoms which can give information on the composition of the sample. [62, 63]

2.10.3 Mercury porosimetry

Mercury porosimetry represents a destructive analysis technique utilized to measure the overall porosity and pore distribution of porous materials. The technique is able to measure pore sizes from 360 µm to 6 nm. It capitalizes on the non-wetting nature of mercury when it is in contact with porous structures such as catalyst layers on AEMs. To infiltrate the surface pores, mercury needs a pressure exceeding the saturated vapor pressure. As the pressure is incrementally raised, progressively smaller pores are filled with mercury, enabling the determination of pore size distribution. The pore diameter, D, can be calculated utilizing the Washburn equation (equation 2.35). [63]

$$D = \frac{-4\zeta\cos\theta}{P} \tag{2.35}$$

Here, the surface tension (ζ) typically exhibits a value of 485 mN/m and opposes expansion upon contact. The wetting angle (θ)) exceeds 90° for non-wetting fluids and is dependent on the roughness and chemistry of the surface. P is the pressure applied. To overcome the surface tension for pores of increasing sizes, the hydrostatic pressure is gradually increased in small increments. The volume of the pore is determined by measuring the volume of mercury within the pores of the sample and the intrusion of the sample at different pressures. Experimental measurements are conducted to determine the volume of mercury by assessing the electrical capacitance of the sample container. [63]

3 Experimental

3.1 Flow chart for experimental procedures

A flow chart given below in Figure 3.1 gives an overview for the experimental procedures conducted in this thesis. Some of the experimental procedures are conducted in earlier work done by the author (Section 3.3, 3.5, 3.6, 3.7 and 3.8) [10].

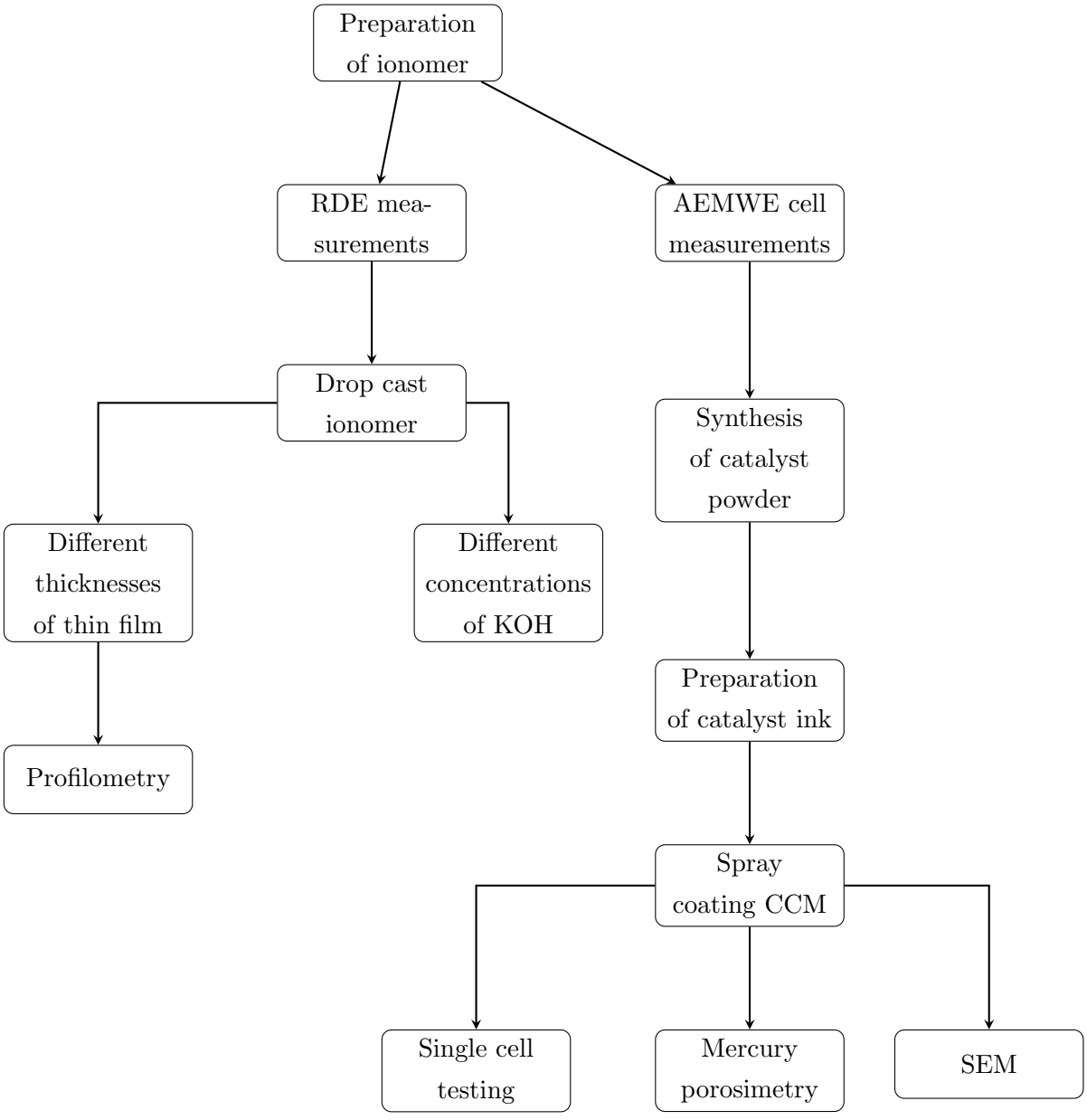

Figure 3.1: Flow chart providing an overview of the experimental procedures.

3.2 Chemicals and instruments

The instruments utilized in the project are given below in Table 3.1. In addition, are the chemicals given in Table 3.2.

Table 3.1: A summary of the instruments utilized in the project.

Manufacturer	Instrument	Usage
Ivium technologies	Ivium-n-stat	RDE measurements
Pine Research	MSR rotator	RDE measurements
Mahr	MarSurf M400 + SD 26	Profilometry
Binder	Vacuum drying furnace model VD23	Drying catalyst powder
VWR	Ultrasonic Cleaner	Ultrasonic bath
Branson	Digital sonifier	Ultrasonic probe sonicator
Ultrasonic system Inc	Prism-400	Machine spray coating
BioLogic	VSP potentiostat and VMP3B20 booster	Single cell testing
SINTEF TS2	SINTEF	Single cell testing
Milli-Q	Ultrapure water Millipak 0.22 µm	DI water
Zeiss	Ultra 55	SEM
Micrometrics	AutoPore IV 9520	Mercury Porosimetry

Table 3.2: Summary of the chemicals utilized in the project.

Manufacturer	Chemical	Usage	Purity
Sigma Aldrich	$NiCl_2{\cdot}6H_2O$	Catalyst synthesis	≥97%
Aldrich chemistry	$FeCl_3{\cdot}6H_2O$	Catalyst synthesis	≥99%
Aldrich chemistry	$NaBH_4$	Catalyst synthesis	≥98%
Sigma Aldrich	Dimetyl sulfoxide (DMSO)	ionomer solution	≥99.9%
Merck	2-propanol (IPA)	catalyst ink	99%
Sigma Aldrich	KOH	Electrolyte	85%
Alfa Aesar	Pt 50% nominally on carbon black	Catalyst	-

3.3 Preparation of ionomer

20 grams of ionomer was prepared to be coated on Pt electrode and added in catalyst inks. 1 g of Evoion Duraion GEN2 ionomer dry OH^- form was mixed with 19 g Dimetyl Sulfoxide (DMSO). The ionomer solution was stirred with a magnetic stirrer until a homogeneous mix was achieved in approximately 72 hours.

3.4 Rotating disk electrode measurements of platinum

Electrochemical rotating disk measurements of platinum with an ionomer thin film were done in a three-electrode Teflon cell. A Pine Research rotating disk was connected to a Ivium-n-stat multi-channel potentiostat. A Hg/HgO electrode was used as the reference electrode and a graphite rod as a counter electrode. The reference electrode was calibrated in a hydrogen saturated alkaline solution (pH=14) to a potential of $E_{Hg/HgO}$=-0.926 V vs. RHE. The working electrode was a 5 mm diameter platinum Pine Research electrode. The working electrode was first polished by using 0.5-, 0.3- and 0.05 μm Allied High-Tech aqueous alumina suspension on polishing pads. The working electrode was sonicated in water for 10 minutes before being coated with an ionomer. The coating was done by drop-casting an ionomer solution on the rotating disk electrode (see Figure 3.2). The thin films were dried on the electrode under a fume hood overnight.

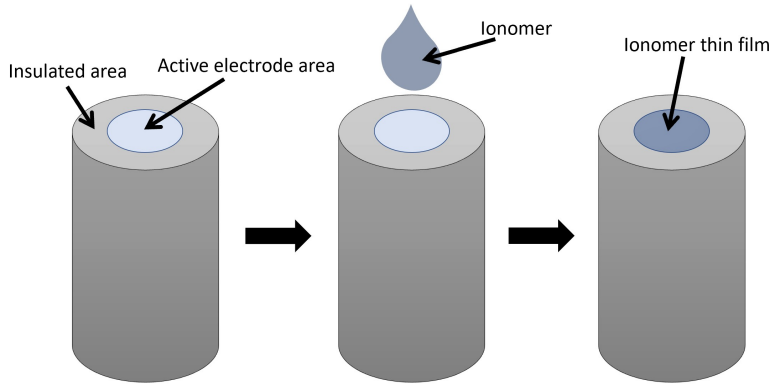

Figure 3.2: Illustrating how a solution such as an ionomer is drop cast on a rotating disk electrode. The insulated area is usually made of Teflon.

KOH solutions of either 1M, 0.1M, or 0.01M were prepared by mixing potassium hydroxide pellets and 18.2 MΩ · cm Milli-Q ultrapure water Millipak 0.22 µm distilled water. The KOH solution was added to a Teflon cell and purged with oxygen gas for 30 minutes. 100 CVs were recorded at 100 mV/s in the range of -0.876V to 0.274V versus Hg/HgO followed by 5 CVs at 20 mV/s in the same range. LSVs at 5mV/s were recorded at the following rpms: 400, 900, 1200, 1600, and 2400 in the range of -0.876V to 0.274V. In the end, OER was conducted in the range of 0.274V to 0.674V vs. Hg/HgO to dislodge the thin film from the electrode.

3.5 Synthesis of NiFeB catalyst powder

NiFeB catalyst powder was prepared by utilizing a procedure adapted from [29]. NiFeB was synthesized by mixing 3.57 g of $NiCl_2{\cdot}6H_2O$ and 2.03 g of $FeCl_3{\cdot}6H_2O$ in 150 mL of 18.2 MΩ · cm Milli-Q ultrapure water Millipak 0.22 µm distilled water. The precursor was stirred for 15 minutes at approximately 750 rpm. The precursor was added to a 750 mL

0.1 M $NaBH_4$ solution followed by 15 minutes of stirring at 750 rpm. The solution was then centrifuged 4 times at 8000 rpm for 6 minutes and cleaned with water and ethanol. The solution was dried in a Binder vacuum drying furnace at 60 °C for 18 hours. The powder was hand milled to a fine powder.

3.6 Preparation of catalyst inks

Catalyst powder was weight in a glass vial before adding 18.2 MΩ · cm Milli-Q ultrapure water Millipak 0.22 µm distilled water. The slurry of water and catalyst powder was sonicated for 2 minutes in an ultrasonic bath. Evoion Duraion GEN2 ionomer solution was then added to the slurry before an additional 10 minutes of sonication in an ice bath. IPA was then added to the slurry before sonicating for 15 minutes in an ice bath. The ink slurry was then probe sonicated by a Branson digital sonifier for either 5 minutes (NiFeB ink) or 3 minutes (Pt/C ink) at an amplitude of 40% and on/off time of 0.5s/0.5s. The catalyst ink was then stirred with a magnetic stirrer until spraying was complete. Table 3.3 gives the amount of each component for the catalyst inks prepared.

Table 3.3: Catalyst ink content. Two different NiFeB inks were prepared and one Pt/C ink.

Sample	**Catalyst** [g]	**Ionomer** [g]	**water** [g]	**IPA** [g]
NiFeB (10% ionomer)	1	1.15	25	25
NiFeB (20% ionomer)	1	1.25	25	25
Pt/C (20% ionomer)	1	1.25	25	25

3.7 Spray coating

An Ultraspray PRISM-400 machine spray coater was utilized to spray coat Duraion Evomem Gen 3 membranes. The catalyst inks were loaded into the syringe and a magnetic stirrer was initiated. The membranes were placed on a vacuum heating plate set at 70 °C. A plastic cover was placed over the membrane with a 2.5 x 2.5 cm cutout in the middle to be spray coated. A larger stainless steel mask was placed on top with a 5 x 5 cm cutout. The height of the spray coater nozzle was 50 mm and the flow rate was set to 1 ml/min. The corner speed was set to 80 mm/s and the head speed to 100 mm/s. The spray area was set to 5x5 cm and the mapping was set to spray back and forth from each side. The nitrogen air pressure was 10 PSI. The recipe was repeated until the NiFeB anode had a loading of 3.5 $mgcm^{-2}$ and 3 $mgcm^{-2}$ for the Pt/C cathode. After spray coating the AEMs they were transferred to OH^- form by soaking them in 1M KOH for 48 hours (before cell testing). The KOH solution was frequently changed during the 48 hours.

3.8 Single cell testing

3.8.1 Cell assembly

The AEMWE cell components, given in Figure 3.3, were first polished with 0.3 µm Allied High-tech aqueous alumina suspension followed by sonication in water a couple of times. Before assembling the cell, the components were lightly rinsed in ethanol. Freudenberg cover gaskets were cut out by hand by utilizing a template for the correct size. 5mm thick gaskets were used for the cathode and 0.35 mm for the anode. Several pressure tests of FujiFilm Ultra super low pressure LLLW pressure paper were completed to ensure a tight and uniform cell assembly. The cell was tightened incrementally from 1Nm to 3.5Nm using a Newton-meter. It was tightened diagonally and gradually to ensure an even distribution where the gap between the sides was constantly measured. Nickel fiber felt was used as anode GDL and Toray carbon paper was used as cathode PTL. They both were cut out by hand at 2.5 x 2.5 cm.

Table 3.4: Cell configuration for electrochemical tests of CCMs. 3.5 Nm of force was applied to tighten the cell.

Cathode	4 mm Flow Field	0.5 mm gasket	0.4 mm GDL
Anode	3.5 mm Flow Field	0.35 mm gasket	0.6 mm PTL

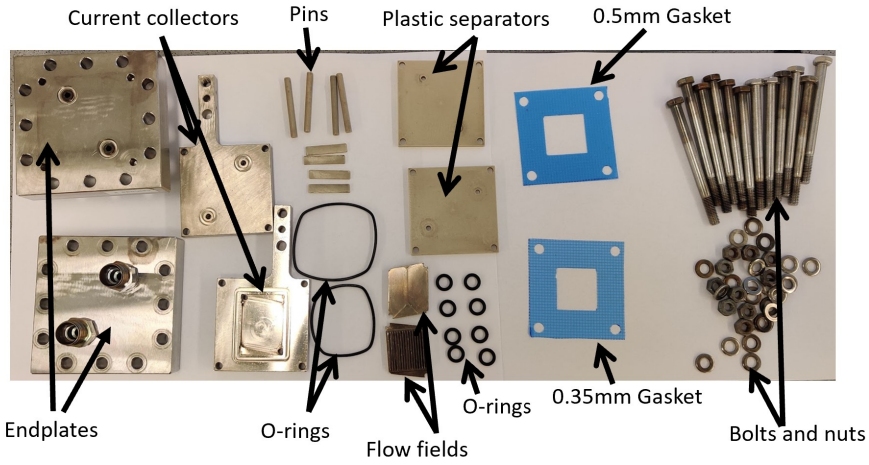

Figure 3.3: Cell components of AEMWE used in this project. Each component is given in the image. The membrane, PTL and GDL is not illustrated. Figure reused from [10]

3.8.2 Single cell testing

Testing of AEMWE cell was conducted in SINTEF TS2 test station with a BioLogic VSP potentiostat and VMP3B20 booster to evaluate its performance. The setup is illustrated in Figure 3.4. The test station was first rinsed three times by circulating DI water for approximately 5 minutes each. 3L 1M KOH solution was added to the test station and

circulated for 30 minutes at 250 mLmin^{-1} before an activation polarisation curve was recorded followed by 1 hour of additional circulation. A polarisation curve was recorded with a stepwise increase of 0.125A every 15 seconds. Galvanostatic EIS was then recorded at 0.625, 3.125, 6.250 and 9.340 A at an amplitude of 0.031, 0.156, 0.313 and 0.467 A. The frequency range was 10 kHz to 0.01 Hz. The test station was then rinsed twice before adding 0.1M KOH and repeating 30 minutes of circulation, polarisation curve and EIS. This was repeated for 0.01M KOH electrolyte as well before a second time with 1M KOH. After the second recording in 1M KOH a durability polarisation curve at 6.25A for 18 hours were conducted. Fitting of Galvanostatic EIS was done utilizing the software: EC-lab. The circuit model is given in Figure 2.11.

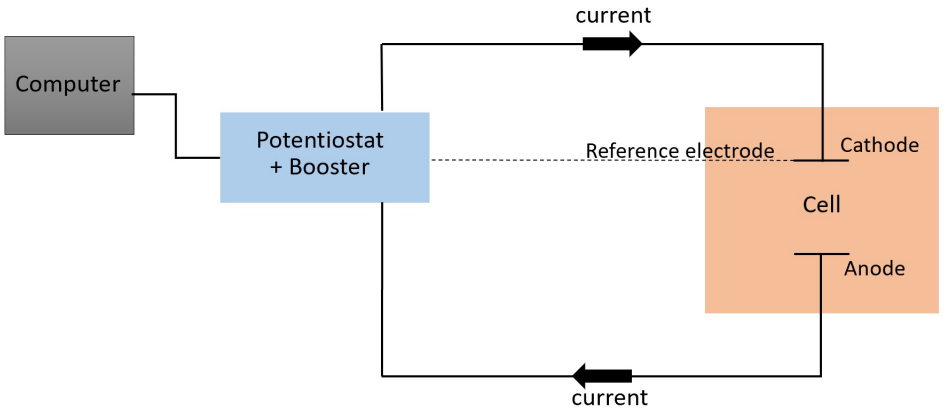

Figure 3.4: Schematic of Sintef TS2 test station to perform AEMWE. Figure inspired by [10].

3.9 Scanning electron microscope characterization

A Zeiss Ultra 55 SEM with a field emission electron gun was utilized to study the morphology of the spray-coated CCM. Cross-sections of the CCMs were created by cooling the CCMs in liquid nitrogen before breaking them in half. The sample was placed in a sample holder with a spacer on each side. Secondary electrons of an accelerating voltage of 15 kV and an aperture of 60 µm were used. The working distance was 5 mm. The images were analyzed with the software tool ImageJ.

3.10 Profilometry

A Mahr Marsurf M400 + SD26 was used to measure the thicknesses of ionomer thin films on Pt electrodes. The electrode was placed under the tip of the profilometer driver before adjusting the tip close to the electrode. The length of measurement, L_T, was set to 8mm. At least 4 separate measurements were completed of each thickness. The profiles obtained from the profilometer were printed out from the instrument directly before being analyzed.

3.11 Mercury porosimetry

An Autopore IV 9520 mercury porosimeter was utilized to analyze the porosity of the anode catalyst layers containing NiFeB with 10 wt% and 20 wt% ionomer. The catalyst layers were spray coated on clear plastic and cut into small pieces. The pieces were added to a penetrometer stem before being weight. The penetrometer was subsequently placed in the low-pressure port and evacuated to reach a low pressure. Afterward, the penetrometer was weighed again before being transferred to the high-pressure port to initiate high-pressure analysis.

4 Results

The results section begins with the presentation of profilometry measurements, which characterize the thicknesses of ionomer thin films on Pt electrodes. Subsequently, three sections provides RDE measurements, investigating ionomer thin films with varied thicknesses and different concentrations of KOH. Following these sections, the research work includes single cell tests, cross-sectional SEM images and mercury porosimetry of CCMs obtained from the aforementioned single cell tests.

4.1 Profilometry of ionomer thin films

The thicknesses of ionomer solution drop cast and dried on Pt RDE were measured by profilometry. The corresponding thickness measurements of the thin films are presented in Table 4.1. Visual inspection of the thin films was performed to ensure homogeneous and even-looking thin films. Thin films with an uneven surface or insufficient coating were not selected to be used for measurements. The emphasis was placed on achieving a consistent and homogeneous film rather than varying the thickness extensively. However, a good variety of thicknesses was achieved.

Table 4.1: Amount of ionomer solution drop cast on electrodes and the thickness after drying.

Ionomer solution [µl]	**Thickness of thin film** [µm]
10	43.0 ± 2
9	41.0 ± 2
8	38.0 ± 1
7	35.0 ± 2
6	33.0 ± 3

4.2 Koutecky Levich study of different thicknesses of ionomer thin films

Voltammograms were recorded for Pt electrodes with and without ionomer thin films to investigate the influence of film thickness on oxygen diffusivity. Initially, Ni was tested as the electrode, but proved not to be suited to perform ORR. It is illustrated in Appendix E. LSVs of pure platinum and different thicknesses of ionomer thin films in 1M KOH are illustrated in Figure 4.1. A large difference in the limiting current densities was observed for the thin films compared to pure Pt (about 10 times larger for pure Pt compared to ionomer thin films). In addition, there was a relatively large difference in limiting currents for different thicknesses of ionomer thin films.

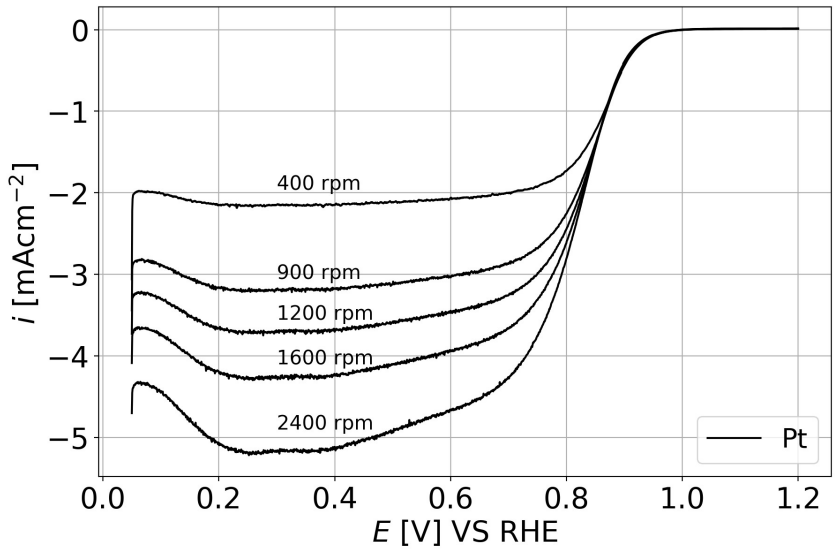

(a) LSV for pure Pt

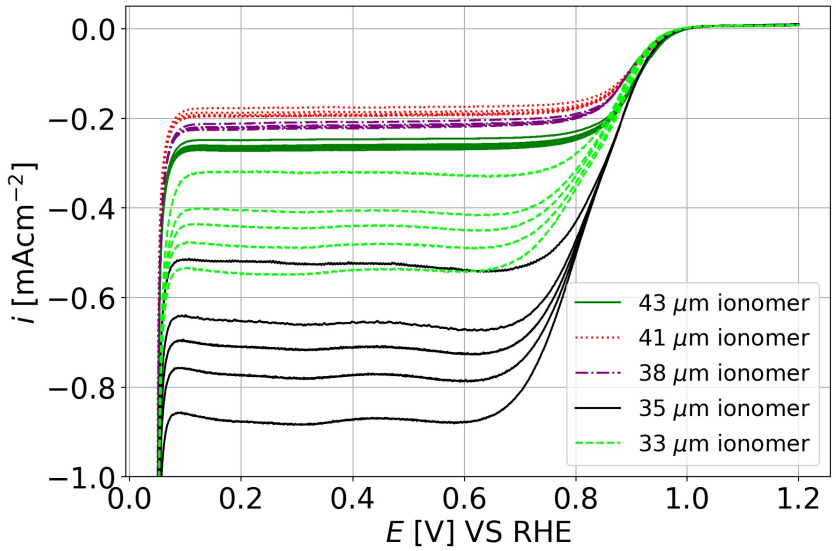

(b) LSV for ionomer thin films

Figure 4.1: LSVs at different rpms for pure Pt and different thicknesses of ionomer thin films in 1M KOH saturated with O_2. The rpms are increasing as the cathodic current is decreasing. The LSVs are measured at a scan rate of 5 mV/s in the range between 0.05V to 1.2V vs. RHE. The LSVs in (b) can be found as individual figures in Appendix A.

Figure 4.2 illustrates a steady-state Koutecky-Levich plot constructed using the limiting currents obtained from the voltammograms presented in Figure 4.1. The plot reveals two distinct regions, wherein the three thickest thin films exhibit high intercept values compared to the two thinnest thin films. Pure Pt extrapolated almost at origo, which was expected. An increase in thickness correlates to an increase in intercept values.

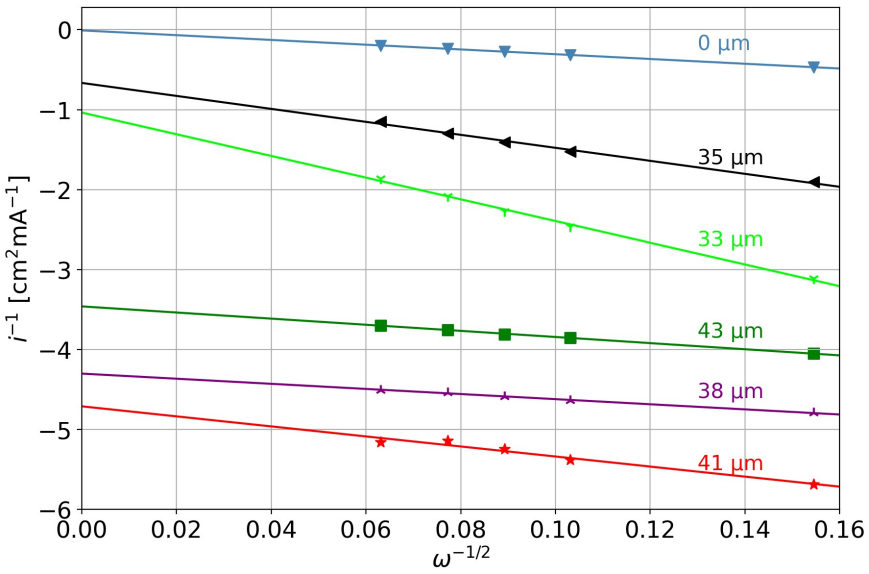

Figure 4.2: Koutecky-Levich plot of different thicknesses of ionomer thin films and pure Pt for limiting currents at 0.426 V vs. RHE.

Data obtained in the Koutecky Levich plot (slope, intercept, R^2-value, and standard deviation) is shown in Table B.1 in Appendix B. It was possible to calculate the $D^{2/3}C$ product for oxygen at the pure Pt electrode by utilizing equation 2.20 and the slope obtained in the given plot. $D^{2/3}C$ for pure Pt was calculated to be 3.381 $\pm$ 0.0023 $\cdot 10^{-6}$ moldm^{-3}cm^{-2}s-1.

The DC product for the thin films was calculated by applying equation 2.23 and is illustrated in Figure 4.3. It is noteworthy that the 35 µm thin film exhibits the highest DC product, primarily because it has the highest intercept in the Koutecky Levich plot. However, the differences are small and lie within the uncertainty of the values observed in Figure 4.3. Therefore, DC is constant and independent of the thickness of ionomer thin films.

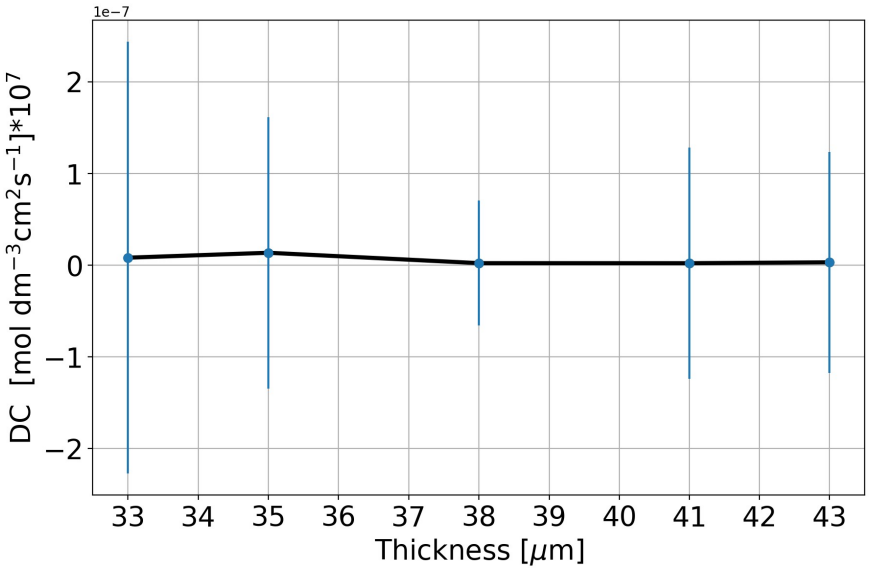

Figure 4.3: *DC* product for different thicknesses of ionomer thin film. The data from the plot can be found in Table B.6 in Appendix B.

To study the reduction rate of the thin films, Koutecky Levich plots for the rising portion of the voltammograms were plotted. The rising portion is the mixed diffusion/kinetic diffusion region of the LSV and was observed at approximately 0.85 V. Found below in Figure 4.4 is the Koutecky Levich plot obtained for a potential of 0.85V. In Appendix B, similar Koutecky Levich plots for potentials 0.825V and 0.9V can be found with additional data.

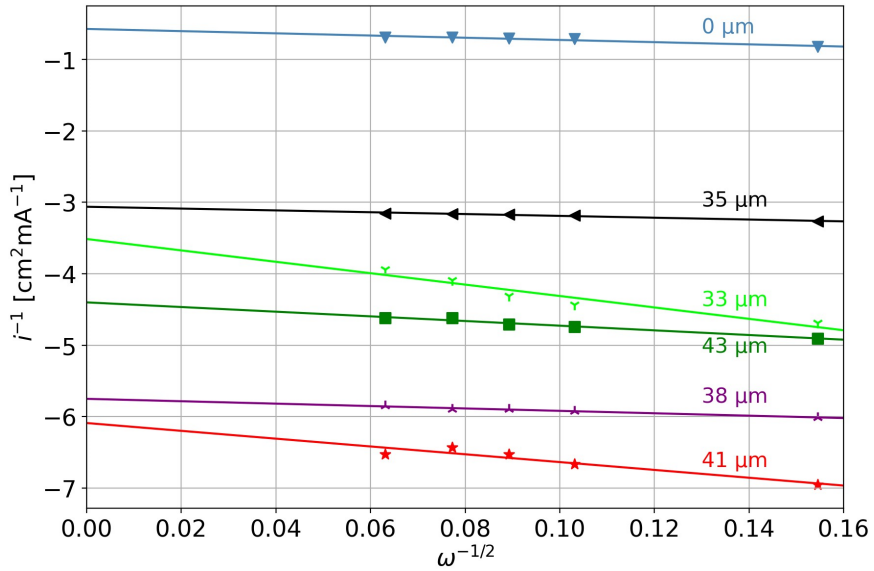

Figure 4.4: Koutecky-Levich plot of different thicknesses of ionomer thin films and pure Pt for the rising portion of voltammogram at 0.85 V vs. RHE.

In the Koutecky Levich diagram, it was observed that the intercepts at the rising portion were at a higher cathodic current compared to the limiting current. Ideally, the slopes

should be the same, but a small increase was observed. The data obtained from the Koutecky Levich plot is presented in Figure B.2. The relation of intercepts vs. thickness and slopes vs. thickness is illustrated in Figure B.3 in Appendix B.

The kinetic currents for the thin films were determined using equations 2.23 and 2.22, incorporating the *DC* product obtained for the limiting currents. In the case of pure Pt, the kinetic current i_k was calculated by utilizing equation 2.20 and the extrapolation to the y-axis. The calculated kinetic currents are presented in Table B.5 as absolute values and visualized in Figure 4.5. Notably, there is a relationship between the thickness of the film and the kinetic current for the thin films, indicating an increase in the kinetic current with increasing film thickness. However, the bare Pt electrode exhibited the highest kinetic current. Additionally, it was observed that the kinetic currents decreased with an increase in potential. This is illustrated in Figure 4.5. There is observed a large uncertainty in the datapoints at 41 µm, especially at 0.825 V.

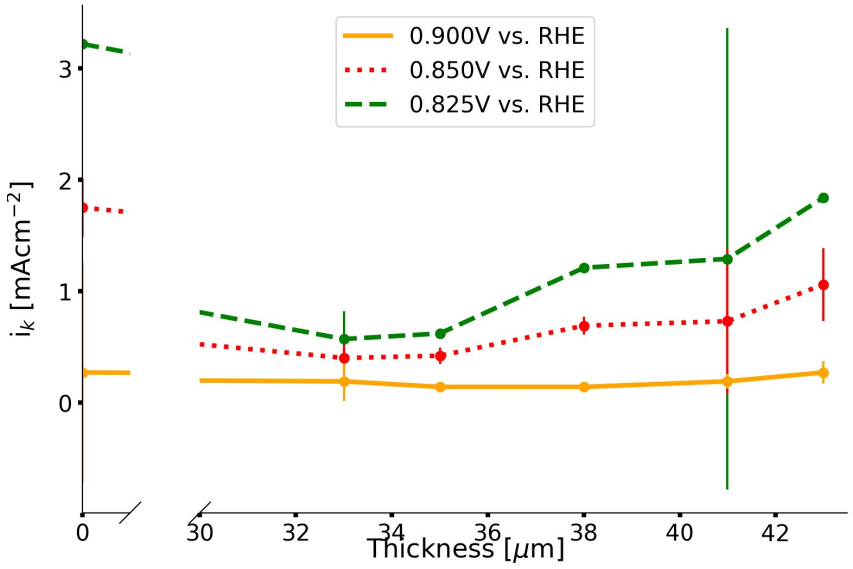

Figure 4.5: Kinetic current for various thicknesses of ionomer thin films at different potentials in 1M KOH.

4.3 Voltammograms of ionomer thin film in different concentration of KOH

RDE measurements were conducted at different concentrations of KOH to investigate the pH dependency of ORR for ionomer thin films. Figure 4.6 depicts the LSVs for a 43 µm ionomer thin film and pure Pt at three different concentrations of KOH. Notably, the limiting current densities for the thin film were approximately 10 times smaller compared to pure Pt. However, it should be mentioned that there was some noise observed in the LSV curve for pure Pt at a rotation rate of 2400 rpm in 0.1 M KOH. CVs for pure Pt and ionomer thin films at different concentrations are found in Appendix C.

Regarding the thin film, it is a clear that an increase of electrolyte concentration results in lower cathodic limiting currents. Additionally, a slight shift in overpotential at the rising portion of the curve was observed. Furthermore, the difference in limiting currents for different rotation rates decreases with increasing concentration. At 1M KOH, the difference in limiting currents for the ionomer thin film is considerably lower compared to the other concentrations. For the bare Pt electrode, a shift in overpotential at the rising portion of the voltammogram was also observed. Specifically, the Pt electrode in 0.01M KOH overlapped with the curves of 0.1M and 1M KOH in this region.

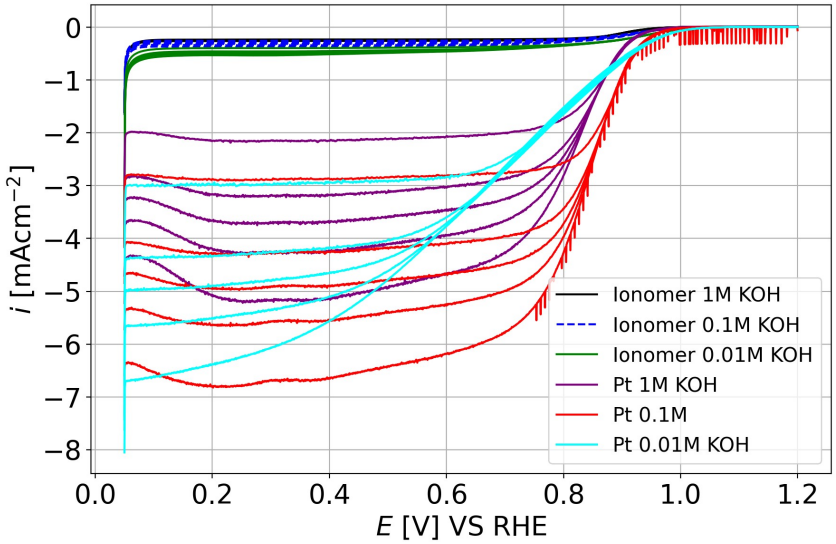

(a) LSVs for pure Pt and 43 µm ionomer thin films

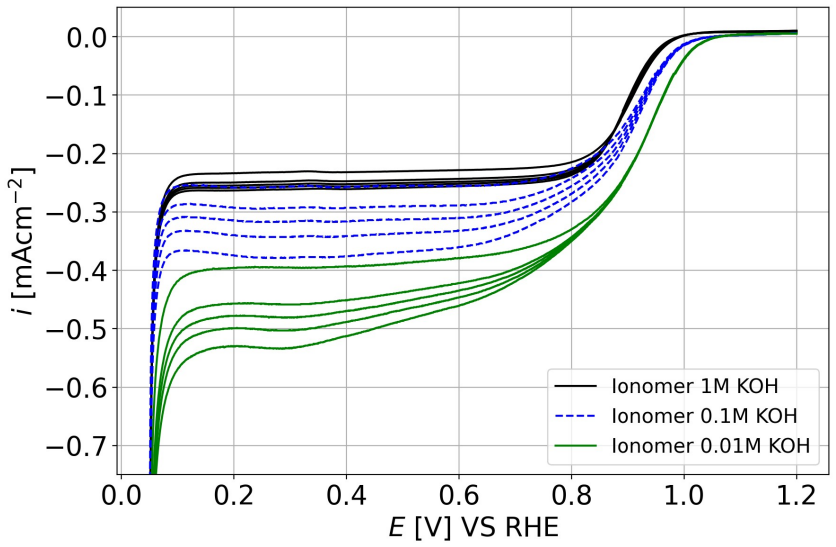

(b) Top section from (a). LSVs for 43 µm ionomer thin films.

Figure 4.6: LSVs at different rpms for pure Pt and 43 µm thick ionomer thin films in three different concentrations of KOH. The rpms are increasing as the current is decreasing. The LSVs are measured at a scan rate of 5 mV/s in the range between 0.05V to 1.2V vs. RHE.

Investigating the LSVs as a Tafel plot visualized the pH (concentration) dependence. The Tafel plot is illustrated in Figure 4.7. As indicated in the LSVs there were two distinct

regions, one for the ionomer and one for pure Pt. Pure Pt in 0.01M exhibited a deviation from the rest and crossed the slopes of pure Pt in 1M and 0.1M KOH in the kinetic/mixed diffusion region. Tafel slopes were not calculated due to not sufficient linearity in the plots.

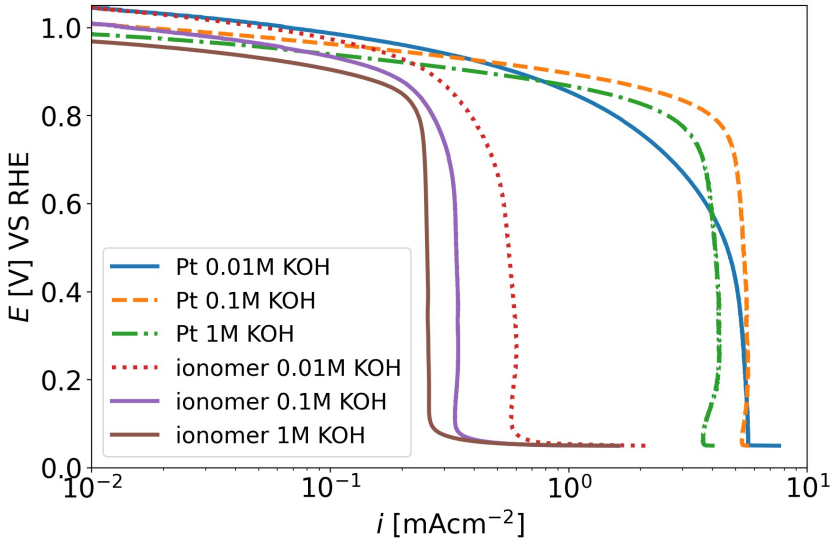

(a) Tafel plots of the ionomer thin film and the pure Pt.

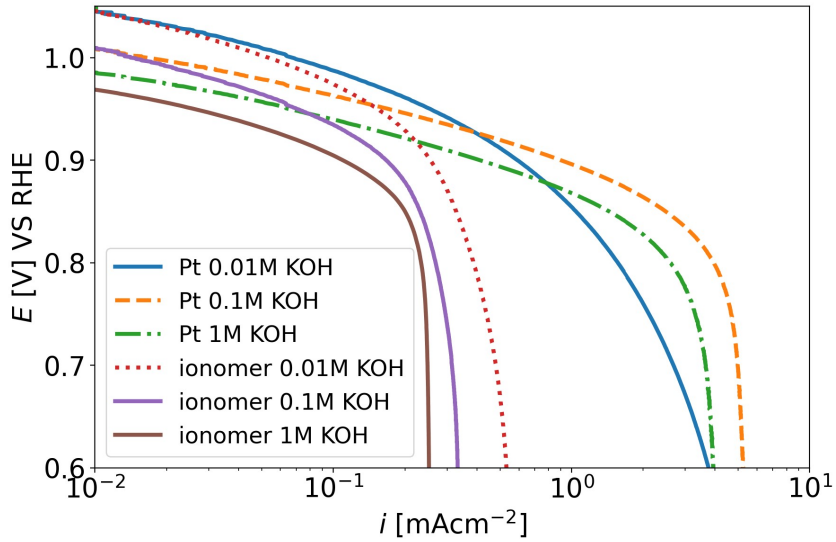

(b) Closer look at the kinetic controlled region from (a)

Figure 4.7: Tafel plots of the ionomer thin film and the pure Pt in different concentrations of KOH.

The Tafel plots provided an opportunity to further investigate the pH dependence by exploring the reaction order for OH^- (Ω_{OH^-}). By employing equations 2.12-2.16, a plot was constructed to determine the reaction order, which is given by the slope of the resulting curves. The resulting plot, shown in Figure 4.8, revealed that choice of potential has an impact on the reaction order. It is important to highlight that a relatively large deviation was observed in the regression line for Pt at 850 mV. The reaction orders at 950 mV are closer in value compared to the reaction orders at 850 mV.

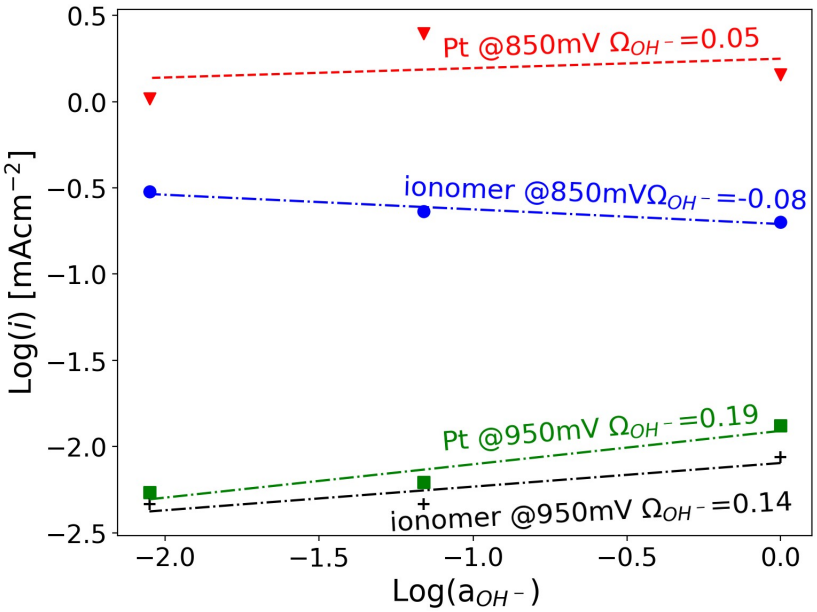

Figure 4.8: Plot indicating reaction order for OH^- as the slope of the linear regression, Ω_{OH^-}. In the figure, @ describes the potential the measurement is observed at.

4.4 Koutecky Levich study of different concentrations of KOH

The Koutecky Levich plots depicting the limiting current densities are presented in Figure 4.9. There were two distinct regions, one containing pure Pt slopes and the other ionomer thin films. At limiting current density, there was not a large variation of the slopes and intercepts for pure Pt. As seen in Figure 4.9(b), there was a slight increase in slope for increasing concentration of KOH. In addition, there was a decrease in intercept as the concentration increased for pure Pt. However, for ionomer thin film, an increase in intercept is related to an increase in concentration of KOH. The slope of the ionomer thin film in 0.1M KOH was twice as large as the other ionomer thin films. In addition, it had a low R^2-value which is given in Table D.1 in Appendix D.

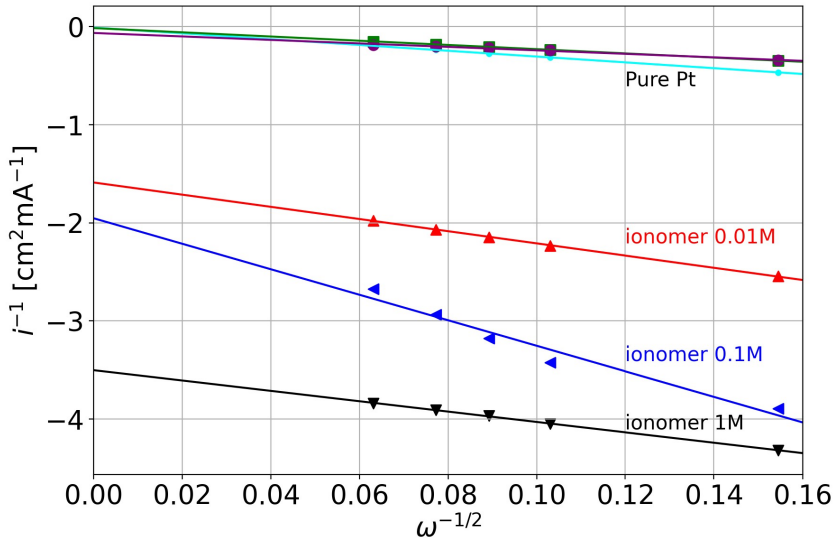

(a) Koutecky Levich diagram for ionomer thin films and pure Pt in different concentrations of KOH

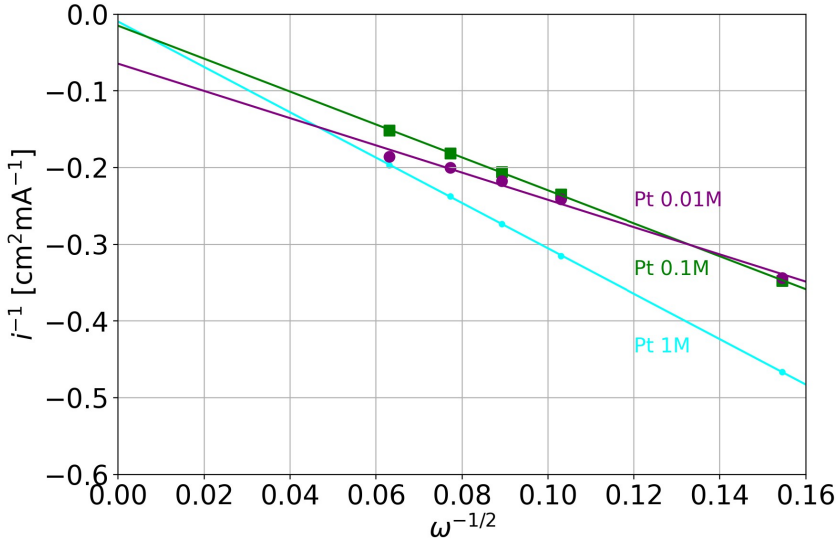

(b) Koutecky Levich diagram for pure Pt in different concentrations of KOH

Figure 4.9: Koutecky Levich diagram for 43 μm ionomer thin film and pure Pt in different concentrations of KOH at limiting current density.

The data obtained from the Koutecky Levich plots are shown in Table D.1 in Appendix D. The R^2-value for the linear fit for ionomer thin film in 0.1M KOH was low in addition to a high standard deviation. The calculated DC values for the thin films and $D^{2/3}C$ for pure Pt are given in Table 4.2. There was a small increase in DC and $D^{2/3}C$ as the KOH concentration decreased. However, the uncertainty of the measurements for ionomer thin films exceeds the difference between the concentrations. Therefore one can assume similar DC for ionomer thin films and a small increase for decreasing concentrations for pure Pt.

Table 4.2: The DC product for O_2 in 43 μm ionomer thin films in different concentrations of KOH saturated with O_2

Concentration of KOH [mol/dm^3]	$DC \cdot 10^9$ [mol/dm^3 · cm^2/s]
Ionomer thin film	
1	3.18 ± 120
0.1	5.71 ± 120
0.01	7.01 ± 120
Concentration of KOH [mol/dm^3]	$D^{2/3}C \cdot 10^6$ [mol/dm^3 · cm^2/s]
Pure Pt	
1	3.383 ± 0.0023
0.1	4.668± 0.0085
0.01	5.61 ± 0.068

Koutecky Levich plot obtained from the rising portion of the voltammogram at a potential of 0.850 V in different concentrations of KOH is illustrated in Figure 4.10. The extrapolated intercepts of the y-axis have increased in addition to the slopes decreasing compared to limiting current Koutecky Levich plot. The slope for pure Pt in 0.01M KOH was slightly positive due to higher current density for increasing rpm.

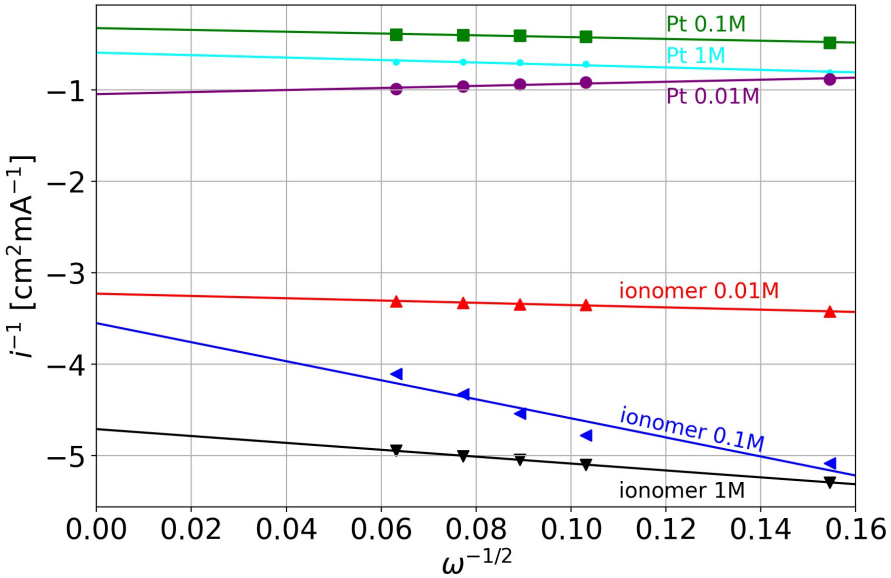

Figure 4.10: Koutecky Levich diagram for pure Pt and ionomer thin films in different concentrations of KOH at 0.850V.

Table D.2 in Appendix D shows the data obtained from the linear regression found in Figure 4.10. The standard deviation for ionomer thin film in 0.1M KOH was quite high in addition to obtaining a low slope.

The kinetic current densities in different concentrations of KOH are given in Table D.5.

The calculation of i_k for 0.825 V and 0.900 V is based on Koutecky Levich diagrams found in Appendix D. The kinetic currents are decreasing as the applied overpotential is increased. The highest kinetic current was observed for ionomer in 0.1M KOH. The overall observation was that the kinetic currents for the ionomer thin films are lower than the ones observed for pure Pt. The trends are illustrated in Figure 4.11. As seen in the figure, there is a large uncertainty for the ionomer at 0.9 V at 1M KOH.

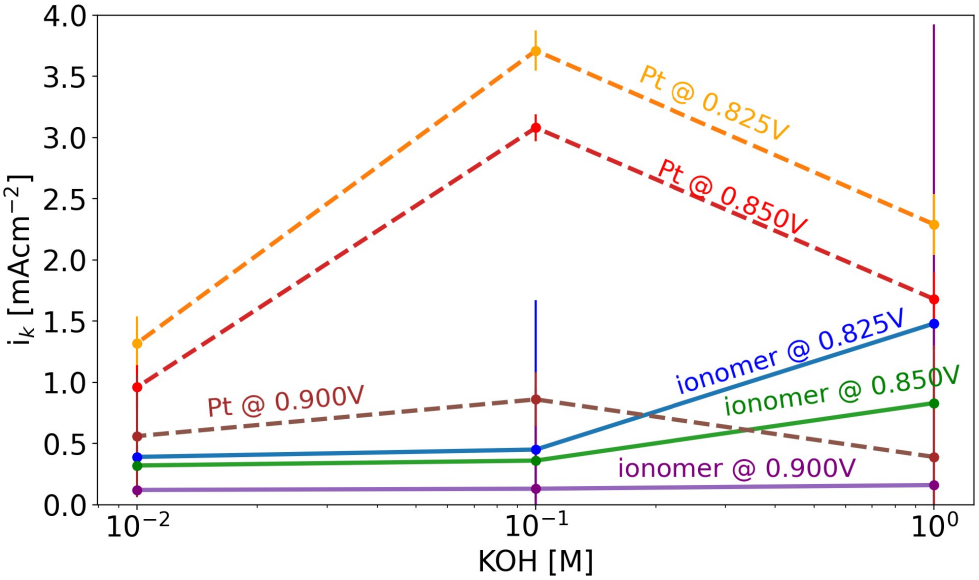

Figure 4.11: Kinetic currents for pure Pt and ionomer thin films in different concentrations of KOH. The measurements are recorded at different potentials given in the figure. @ indicates the potential the kinetic currents are recorded at.

4.5 Single cell testing

Single cell testing of different wt% of ionomer for the anode (10 wt% for CCM10% and 20 wt% for CCM20%) in different concentrations of electrolyte were conducted. In order to study how the ionomer content affects the performance of an AEMWE cell, tests with varying ionomer content were conducted at different electrolyte concentrations. Due to a lack of material, only two different values of ionomer content could be examined. Polarisation curves for the single cell tests are given in Figure 4.12. There are three distinct regions in the plot divided by the concentration of the electrolyte. There is not a large difference between the two different CCMs, but it is noteworthy that CCM10% was able to reach the highest current densities for 1.0M KOH and 1M KOH.

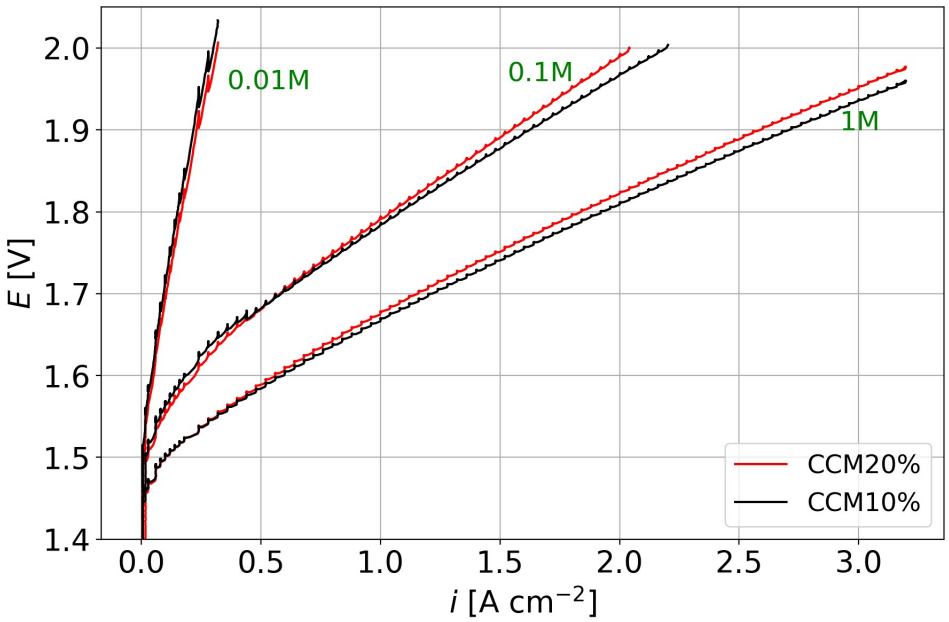

Figure 4.12: Polarisation curve for the two different CCMs in 1M, 0.1M and 0.01M KOH.

Figure 4.13 illustrates the durability of the cell for 18 hours. As seen in the figure, CCM10% started at a lower potential than CCM20%. However, the two curves crossed after approximately 12 hours leaving CCM10% to have a higher change in potential over the 18 hours compared to CCM20%.

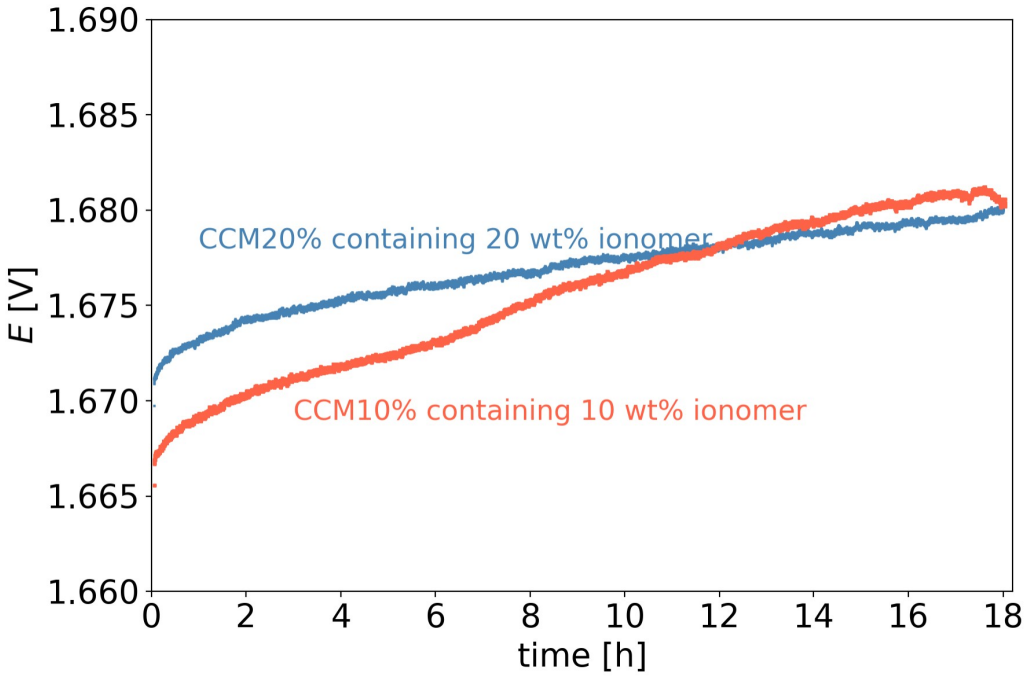

Figure 4.13: Durability for the two CCMs in 1M KOH.

Galvanostatic EIS conducted in three different concentrations for the two CCMs are given in Figure 4.14. The measurements given in the figure were conducted at 0.1 A/cm^2 to

be able to include the measurements conducted with 0.01M KOH electrolyte. The only variable that changed, in addition to the concentration of electrolyte, was the ionomer content in the anode catalyst layer. The cathode remained unchanged, in which the results focus on the anode. However, as seen in Table 4.3, it is difficult to assign the cathode and anode to specific time constants. Additional EIS data is given in Appendix F in Table F.1.

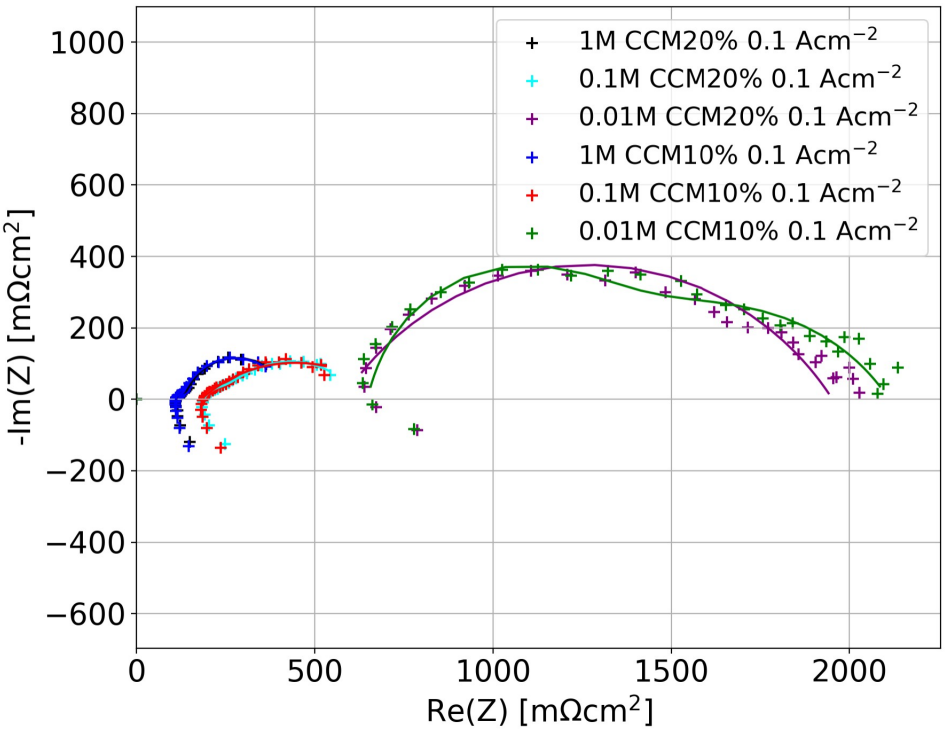

Figure 4.14: EIS for CCM20% and CCM10% recorded at 0.1A/cm^2 in 1M, 0.1M and 0.01M KOH.

Changing the electrolyte concentration from 1M to 0.1M results in an increase in ohmic resistance, R_s, of approximately 75 mΩcm^2 for both the CCMs. R_s for 0.01M KOH electrolyte was the highest for CCM10%. The charge transfer resistances increased as the concentration decreased with the largest difference between 0.1M and 0.01M. The CPE constants, Y_1 and Y_2 have a small decrease from 1M to 0.1M KOH. There is a further decrease of test in 0.01M KOH, which obtains the lowest Y_1 and Y_2.

Table 4.3: EIS data for the NiFeB anode from the fitting model. at 0.1 Acm^{-2}

KOH [M]	$\mathbf{R_s}$ [mΩcm^2]	$\mathbf{R_{CT1}}$ [mΩcm^2]	$\mathbf{R_{CT2}}$ [mΩcm^2]	$\mathbf{Y_1}$ [F s$^{(n-1)}$]	$\mathbf{Y_2}$ [F s$^{(n-1)}$]
CCM20%					
1	111.9	291.9	24.4	2.0	0.2
0.1	187.5	50.0	391.3	0.24	1.9
0.01	628.8	646.9	740.6	$1.9{\cdot}10^{-3}$	0.1
CCM10%					
1	111.3	17.5	296.3	0.2	1.9
0.1	187.5	48.8	369.4	0.1	1.7
0.01	645.6	618.1	846.9	$1.3{\cdot}10^{-3}$	0.1

Figure 4.15 illustrates Nyquist plots for the CCMs in 1M and 0.1M KOH electrolyte at 1.49 A/cm^2. It was not possible to obtain data at this current density for the test conducted in 0.01M KOH as the voltage exceeded the cut-off voltage of 2V. There is a shift in the real part of the impedance towards higher values for CCM20% compared to CCM10% in both concentrations of electrolyte. However, it is noticeably larger in 0.1M KOH compared to 1M KOH. In addition, the half circle for CCM20% is wider compared to CCM10% for 0.1M KOH.

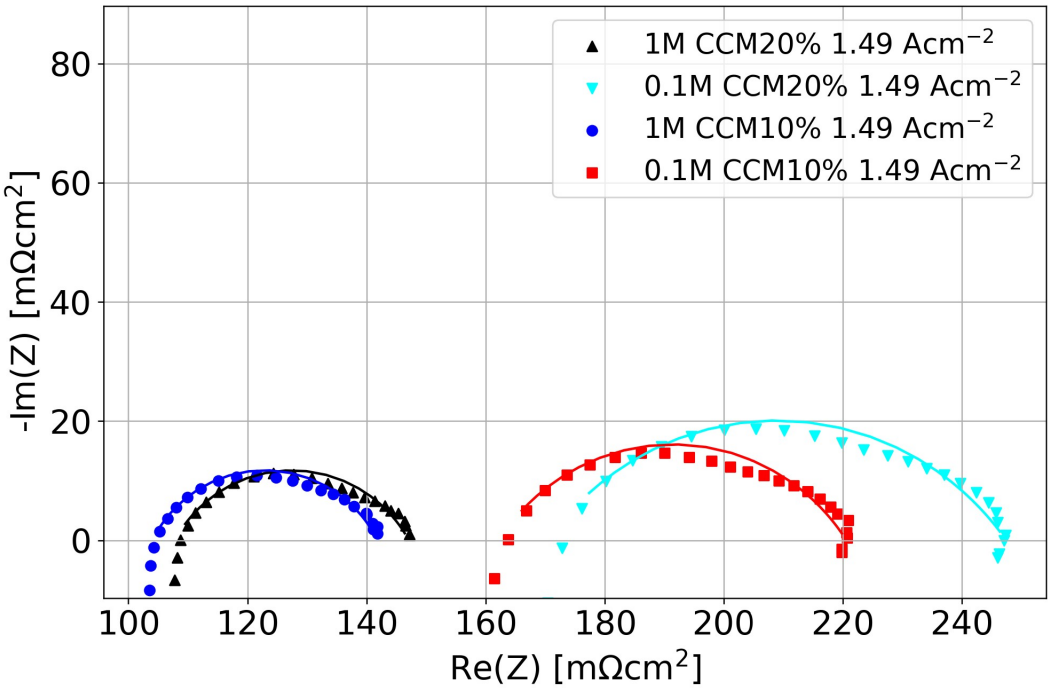

Figure 4.15: EIS for CCM20% and CCM10% recorded at 1.49A/cm^2 in 1M and 0.1M KOH.

The fitting data from Figure 4.15 is given below in Table 4.5. The charge transfer resistances for CCM20% are larger than CCM10% in 1M and 0.1M. The ohmic resistances are similar for the EIS measurements conducted at 0.1, but for 1M is it drastically lower for CCM10%. The CPEs, Y_1 and Y_2, are similar for the CCMs. A small decrease is observed

when changing the electrolyte from 1M to 0.1M KOH. There is a large decrease changing it to 0.01M KOH, which obtains the lowest CPEs.

Table 4.4: EIS data for the NiFeB anode from the fitting model recorded at 1.49 Acm^{-2}

KOH [M]	$\mathbf{R_s}$ [$m\Omega cm^2$]	$\mathbf{R_{CT1}}$ [$m\Omega cm^2$]	$\mathbf{R_{CT2}}$ [$m\Omega cm^2$]	$\mathbf{Y_1}$ [F $s^{(n-1)}$]	$\mathbf{Y_2}$ [F $s^{(n-1)}$]
CCM20%					
1	110.0	20.0	17.5	5.74	0.17
0.1	140.0	30.6	76.9	$-6.7 \cdot 10^{-6}$	0.6
CCM10%					
1	85.6	21.9	31.9	0.1	3.2
0.1	141.9	58.1	20.0	0.8	0.1

EIS was conducted before and after polarization curves were recorded. This is illustrated in Figure 4.16.

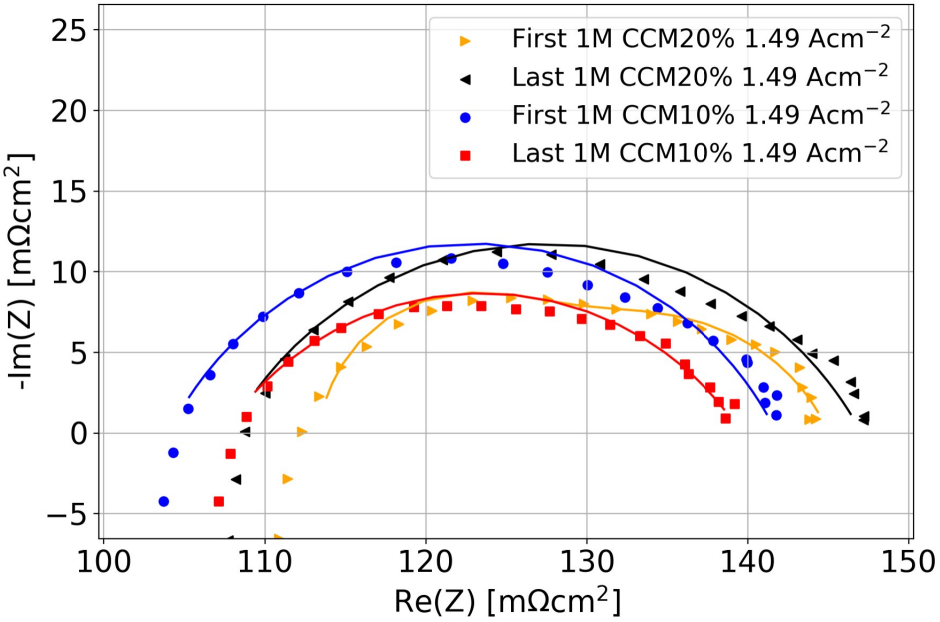

Figure 4.16: The first recorded EIS in 1M KOH and the last recorded EIS in 1M KOH before durability tests.

The fitting data obtained from the Nyquist plot (Figure 4.16) is given in Table 4.5. The ohmic resistance, R_s, increased for CCM20% after polarization. CCM10% had a different development, where R_s decreased. Noticeably, the ohmic resistances for CCM20% are over 20 $m\Omega cm^2$ larger than CCM10%. On the other hand, does CCM10% obtain larger charge transfer resistances. The CPE constants are lower for CCM10% compared to CCM20%.

Table 4.5: EIS data for the NiFeB anode from the fitting model recorded at 1.49 Acm^{-2}. The change from first to last is given in the table as Δ.

Sample	R_s [$m\Omega cm^2$]	R_{CT1} [$m\Omega cm^2$]	R_{CT2} [$m\Omega cm^2$]	Y_1 [F $s^{(n-1)}$]	Y_2 [F $s^{(n-1)}$]
CCM20% first	110.0	20.0	17.5	5.7	0.2
CCM20% last	113.1	13.1	19.4	0.2	6.5
Δ	3.1	-6.9	1.9	-5.5	6.3
CCM10% first	87.5	37.8	16.6	1.6	0.3
CCM10% last	85.6	21.9	31.9	0.1	3.2
Δ	-1.9	-15.9	15.3	-1.5	2.9

4.6 Mercury porosimetry

Mercury porosimetry of CCM20% and CCM10% is given in Figure 4.17. As seen in the figure there is not a large difference. CCM20% seems to achieve more pores in the larger pore size range of 100-5 µm. These are macro-pores and can be identified as secondary pores. CCM10% looks to obtain a slightly more porous structure in the micro-pore section at 0.5-0.01 µm which can indicate primary pores.

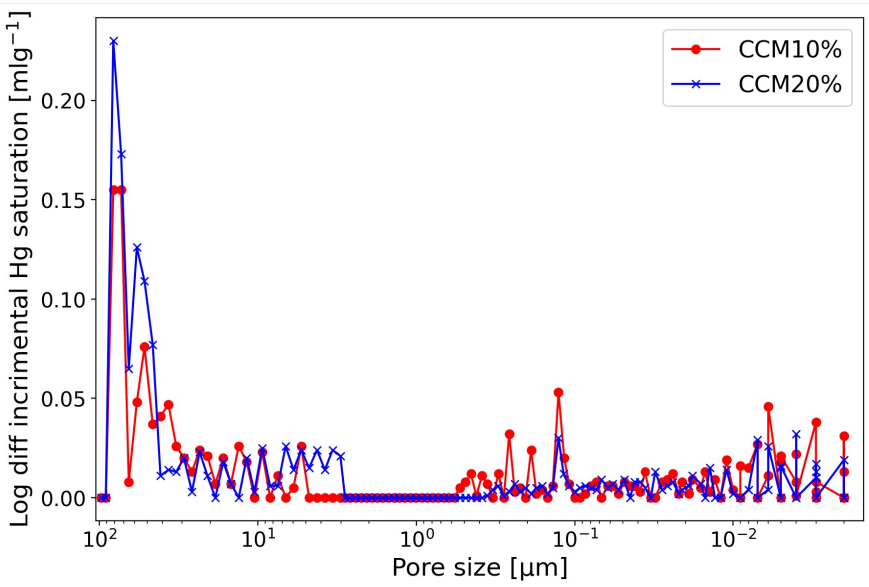

Figure 4.17: Mercury porosimetry illustrating the pore size distribution for CCM20% and CCM10%.

4.7 SEM

Figure 4.18 illustrates cross sections of CCM10% and CCM20%. Both of the CCMs illustrate porous catalyst layers. The AEM for CCM10% can be seen on the left side in Figure 4.18(a) and on the bottom for CCM20% in Figure 4.18(b). As seen in the figure, CCM10% appears to obtain a more porous structure inside the catalyst layer. CCM20% seems to have a slightly less porous structure where the double amount of

ionomer compared to CCM10%, is likely to make it more dense.

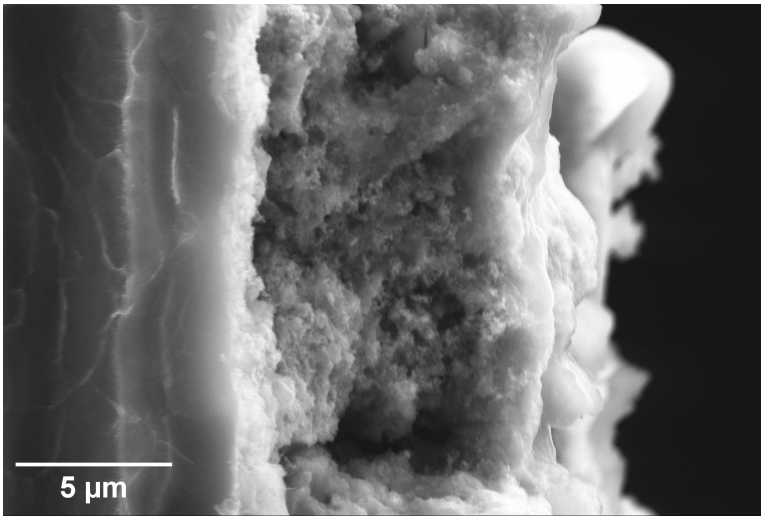

(a) CCM10%

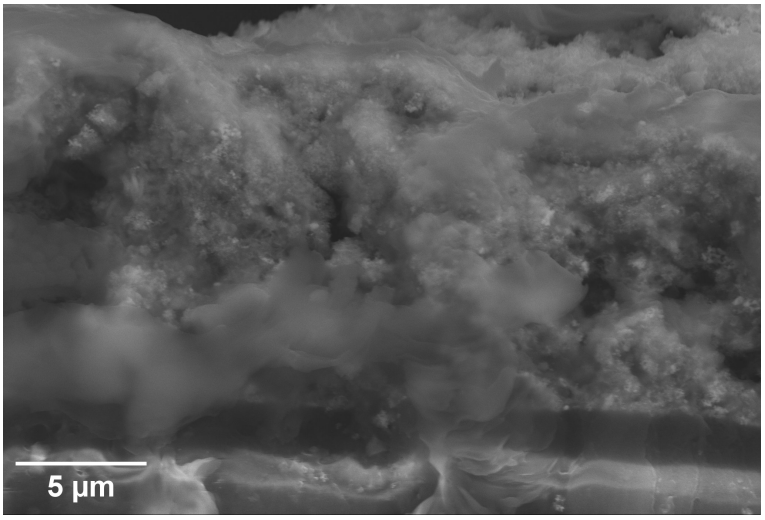

(b) CCM20%

Figure 4.18: SEM images of the cross section of CCM10% and CCM20%. CCM10% has the membrane on the left side and the catalyst layer is in the middle. CCM20% has the membrane at the bottom and the catalyst layer is in the middle.

5 Discussion

The ionomer decreases the rate of the oxygen reduction reaction due to the ionomer not efficiently conducting hydroxide ions. RDE measurements of ionomer thin films compared to bare Pt electrodes clearly indicate that the ionomer reduces the rate of the oxygen reduction reaction for oxygen. Ionomer thin films of varying thicknesses showed approximately 10 times smaller cathodic limiting current densities compared to pure Pt as seen in Figure 4.1. A decrease in limiting currents can originate from a decrease in mass transfer [64]. In addition, a general trend where an increase in thickness exhibited a further decrease in limiting currents. However, there were some deviations from that trend where for example 35 µm thick film obtained a larger limiting current compared to the thinner 33 µm ionomer thin film. This can be explained by the uncertainties related to the drop-casting method that was used for the preparation of the films. Drying effects can lead to an uneven distribution of ionomer on the surface. It is therefore difficult to control the film thickness accurately which might affect the precision of the voltammetric measurements [65].

Furthermore, a decrease in kinetic current for ionomer thin films is expected to be observed due to a decrease in the rate of the oxygen reduction reaction. The kinetic current density exposed a clear indication that the ionomer thin films have a lower rate of reaction compared to pure Pt as seen in Figure 4.5. This indicates that the reactions do not occur efficiently inside the ionomer. However, there is an interesting trend where an increase in the thickness of thin film gives an increase in kinetic current in 1M KOH. The kinetic current depends on the concentration of O_2 and OH^- in the phase that is in contact with the Pt surface [55]. The result suggests that a thicker ionomer film results in a larger concentration of O_2 and OH^- at the electrode compared to a thinner ionomer film. A possible explanation is that a thinner ionomer film will not contain as much OH^- as a thicker film and inhibit a fast reaction. A thicker film will also facilitate a slow reaction (hence low i_k), but will have a higher concentration of OH^- available inside the ionomer. If this is the case, a thicker amount of ionomer film should be able to exceed the kinetic current for pure Pt and indeed work as an electrolyte for AEMWE. However, additional measurements explained below show that this is probably not the case.

It is expected that a reason for the ionomer not working as a stand-alone electrolyte is due to low solubility and low diffusion coefficient for oxygen in the ionomer. However, by applying equation 2.22, one expects the DC product to be constant for the varying thicknesses. This is observed in Figure 4.3. The change of DC product will not be larger than the uncertainties, and can therefore be regarded as independent of the thickness of ionomer thin film. It is not directly comparable to the $D^{2/3}C$ obtained for pure Pt due to the exponent for the diffusion coefficient. However, it is likely that the constants, D and C, are close in value for Pt and the ionomer. The kinetics thereby play a larger role in how the ionomer compares to the pure Pt.

Performing RDE measurements of an ionomer thin film in different concentrations decreases the oxygen reduction reaction. The Tafel plots illustrated in Figure 4.7 show that the ORR that occurs in the thin film is affected by the concentration of KOH. If the ionomer itself would be sufficient to conduct OH^-, there should not be observed a difference by assuming the ORR inside the film is independent of the electrolyte (in theory only needs water). The LSVs seen in Figure 4.6, indicate that a decrease in concentration gives an increase in cathodic limiting currents, which is the same for pure Pt. There is also a shift in overpotential for the rising portion of the LSV. This suggests that the rate of the reduction reaction is faster for the lower concentration of KOH [55].

As seen in the LSVs (Figure 4.6), there is a slight difference in limiting current densities in different concentrations of KOH. The limiting current densities were expected to increase as the concentration was decreased. This is likely to be a result of the DC product decreasing as the concentration of KOH is increased. This result correlates with a study done by Park et al. [66]. However, this is not clearly indicated for Pt in 0.1M and 0.01M which have similar limiting currents, but the onset potential is shifted at 0.01M. In addition similar to the ionomer thin film, shifts in overpotentials for the mixed diffusion/kinetic diffusion region are observed for Pt as well. The same trend is observed for 1M and 0.1M, but Pt in 0.01M deviates and crosses them both in the mixed diffusion region.

If the ionomer would provide a sufficient concentration of hydroxide ions, the reaction rate of the ORR should be independent of the electrolyte concentration. However, the kinetic current obtained in different concentrations of KOH given in Figure 4.11, indicates as well that the ionomer reduces the reaction rate for oxygen. Compared to a similar study done by Lawson et al. on Nafion-coated Pt electrodes in phosphoric acid, the results are quite different [55]. Nafion is a perfluorosulfonic acid polymer used in PEMWE as a proton-conducting polymer which has a similar function to anion-conducting polymers for AEMWE [67]. Lawson et al. found that Nafion thin films on Pt electrodes decreased the diffusion coefficient, but increased the solubility of O_2 and oxygen reduction reaction. The Nafion thin films enhanced the kinetic currents by a factor of approximately 1.4-1.5 depending on the overpotential [55]. This indicates that Nafion can be utilized as an electrolyte for PEMWE and not be dependent on an acidic electrolyte feed to the electrolyzer. Therefore varying the concentration of KOH made it possible to confirm that the ionomer itself is not suited to be used as an electrolyte alone.

The reaction order for ionomer and pure Pt should be different in order to validate the premise that the ionomer decreases the oxygen reduction reaction. The reaction orders calculated for the ionomer and pure Pt indicate that in the mixed diffusion region at approximately 0.85 V, the ionomer is inferior to pure Pt. This relatively large difference in reaction order indicates that the oxygen reduction is slow and the ionomer is not enhancing the performance. At 0.95 V near the flatter kinetic diffusion region, the reactions order are more similar. This is expected due to 0.95 V being at the start of the kinetic diffusion

region. However, Pt is still showing slightly better reaction kinetics.

The observed decrease in the rate of oxygen reduction for the ionomer may be attributed to the low pH within the ionomer thin film itself. Previous studies indicated that ionomers containing quaternary ammonium groups do not exhibit a highly alkaline environment compared to alkaline electrolytes such as KOH. This is due to the quaternary ammonium groups not being as basic as alkali metal hydroxides [9]. If this is the case, a reason for the ionomers not being able to function as a standalone electrolyte is due to not providing an alkaline enough environment. Therefore the ionomer is not conducting OH^- efficiently without additional electrolyte.

Polarisation curves in varied concentrations of KOH from single cell tests is expected to show improved performance for a lower amount of ionomer due to a higher amount of active sites available. Single cell tests clearly indicate that the concentration of the electrolyte has a large effect on the performance. Polarisation curves seen in Figure 4.12 indicate that the CCM containing only 10% ionomer has slightly higher performance compared to the CCM containing 20% in 1M and 0.1M KOH. As stated in the theory section, the performance of the AEMWE is affected by the morphology of the catalyst layers due to the electrochemical reactions occurring at the active sites. A higher performance for a lower ionomer content suggests that the ionomer does not extend the active sites and facilitate OH^-, but hinders the active sites by reducing the reaction rate. This is contrary to the prevailing understanding in the literature which states that the ionomer's function is to improve hydroxide conductivity and extend the active sites. There are no observed differences for the CCMs in 0.01M KOH. This is probably due to the CCMs reaching 2V fast with only a small current applied.

Low electrolyte concentrations will lead to an increase in cell resistance due to lower ionic conductivity. This is in line with the polarisation curves obtained for different KOH concentrations, where the poorest performance was observed in 0.01M KOH. It is likely caused by a lack of OH^- to facilitate the electrochemical reactions. The charge transfer resistances were high for both CCMs in 0.01M KOH, indicating poor kinetics. Furthermore, the only EIS measurement able to run for the 0.01M KOH CCMs was at 0.1 Acm^{-2}. These observations are in line with the findings by Cossar et al. who studied the effect of alkaline concentration on AEMWE. The study found that a decrease in KOH solution resulted in a decrease in the electrolysis performance [68].

Since an increase in reaction rate at active sites is expected for a lower amount of ionomer, it is assumed that a lower resistance is obtained for lower ionomer content as well. EIS measurements conducted at 1.49 Acm^2 revealed some difference in resistance for CCM20% compared to CCM10%. CCM20% appears to have a higher ohmic resistance (R_s) at 1M KOH compared to CCM10%, even though they have the same electrolyte and cathode. A reason for this increase in ohmic resistance for CCM20% is probably caused by an increase in contact resistance between the anode PTL and the anode catalyst layer that sits on the

membrane. Hence the higher ionomer content disrupts the catalyst structure. The charge transfer resistances for the CCMs in 0.1M KOH vary in which of the time constants is the largest. This could be a result of a change in which of the anode and cathode obtain the largest resistance, but it is not possible to verify this. Overall, CCM20% exhibits a larger charge transfer resistance. This means that the higher amount of ionomer at the anode results in a higher charge transfer resistance for OER at the anode. This indicates that the ionomer to a large degree hinders active sites and impedes the OER instead of enhancing it.

Furthermore, the R_{CT2} in 1M KOH is higher for CCM10% even though the size of the half circle displayed by the Nyquist plot is of a similar diameter to CCM20%. A likely reason for why there is observed a larger difference in charge transfer resistances in 0.1M KOH compared to 1M KOH is that the higher concentration of KOH provides such a good supply of OH^- that a poor performing catalyst layer will not deviate compared to a better performing one. If the assumption is correct, this means that a higher concentration of electrolyte will compensate for low-performing catalyst layers. If the concentration is decreased, it will expose larger differences in catalyst layers such as a higher amount of ionomer decreases the rate of electrochemical reactions. The impact of ionomer content on the cell performance will therefore be more prominent at lower electrolyte concentrations. This can also indicate that the ionomer does not block the active sites, but hinders them with slow reaction rates.

The binding effect of the ionomer is assumed to improve the durability of the electrolyzer, especially for CCMs. Therefore one could assume a higher ionomer amount would disintegrate less than a lower amount of ionomer. However, the EIS measurements indicate that there is not a large difference between the two CCMs. The main difference obtained from the Nyquist plot, is that the ohmic resistance increased slightly from CCM20% and decreased slightly for CCM10%. Interestingly, durability tests were conducted which indicated an improvement in the durability for higher amounts of ionomer. The polarization curve conducted for 18 hours indicates a difference in durability when comparing the CCMs. CCM10% is able to perform at a lower potential than CCM20%. However, CCM10% obtains a steeper slope which indicates a faster degradation process. Even though the differences are relatively small, is it an interesting trend that is supported by the literature. Research conducted by Li et al. showed that ammonium-enriched anion exchange ionomers improve performance by improving durability due to the binding strength of the ionomer [69].

The binding effect can be traced to the catalytic structure and morphology. As seen from the mercury porosimetry data and the SEM images, it is difficult to differentiate the CCMs. There is a small difference where CCM20% obtains a slightly higher porosity for secondary pores, and CCM10% for primary pores. This trend is supported by literature where Suzuki et al. found that secondary pores were filled by ionomer [41]. However,

there have to be conducted more experimental evidence to confirm this trend.

The results obtained from the RDE measurements and single-cell tests suggest that the electrochemical reactions are efficiently taking place at active sites comprising KOH, catalyst, and a pore. This study does not provide evidence for the occurrence of these reactions at active sites represented by TPBs or where gas diffuses through the KOH electrolyte and reacts at two-phase boundaries between electrolyte and catalyst. For the ionomer, however, it is unlikely for these reactions to occur at active sites located within the ionomer, which consists only of catalyst and ionomer. This is due to the low reaction rate through the ionomer and the limited conduction of hydroxide ions.

Improved performance of AEMWE due to initiating activation processes in the start could be a result of getting rid of excess ionomer at active sites. "Activation" or "break in" is initiated at the start of a AEMWE testing protocol. Activation usually includes performing a stepwise polarisation curve until 2V is reached followed by circulating the electrolyte for $\approx$ 1 hour. A possible explanation could be that "break in" has to be completed to start gas development in the catalyst layers to get rid of excess ionomer that sits on the active sites. Hence it activates the active sites in the catalyst layers by getting rid of excess ionomer that slows the reactions. The ionomer is then distributed in the catalyst layer and could have an impact on strengthening it to some degree. Niaz et al. found that both the ohmic and non-ohmic resistances decreased after performing activation [70]. However, more experimental evidence is needed to confirm this theory.

There are a large number of factors that play a role in how the ionomer works in the catalyst layer. A larger focus on how the ionomer works and how it integrates with the catalyst layers is needed to improve AEMWE. Since the ionomer does not provide sufficient hydroxide ions for the electrochemical reactions to occur efficiently, a possible solution is to utilize another type of binder to stabilize the catalyst layers. Instead of using expensive ionomers, a possibility could be to exchange it with a cheaper porous binder that stabilizes the catalyst ink without hindering any active sites. Another more obvious possibility is to improve the ionomers by further studying the dispersion solvent, size of ionomer aggregates, and stability of the AEM. In addition, further study on how it disperses in the catalyst layer and reacts with active sites. It is a complex matter with a lot of different factors.

6 Conclusion

Ionomer thin films coated on platinum electrodes revealed that the ionomer reduces the rate of oxygen reduction reaction for oxygen. While the ionomer thin film demonstrated the ability to facilitate the diffusion of reactants and products, it did so at a low rate, which makes it ineffective as a stand-alone electrolyte in an AEMWE. Furthermore, it indicates that active sites inside the ionomer are not efficient. This was shown by low kinetic currents compared to pure platinum. Additional measurements of the ionomer thin film in varying concentrations of KOH did also reveal low kinetic currents and low reaction order. A likely reason for this is due to poor conductivity of hydroxide ions. The low conductivity of hydroxide ions of the ionomer compared to KOH may be due to the quaternary ammonium groups in the ionomer being less basic compared to alkali metal hydroxides such as KOH.

Furthermore, testing in a real AEMWE cell indicated that a lower amount of ionomer outperformed a higher amount of ionomer in terms of achieving higher current densities at lower potentials. This indicates that higher ionomer content reduces the rate of electrochemical reaction at active sites containing ionomer. Varying the concentration in the cell resulted in a large decrease in performance as the KOH concentration decreased. This decrease in performance is due to the ionomer not being able to conduct OH^- efficiently without additional alkaline electrolytes. Electrochemical impedance spectroscopy further demonstrated a slight increase in resistance for a higher amount of ionomer. Nonetheless, durability tests indicated that a higher amount of ionomer enhanced the durability of the cell due to the binding characteristics of the ionomer. In conclusion, the ionomer enables the diffusion of reactants and products, although at a relatively low rate. The electrochemical reactions occurs faster at active sites containing KOH compared to active sites containing ionomer. Furthermore, it exhibits limited conductivity for hydroxide ions, making it not fit to be used as a standalone electrolyte. However, the ionomer does serve as a binder that strengthens the catalyst layer and enhances durability.

7 Further work

First and foremost there are several improvements to the fabrication of ionomer thin films on the rotating disk electrodes. To enhance the understanding of the ionomer, a better coating technique to achieve higher reproducibility in addition to a larger variation of ionomer thicknesses could give a clearer indication of the limitation of the ionomer. To further enhance the understanding of the ionomer is to utilize other types of alkaline ionomers to get a broader specter of data.

For the single cell tests, would it be interesting to substitute the ionomer with a cheaper porous binder that does not block active sites. This will of course not eliminate the need for alkaline electrolytes being fed to the cell, but can offer a benefit in comparison to today's solution in terms of price and functionality of durability characteristics. If further research of the ionomer is to be conducted, an interesting approach is to investigate different solvents for it in addition to the sizing of the aggregates. There could be some configuration in terms of the solvents that could offer beneficial solubility which could see to increase the conductivity of hydroxide ions. Furthermore, providing a more basic ionomer could see it improving the conductivity of hydroxide ions.

Bibliography

[1] Naiying Du et al. "Anion-Exchange Membrane Water Electrolyzers". In: *Chemical Reviews* 122.13 (2022), pp. 11830–11895. DOI: 10.1021/acs.chemrev.1c00854. URL: https://doi.org/10.1021/acs.chemrev.1c00854.

[2] European Commission. *Renewable energy targets*. May 2023. URL: https://energy.ec.europa.eu/topics/renewable-energy/renewable-energy-directive-targets-and-rules/renewable-energy-targets_en.

[3] Ji Eun Park et al. "High-performance anion-exchange membrane water electrolysis". In: *Electrochimica Acta* 295 (2019), pp. 99–106. ISSN: 0013-4686. DOI: https://doi.org/10.1016/j.electacta.2018.10.143. URL: https://www.sciencedirect.com/science/article/pii/S0013468618323831.

[4] Patrick Fortin et al. "High-performance alkaline water electrolysis using Aemion™ anion exchange membranes". In: *Journal of Power Sources* 451 (Mar. 2020). ISSN: 03787753. DOI: 10.1016/j.jpowsour.2020.227814.

[5] Hamish Andrew Miller et al. "Green hydrogen from anion exchange membrane water electrolysis: a review of recent developments in critical materials and operating conditions". In: *Sustainable Energy Fuels* 4.5 (2020), pp. 2114–2133. DOI: 10.1039/C9SE01240K. URL: http://dx.doi.org/10.1039/C9SE01240K.

[6] Abdalla M Abdalla et al. "Hydrogen production, storage, transportation and key challenges with applications: A review". In: *Energy Conversion and Management* 165 (2018), pp. 602–627. ISSN: 0196-8904. DOI: https://doi.org/10.1016/j.enconman.2018.03.088. URL: https://www.sciencedirect.com/science/article/pii/S0196890418303170.

[7] John Ahlfield et al. "Anion Conducting Ionomers for Fuel Cells and Electrolyzers". In: *Journal of The Electrochemical Society* 164.14 (Dec. 2017), F1648–F1653. ISSN: 0013-4651. DOI: 10.1149/2.1341714jes. URL: https://iopscience.iop.org/article/10.1149/2.1341714jes.

[8] Susanne Koch et al. "The effect of ionomer content in catalyst layers in anion-exchange membrane water electrolyzers prepared with reinforced membranes (Aemion+™)". In: *Journal of Materials Chemistry A* 9.28 (July 2021), pp. 15744–15754. ISSN: 20507496. DOI: 10.1039/d1ta01861b.

[9] Dongguo Li et al. "Durability of anion exchange membrane water electrolyzers". In: *Energy Environ. Sci.* 14.6 (2021), pp. 3393–3419. DOI: 10.1039/D0EE04086J. URL: http://dx.doi.org/10.1039/D0EE04086J.

[10] Sebastian Sakshaug Angelsen. *Improved catalyst layer morphology for anion exchange membrane water electrolysis through optimization of the spray coating parameters*. Tech. rep. Trondheim: NTNU, Dec. 2022.

[11] Pierre Millet and Sergey Grigoriev. "Water Electrolysis Technologies". In: *Renewable Hydrogen Technologies: Production, Purification, Storage, Applications and Safety* (Jan. 2013), pp. 19–41. DOI: 10.1016/B978-0-444-56352-1.00002-7. URL: https://www.sciencedirect.com/science/article/pii/B9780444563521000027?via%3Dihub.

[12] S Shiva Kumar and V Himabindu. "Hydrogen production by PEM water electrolysis – A review". In: *Materials Science for Energy Technologies* 2.3 (2019), pp. 442–454. ISSN: 2589-2991. DOI: https://doi.org/10.1016/j.mset.2019.03.002. URL: https://www.sciencedirect.com/science/article/pii/S2589299119300035.

[13] Ester López-Fernández et al. *Recent advances in alkaline exchange membrane water electrolysis and electrode manufacturing*. Nov. 2021. DOI: 10.3390/molecules26216326. URL: https://pubmed.ncbi.nlm.nih.gov/34770735/.

[14] Fatemeh Razmjooei et al. "Increasing the performance of an anion-exchange membrane electrolyzer operating in pure water with a nickel-based microporous layer". In: *Joule* 5.7 (July 2021), pp. 1776–1799. ISSN: 2542-4351. DOI: 10.1016/J.JOULE.2021.05.006. URL: https://www.sciencedirect.com/science/article/pii/S2542435121002105.

[15] Alaa Y Faid and Svein Sunde. "Anion Exchange Membrane Water Electrolysis from Catalyst Design to the Membrane Electrode Assembly". In: *Energy Technology* 10.9 (2022), p. 2200506. DOI: https://doi.org/10.1002/ente.202200506. URL: https://onlinelibrary.wiley.com/doi/abs/10.1002/ente.202200506.

[16] S Shiva Kumar and Hankwon Lim. "An overview of water electrolysis technologies for green hydrogen production". In: *Energy Reports* 8 (2022), pp. 13793–13813. ISSN: 2352-4847. DOI: https://doi.org/10.1016/j.egyr.2022.10.127. URL: https://www.sciencedirect.com/science/article/pii/S2352484722020625.

[17] Yujing Guo et al. "Comparison between hydrogen production by alkaline water electrolysis and hydrogen production by PEM electrolysis". In: *IOP Conference Series: Earth and Environmental Science* 371.4 (Dec. 2019), p. 042022. ISSN: 1755-1307. DOI: 10.1088/1755-1315/371/4/042022. URL: https://iopscience.iop.org/article/10.1088/1755-1315/371/4/042022.

[18] Emanuele Taibi et al. *Green Hydrogen Cost Reduction: Scaling up Electrolysers to Meet the 1.5C Climate Goal*. Tech. rep. Abu Dhabi: International Renewable Energy Agency, 2020. URL: https://www.irena.org/-/media/Files/IRENA/Agency/Publication/2020/Dec/IRENA_Green_hydrogen_cost_2020.pdf.

[19] Paige Shirvanian et al. *Novel components in anion exchange membrane water electrolyzers (AEMWE's): Status, challenges and future needs. A mini review*. Nov. 2021. DOI: 10.1016/j.elecom.2021.107140.

[20] Markus Stähler et al. "Impact of porous transport layer compression on hydrogen permeation in PEM water electrolysis". In: *International Journal of Hydrogen Energy* 45.7 (2020), pp. 4008–4014. ISSN: 0360-3199. DOI: https://doi.org/10.1016/

j.ijhydene.2019.12.016. URL: https://www.sciencedirect.com/science/article/pii/S0360319919345161.

[21] Jing Peng et al. "Effect of CO2 absorption on ion and water mobility in an anion exchange membrane". In: *Journal of Power Sources* 380 (2018), pp. 64–75. ISSN: 0378-7753. DOI: https://doi.org/10.1016/j.jpowsour.2018.01.071. URL: https://www.sciencedirect.com/science/article/pii/S0378775318300715.

[22] Reza Abbasi et al. "A Roadmap to Low-Cost Hydrogen with Hydroxide Exchange Membrane Electrolyzers". In: *Advanced Materials* 31 (Mar. 2019), p. 1805876. DOI: 10.1002/adma.201805876. URL: https://www.researchgate.net/publication/332326371_A_Roadmap_to_Low-Cost_Hydrogen_with_Hydroxide_Exchange_Membrane_Electrolyzers.

[23] Jaromír Hnát et al. "Development and testing of a novel catalyst-coated membrane with platinum-free catalysts for alkaline water electrolysis". In: *International Journal of Hydrogen Energy* 44.33 (2019), pp. 17493–17504. ISSN: 0360-3199. DOI: https://doi.org/10.1016/j.ijhydene.2019.05.054. URL: https://www.sciencedirect.com/science/article/pii/S0360319919318853.

[24] Hiroshi Ito et al. "Investigations on electrode configurations for anion exchange membrane electrolysis". In: *Journal of Applied Electrochemistry* 48.3 (2018), pp. 305–316. ISSN: 1572-8838. DOI: 10.1007/s10800-018-1159-5. URL: https://doi.org/10.1007/s10800-018-1159-5.

[25] Gadi Rothenberg. *Catalysis : concepts and green applications*. eng. Weinheim: Wiley-VCH, 2008. ISBN: 9783527318247.

[26] C.H. Hamnett. *Electrochemistry*. 2nd. Weinheim: Wiley, 2007, pp. 339–355. ISBN: 9783527310692.

[27] Zhijie Chen et al. "Recent advances in transition metal-based electrocatalysts for alkaline hydrogen evolution". In: *J. Mater. Chem. A* 7.25 (2019), pp. 14971–15005. DOI: 10.1039/C9TA03220G. URL: http://dx.doi.org/10.1039/C9TA03220G.

[28] Yi Cheng and San Ping Jiang. "Advances in electrocatalysts for oxygen evolution reaction of water electrolysis-from metal oxides to carbon nanotubes". In: *Progress in Natural Science: Materials International* 25.6 (2015), pp. 545–553. ISSN: 1002-0071. DOI: https://doi.org/10.1016/j.pnsc.2015.11.008. URL: https://www.sciencedirect.com/science/article/pii/S1002007115001264.

[29] Alaa Y. Faid and Svein Sunde. "NiFeB anode catalyst for anion exchange membrane water electrolysis". In: *Materials Letters* 324 (Oct. 2022). ISSN: 18734979. DOI: 10.1016/j.matlet.2022.132738.

[30] Suraj Gupta et al. "Metal Boride-Based Catalysts for Electrochemical Water-Splitting: A Review". In: *Advanced Functional Materials* 30.1 (2020), p. 1906481. DOI: https://doi.org/10.1002/adfm.201906481. URL: https://onlinelibrary.wiley.com/doi/abs/10.1002/adfm.201906481.

[31] Bernard Bladergroen et al. “Overview of Membrane Electrode Assembly Preparation Methods for Solid Polymer Electrolyte Electrolyzer”. In: *Electrolysis*. Ed. by Vladimir Linkov and Janis Kleperis. Rijeka: IntechOpen, 2012. Chap. 3. DOI: 10.5772/52947. URL: https://doi.org/10.5772/52947.

[32] Rhodri Jervis et al. “The Importance of Using Alkaline Ionomer Binders for Screening Electrocatalysts in Alkaline Electrolyte”. In: *Journal of The Electrochemical Society* 164.14 (Nov. 2017), F1551. DOI: 10.1149/2.0441714jes. URL: https://dx.doi.org/10.1149/2.0441714jes.

[33] Michael K Bates et al. “Composite Ni/NiO-Cr2O3 Catalyst for Alkaline Hydrogen Evolution Reaction”. In: *The Journal of Physical Chemistry C* 119.10 (Mar. 2015), pp. 5467–5477. ISSN: 1932-7447. DOI: 10.1021/jp512311c. URL: https://doi.org/10.1021/jp512311c.

[34] Dongguo Li et al. “Phenyl Oxidation Impacts the Durability of Alkaline Membrane Water Electrolyzer”. In: *ACS Applied Materials & Interfaces* 11.10 (2019), pp. 9696–9701. DOI: 10.1021/acsami.9b00711. URL: https://doi.org/10.1021/acsami.9b00711.

[35] Immanuel Vincent, Andries Kruger, and Dmitri Bessarabov. “Development of efficient membrane electrode assembly for low cost hydrogen production by anion exchange membrane electrolysis”. In: *International Journal of Hydrogen Energy* 42.16 (2017), pp. 10752–10761. ISSN: 0360-3199. DOI: https://doi.org/10.1016/j.ijhydene.2017.03.069. URL: https://www.sciencedirect.com/science/article/pii/S036031991730993X.

[36] Jonghyun Hyun et al. “Tailoring catalyst layer structures for anion exchange membrane fuel cells by controlling the size of ionomer aggreates in dispersion”. In: *Chemical Engineering Journal* 427 (2022), p. 131737. ISSN: 1385-8947. DOI: https://doi.org/10.1016/j.cej.2021.131737. URL: https://www.sciencedirect.com/science/article/pii/S1385894721033180.

[37] Min Wang et al. “The Impact of Catalyst Ink Dispersing Methodology on Fuel Cell Performance Using In-situ X-ray Scattering”. In: *ACS Applied Energy Materials* 2 (Mar. 2019). DOI: 10.1021/acsaem.9b01037. URL: https://www.researchgate.net/publication/334718128_The_Impact_of_Catalyst_Ink_Dispersing_Methodology_on_Fuel_Cell_Performance_Using_In-situ_X-ray_Scattering.

[38] Hiroki Nara et al. “Impedance Analysis Counting Reaction Distribution on Degradation of Cathode Catalyst Layer in PEFCs”. In: *Journal of The Electrochemical Society* 158.9 (July 2011), B1184. DOI: 10.1149/1.3610988. URL: https://dx.doi.org/10.1149/1.3610988.

[39] Makoto Uchida et al. “Effects of Microstructure of Carbon Support in the Catalyst Layer on the Performance of Polymer-Electrolyte Fuel Cells”. In: *Journal of The Electrochemical Society* 143.7 (July 1996), p. 2245. DOI: 10.1149/1.1836988. URL: https://dx.doi.org/10.1149/1.1836988.

[40] Masahiro Watanabe et al. “New preparation method of a high performance gas diffusion electrode working at 100% utilization of catalyst clusters and analysis of the reaction layer”. In: *Journal of Electroanalytical Chemistry and Interfacial Electrochemistry* 197.1 (1986), pp. 195–208. ISSN: 0022-0728. DOI: https://doi.org/10.1016/0022-0728(86)80149-8. URL: https://www.sciencedirect.com/science/article/pii/0022072886801498.

[41] Takahiro Suzuki, Shinya Okada, and Shohji Tsushima. “Analysis of Ionomer Distribution and Pt/C Agglomerate Size in Catalyst Layers by Two-Stage Ion-Beam Processing”. In: *Journal of The Electrochemical Society* 167.12 (Aug. 2020), p. 124513. DOI: 10.1149/1945-7111/abad6a. URL: https://dx.doi.org/10.1149/1945-7111/abad6a.

[42] Min Wang et al. “Impact of Catalyst Ink Dispersing Methodology on Fuel Cell Performance Using in-Situ X-ray Scattering”. In: *ACS Applied Energy Materials* 2.9 (Sept. 2019), pp. 6417–6427. ISSN: 25740962. DOI: 10.1021/acsaem.9b01037.

[43] Shohei Suzuki et al. “Influence of CO2 dissolution into anion exchange membrane on fuel cell performance”. In: *Electrochimica Acta* 88 (2013), pp. 552–558. ISSN: 0013-4686. DOI: https://doi.org/10.1016/j.electacta.2012.10.105. URL: https://www.sciencedirect.com/science/article/pii/S0013468612017197.

[44] Jaromír Hnát et al. “Polymer anion-selective membrane for electrolytic water splitting: The impact of a liquid electrolyte composition on the process parameters and long-term stability”. In: *International Journal of Hydrogen Energy* 39.10 (2014), pp. 4779–4787. ISSN: 0360-3199. DOI: https://doi.org/10.1016/j.ijhydene.2014.01.086. URL: https://www.sciencedirect.com/science/article/pii/S0360319914001360.

[45] Lena Trotochaud et al. “Nickel–Iron Oxyhydroxide Oxygen-Evolution Electrocatalysts: The Role of Intentional and Incidental Iron Incorporation”. In: *Journal of the American Chemical Society* 136.18 (2014), pp. 6744–6753. DOI: 10.1021/ja502379c. URL: https://doi.org/10.1021/ja502379c.

[46] Javier Parrondo et al. “Degradation of anion exchange membranes used for hydrogen production by ultrapure water electrolysis”. In: *RSC Adv.* 4.19 (2014), pp. 9875–9879. DOI: 10.1039/C3RA46630B. URL: http://dx.doi.org/10.1039/C3RA46630B.

[47] Keith B. Oldham, Jan C. Myland, and A. M. (Alan Maxwell) Bond. *Electrochemical science and technology : fundamentals and applications*. John Wiley & Sons, 2011, p. 405. ISBN: 9780470710852.

[48] Gino Bontempelli, Nicolò Dossi, and Rosanna Toniolo. “Voltammetry — Polarography”. In: *Encyclopedia of Analytical Science (Third Edition)*. Ed. by Paul Worsfold et al. Third Edition. Oxford: Academic Press, 2019, pp. 218–229. ISBN: 978-0-08-101984-9. DOI: https://doi.org/10.1016/B978-0-12-409547-2.14326-4. URL: https://www.sciencedirect.com/science/article/pii/B9780124095472143264.

[49] Wenlong Chen et al. "Reconsidering the Benchmarking Evaluation of Catalytic Activity in Oxygen Reduction Reaction". In: *iScience* 23.10 (2020), p. 101532. ISSN: 2589-0042. DOI: https://doi.org/10.1016/j.isci.2020.101532. URL: https://www.sciencedirect.com/science/article/pii/S2589004220307240.

[50] Xiaoming Ge et al. "Oxygen Reduction in Alkaline Media: From Mechanisms to Recent Advances of Catalysts". In: *ACS Catalysis* 5.8 (2015), pp. 4643–4667. DOI: 10.1021/acscatal.5b00524. URL: https://doi.org/10.1021/acscatal.5b00524.

[51] Allen J. Bard and Larry R. Faulkner. *Electrochemical methods : fundamentals and applications*. 605 Third Avenue New York NY USA: John Wiley & sons Inc, 2000. ISBN: 0471043729.

[52] Wei Xing et al. "1 - Oxygen Solubility, Diffusion Coefficient, and Solution Viscosity". In: *Rotating Electrode Methods and Oxygen Reduction Electrocatalysts*. Ed. by Wei Xing, Geping Yin, and Jiujun Zhang. Amsterdam: Elsevier, 2014, pp. 1–31. ISBN: 978-0-444-63278-4. DOI: https://doi.org/10.1016/B978-0-444-63278-4.00001-X. URL: https://www.sciencedirect.com/science/article/pii/B978044463278400001X.

[53] Weiwei Cai et al. "2 - Electrode Kinetics of Electron-Transfer Reaction and Reactant Transport in Electrolyte Solution". In: *Rotating Electrode Methods and Oxygen Reduction Electrocatalysts*. Ed. by Wei Xing, Geping Yin, and Jiujun Zhang. Amsterdam: Elsevier, 2014, pp. 33–65. ISBN: 978-0-444-63278-4. DOI: https://doi.org/10.1016/B978-0-444-63278-4.00002-1. URL: https://www.sciencedirect.com/science/article/pii/B9780444632784000021.

[54] Chunyu Du et al. "5 - Rotating Disk Electrode Method". In: *Rotating Electrode Methods and Oxygen Reduction Electrocatalysts*. Ed. by Wei Xing, Geping Yin, and Jiujun Zhang. Amsterdam: Elsevier, 2014, pp. 171–198. ISBN: 978-0-444-63278-4. DOI: https://doi.org/10.1016/B978-0-444-63278-4.00005-7. URL: https://www.sciencedirect.com/science/article/pii/B9780444632784000057.

[55] Del R Lawson et al. "Oxygen Reduction at Nafion Film-Coated Platinum Electrodes: Transport and Kinetics". In: *Journal of The Electrochemical Society* 135.9 (Sept. 1988), p. 2247. DOI: 10.1149/1.2096247. URL: https://dx.doi.org/10.1149/1.2096247.

[56] Kazuma Shinozaki et al. "Oxygen Reduction Reaction Measurements on Platinum Electrocatalysts Utilizing Rotating Disk Electrode Technique: I. Impact of Impurities, Measurement Protocols and Applied Corrections". In: *Journal of The Electrochemical Society* 162.10 (July 2015), F1144. DOI: 10.1149/2.1071509jes. URL: https://dx.doi.org/10.1149/2.1071509jes.

[57] Ernesto Amores et al. "Development of an operation strategy for hydrogen production using solar PV energy based on fluid dynamic aspects". In: Open Engineering 7.1 (2017), pp. 141–152. DOI: doi:10.1515/eng-2017-0020. URL: https://doi.org/10.1515/eng-2017-0020.

[58] Alexandros Ch. Lazanas and Mamas I Prodromidis. "Electrochemical Impedance Spectroscopy: A Tutorial". In: *ACS Measurement Science Au* (Mar. 2023). DOI: 10.1021/acsmeasuresciau.2c00070. URL: https://doi.org/10.1021/acsmeasuresciau.2c00070.

[59] Qiucheng Xu et al. "Anion Exchange Membrane Water Electrolyzer: Electrode Design, Lab-Scaled Testing System and Performance Evaluation". In: *EnergyChem* 4.5 (2022), p. 100087. ISSN: 2589-7780. DOI: https://doi.org/10.1016/j.enchem.2022.100087. URL: https://www.sciencedirect.com/science/article/pii/S2589778022000197.

[60] Fatemeh Razmjooei et al. "Elucidating the Performance Limitations of Alkaline Electrolyte Membrane Electrolysis: Dominance of Anion Concentration in Membrane Electrode Assembly". In: *ChemElectroChem* 7 (June 2020), pp. 1–11. DOI: 10.1002/celc.202000605.

[61] "4. - Real-Space Surface Profiling Techniques". In: *Characterization of Amorphous and Crystalline Rough Surface: Principles and Applications*. Ed. by Yiping Zhao, Gwo-Ching Wang, and Toh-Ming Lu. Vol. 37. Experimental Methods in the Physical Sciences. Academic Press, 2001, pp. 63–82. DOI: https://doi.org/10.1016/S1079-4042(01)80059-X. URL: https://www.sciencedirect.com/science/article/pii/S107940420180059X.

[62] Jarle Hjelen. *Scanning elektron-mikroskopi*. nob. Trondheim, 1989. URL: https://www.nb.no/items/URN:NBN:no-nb_digibok_2013070305116?page=0.

[63] Dermot Brabazon. "Chapter 18 - Nanocharacterization Techniques for Dental Implant Development". In: *Emerging Nanotechnologies in Dentistry*. Ed. by Karthikeyan Subramani and Waqar Ahmed. Micro and Nano Technologies. Boston: William Andrew Publishing, 2012, pp. 307–331. ISBN: 978-1-4557-7862-1. DOI: https://doi.org/10.1016/B978-1-4557-7862-1.00018-3. URL: https://www.sciencedirect.com/science/article/pii/B9781455778621000183.

[64] Juan Wang et al. "Quantitative kinetic analysis on oxygen reduction reaction: A perspective". In: *Nano Materials Science* 3.3 (2021), pp. 313–318. ISSN: 2589-9651. DOI: https://doi.org/10.1016/j.nanoms.2021.03.006. URL: https://www.sciencedirect.com/science/article/pii/S2589965121000179.

[65] Archana Kaliyaraj Selva Kumar et al. "A mini-review: How reliable is the drop casting technique?" In: *Electrochemistry Communications* 121 (2020), p. 106867. ISSN: 1388-2481. DOI: https://doi.org/10.1016/j.elecom.2020.106867. URL: https://www.sciencedirect.com/science/article/pii/S1388248120302186.

[66] S M PARK et al. "Electrochemical reduction of oxygen at platinum electrodes in KOH solutions - Temperature and concentration effects". In: *Journal of the electrochemical society* 133.8 (Aug. 1986), pp. 1641–1649. ISSN: 0013-4651. DOI: 10.1149/1.2108982.

[67] Abu Zafar Al Munsur et al. “Nafion-Based Proton-Exchange Membranes Built on Cross-Linked Semi-Interpenetrating Polymer Networks between Poly(acrylic acid) and Poly(vinyl alcohol)”. In: *ACS Applied Materials & Interfaces* 13.24 (June 2021), pp. 28188–28200. ISSN: 1944-8244. DOI: 10.1021/acsami.1c05662. URL: https://doi.org/10.1021/acsami.1c05662.

[68] Emily Cossar et al. “The Performance of Nickel and Nickel-Iron Catalysts Evaluated As Anodes in Anion Exchange Membrane Water Electrolysis”. In: *Catalysts* 9.10 (2019). ISSN: 2073-4344. DOI: 10.3390/catal9100814. URL: https://www.mdpi.com/2073-4344/9/10/814.

[69] Dongguo Li et al. “Highly quaternized polystyrene ionomers for high performance anion exchange membrane water electrolysers”. In: *Nature Energy* 5.5 (2020), pp. 378–385. ISSN: 2058-7546. DOI: 10.1038/s41560-020-0577-x. URL: https://doi.org/10.1038/s41560-020-0577-x.

[70] Atif Niaz et al. “Tracing Resistances of Anion Exchange Membrane Water Electrolyzer during Long-term Stability Tests”. In: *Journal of Electrochemical Science and Technology* 12 (June 2021). DOI: 10.33961/jecst.2021.00094.

Appendix

A Linear sweeps of different thicknesses of ionomer in 1M KOH

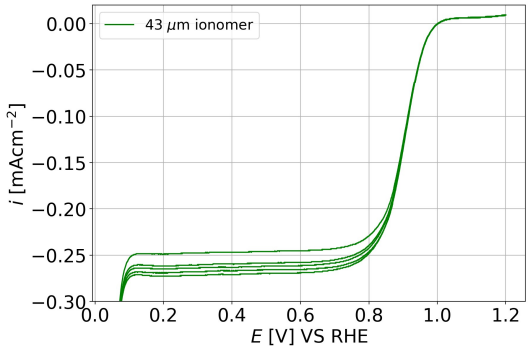

(a) 43 µm thick ionomer

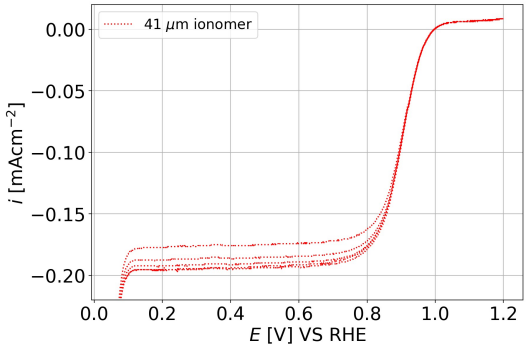

(b) 41 µm thick ionomer

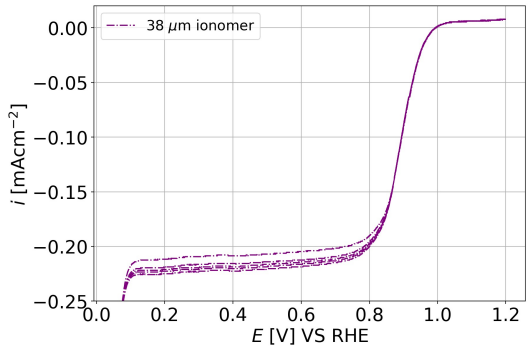

(c) 38 µm thick ionomer

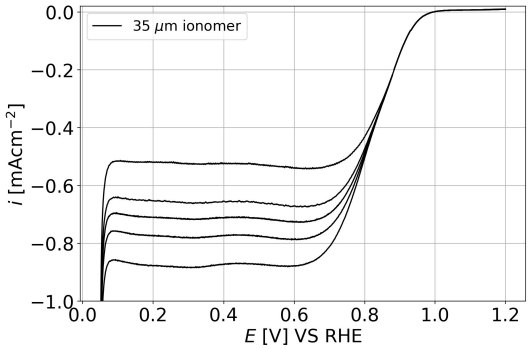

(d) 35 µm thick ionomer

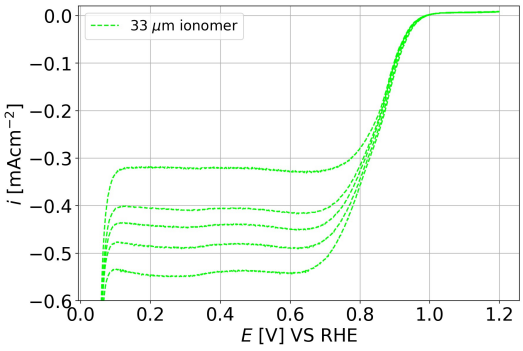

(e) 33 µm thick ionomer

Figure A.1: LSVs for different thicknesses of ionomer in 1M KOH

B Data from Koutecky Levich plots for different thicknesses of ionomer thin films in 1M KOH

Table B.1: Data obtained from the linear regression of the Koutecky Levich plot for pure Pt and different thicknesses of ionomer thin films on Pt electrode at limiting currents.

Thickness [μm]	**Intercept** [cm^2/mA]	**Slope** [cm^2/mA $\Omega^{0.5}$]	**R^2**	**standard deviation**
0	-0.01	-2.98	0.999	0.03
33	-1.04	-13.58	0.997	0.43
35	-0.66	-8.12	0.994	0.36
38	-4.30	-3.20	0.997	0.10
41	-4.71	-6.28	0.965	0.69
43	-3.46	-3.83	0.999	0.07

Table B.2: Data from the Koutecky Levich at 0.85 V plot given in Figure 4.4. The thickness of 0 indicates a pure Pt electrode.

Thickness [μm]	**Intercept** [cm^2/mA]	**Slope** [cm^2/mA $\Omega^{0.5}$]	**R^2**	**standard deviation**
0	-0.57	-1.54	0.921	0.26
33	-3.51	-7.99	0.921	1.35
35	-3.06	-1.28	0.966	0.14
38	-5.75	-1.68	0.967	0.18
41	-6.09	-5.47	0.889	1.12
43	-4.40	-3.27	0.973	0.31

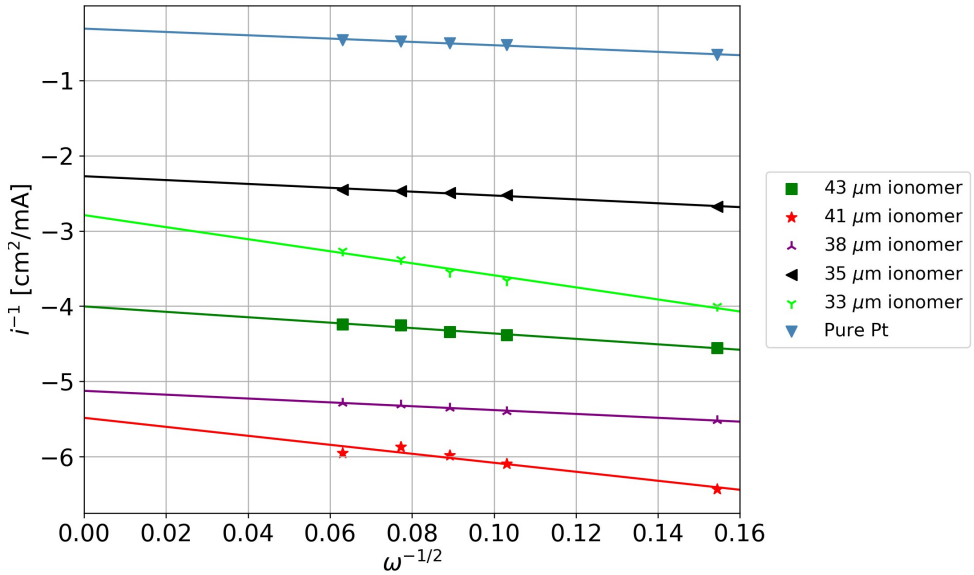

Figure B.1: Koutecky Levich plot for different thicknesses of ionomer in 1M KOH at 0.825 V

Table B.3: Data from the Koutecky Levich plot at 0.825 V given in Figure B.1. The thickness of 0 indicates a pure Pt electrode.

Thickness [μm]	**Intercept** [cm^2/mA]	**Slope** [cm^2/mA $\Omega^{0.5}$]	**r^2**	**standard deviation**
0	-0.31	-2.203	0.9859	0.1518
33	-2.79	-8.006	0.9810	0.64179
35	-2.2723	-2.5679	0.9794	0.21486
38	-5.125	-2.559	0.9906	0.1432
41	-5.48	-5.9752	0.91708	1.0372
43	-4.003	-3.597	0.9812	0.286

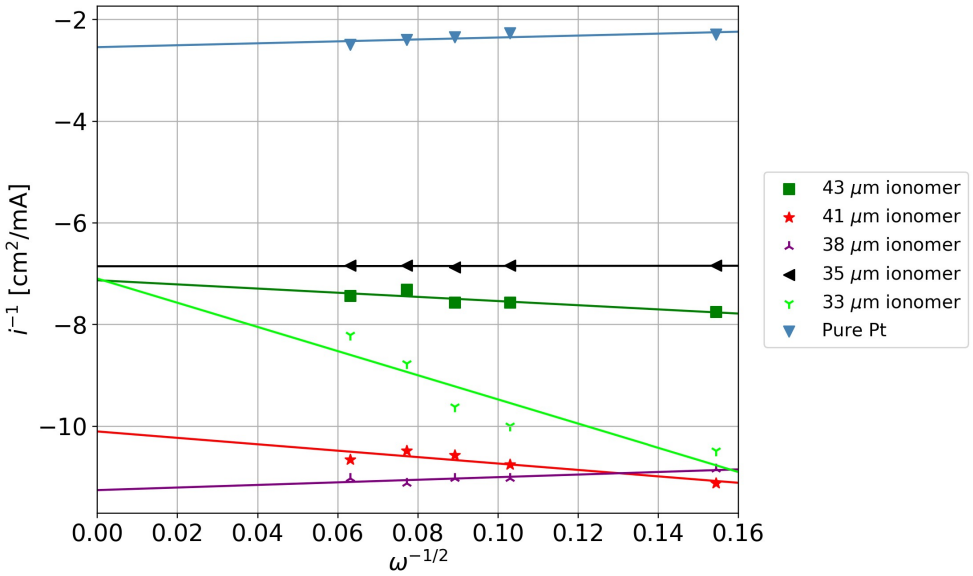

Figure B.2: Koutecky Levich plot for different thicknesses of ionomer in 1M KOH at 0.9 V

Table B.4: Data from the Koutecky Levich plot at 0.9 V given in Figure B.2. The thickness of 0 indicates a pure Pt electrode.

Thickness [μm]	**Intercept** [cm^2/mA]	**Slope** [cm^2/mA $\Omega^{0.5}$]	**r^2**	**standard deviation**
0	-2.55	1.90	0.553	0.99
33	-7.10	-23.78	0.81	6.51
35	-6.86	0.06	0.017	0.27
38	-11.26	2.55	0.757	0.83
41	-10.11	-6.31	0.807	1.79
43	-7.13	-4.09	0.75	1.35

Table B.5: Absolute kinetic current densities for ionomer thin films and pure Pt (0 μm)

Thickness [μm]	$\mathbf{i_k}$ [mA/cm^2]		
	0.825 [V]	**0.850** [V]	**0.900** [V]
43	1.84	1.06	0.27
41	1.29	0.73	0.19
38	1.21	0.69	0.14
35	0.62	0.42	0.14
33	0.57	0.40	0.16
0	3.22	1.75	0.39

Table B.6: The *DC* product for O_2 in ionomer thin films in 1 M KOH saturated with O_2

Thickness of thin film [μm]	**DC** $\cdot 10^9$ [mol/dm^3 $\cdot$ cm^2/s]
43	3.22
41	2.25
38	2.29
35	13.63
33	8.25

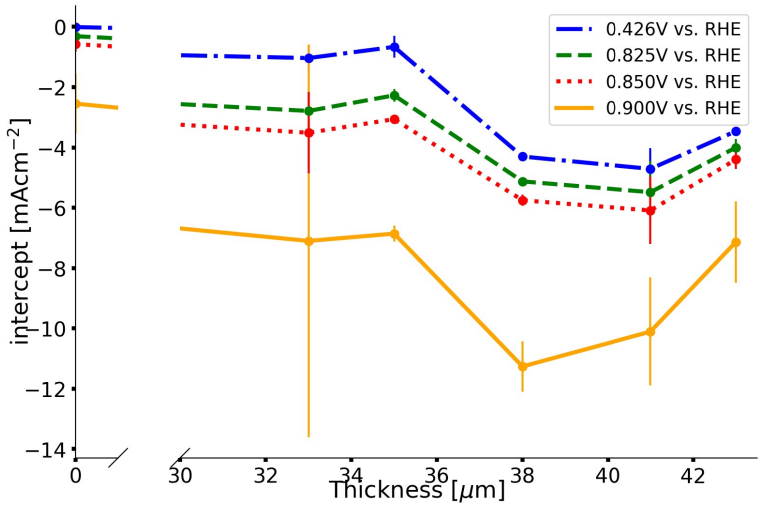

(a) Intercept vs. thickness

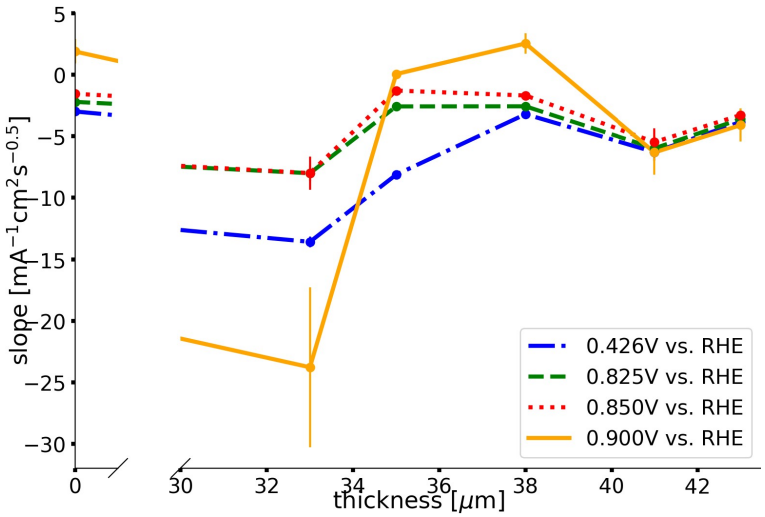

(b) slope vs thickness

Figure B.3: Illustration of the slopes and intercepts from the Koutecky Levich diagrams vs. thicknesses of ionomer thin films. Pure Pt can be viewed all the way to the left at thickness equal to 0.

C Cyclic voltammetry for Pt and ionomer thin films in different concentrations of KOH

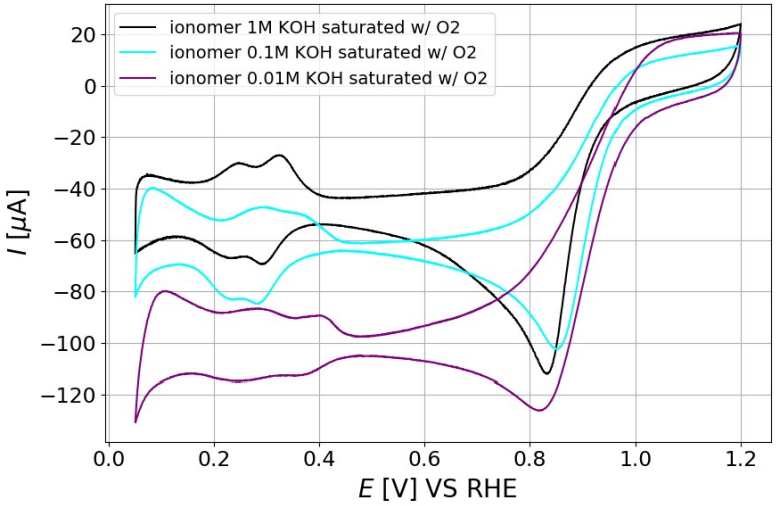

Figure C.1: Cyclic voltammetry of 43 µm thick ionomer film at various concentrations of KOH at a scan rate of 100 mV/s.

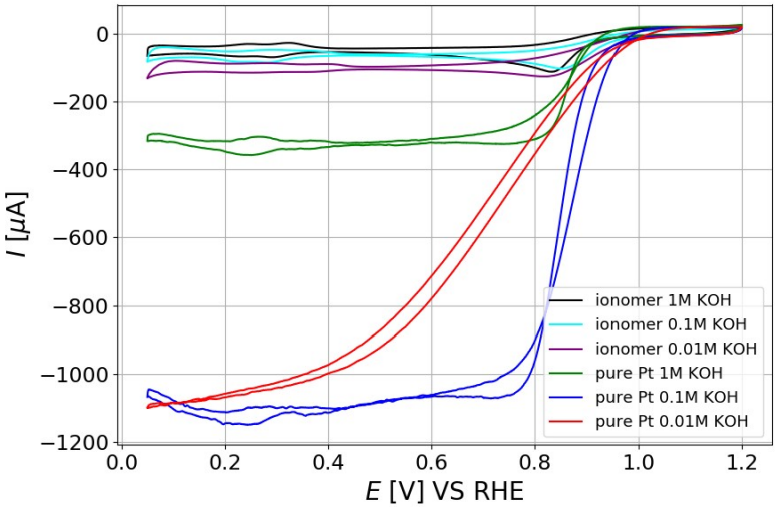

Figure C.2: Cyclic voltammetry of µm thick ionomer film and pure Pt at various concentrations of KOH at a scan rate of 100 mV/s

D Data from Koutecky Levich plots for ionomer thin film and pure Pt in various concentrations of KOH

Table D.1: Data obtained from Koutecky Levich plot of pure Pt and 43 μm ionomer thin films in different concentrations of KOH at the limiting currents.

KOH [mol/L]	**Intercept** [cm^2/mA]	**Slope** [cm^2/mA $\Omega^{0.5}$]	$\mathbf{R^2}$	**standard deviation**
Ionomer thin film				
1	-3.50	-5.29	0.999	0.07
0.1	-1.95	-13.01	0.958	1.57
0.01	-1.59	-6.21	0.999	0.07
Pure Pt				
1	-0.01	-2.96	0.999	0.01
0.1	-0.02	-2.15	0.999	0.02
0.01	-0.06	-1.78	0.989	0.11

Table D.2: Data obtained from Koutecky Levich plot of pure Pt and 43 μm ionomer thin films in different concentrations of KOH from the rising portion of the LSV at 0.85 V.

KOH [mol/L]	**Intercept** [cm^2/mA]	**Slope** [cm^2/mA $\Omega^{0.5}$]	$\mathbf{R^2}$	**standard deviation**
Ionomer thin film				
1	-4.71	-3.77	0.999	0.02
0.1	-3.55	-10.41	0.922	1.74
0.01	-3.22	-1.25	0.994	0.05
Pure Pt				
1	-0.59	-1.35	0.925	0.22
0.1	-0.33	-0.99	0.962	0.11
0.01	-1.05	1.13	0.931	0.18

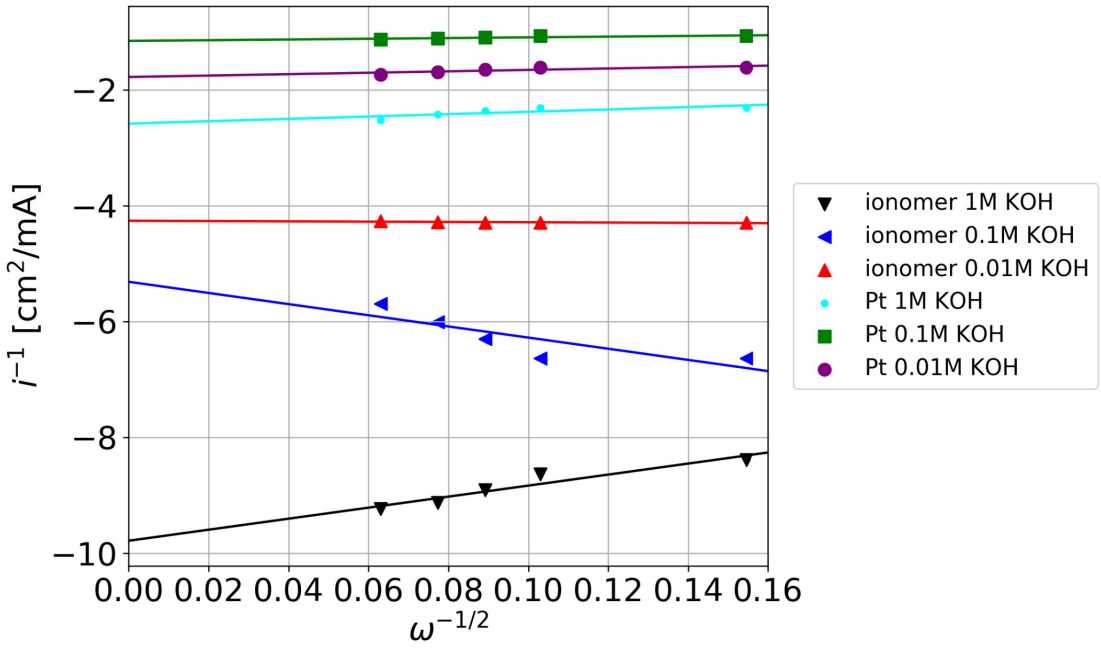

Figure D.1: Koutecky Levich diagram for 43 µm ionomer thin film and pure Pt in various concentrations of KOH at 0.9 V

Table D.3: Data obtained from Koutecky Levich plot of pure Pt and 43 μm ionomer thin films in different concentrations of KOH at 900mV.

KOH [mol/L]	**Intercept** [cm^2/mA]	**Slope** [cm^2/mA $\Omega^{0.5}$]	**r^2-value**	**standard deviation**
Ionomer thin film				
1	-9.78	9.51	0.911	1.72
0.1	-5.32	-9.63	0.687	3.75
0.01	-4.26	-0.26	0.50	0.15
Pure Pt				
1	-2.58	2.04	0.627	0.91
0.1	-1.16	0.61	0.72	0.22
0.01	-1.78	1.22	0.663	0.50

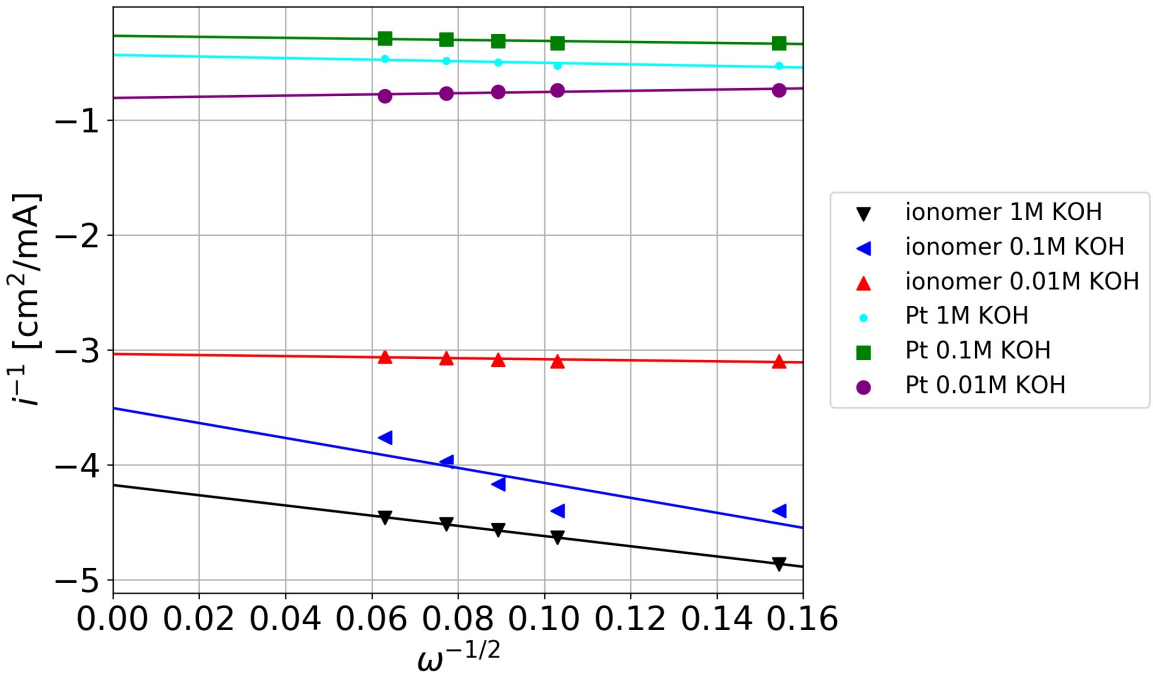

Figure D.2: Koutecky Levich diagram for 43 µm ionomer thin film and pure Pt in various concentrations of KOH at 0.825 V

Table D.4: Data obtained from Koutecky Levich plot of pure Pt and 43 μm ionomer thin films in different concentrations of KOH at 0.825 V.

KOH [mol/L]	**Intercept** [cm^2/mA]	**Slope** [cm^2/mA $\Omega^{0.5}$]	**r^2-value**	**standard deviation**
Ionomer thin film				
1	-4.177	-4.4374	0.9993	0.067
0.1	-3.507	-6.5085	0.6921	2.5062
0.01	-3.037	-0.4541	0.6841	0.1781
Pure Pt				
1	-0.4359	-0.681	0.7118	0.250
0.1	-0.269	-0.4438	0.7089	0.1642
0.01	-0.8100	0.5202	0.6490	0.2208

Table D.5: Absolute kinetic current calculated by utilizing equation 2.22 and 2.23

concentration of KOH [mol/dm^3]	$\mathbf{i_k}$ [mA/cm^2]		
	0.825 [V]	**0.850** [V]	**0.900** [V]
Ionomer thin film			
1	1.48	0.83	0.16
0.1	0.45	0.36	0.13
0.01	0.39	0.32	0.12
Pure Pt			
1	2.29	1.68	0.39
0.1	3.71	3.08	0.86
0.01	1.23	0.96	0.56

E Nickel voltammograms

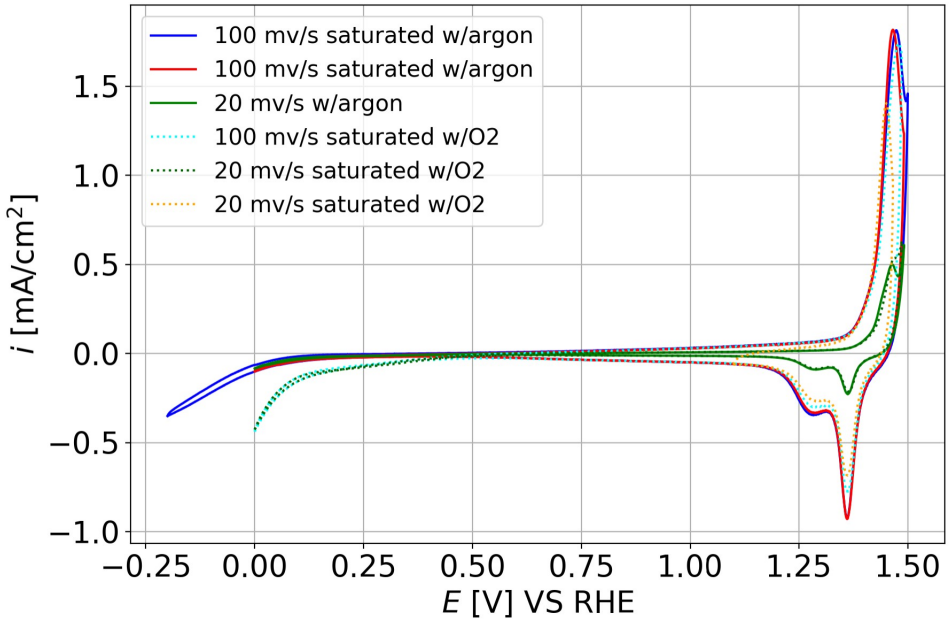

Figure E.1: CVs for Ni at different scan rates and saturated with either Ar gas or O_2 gas.

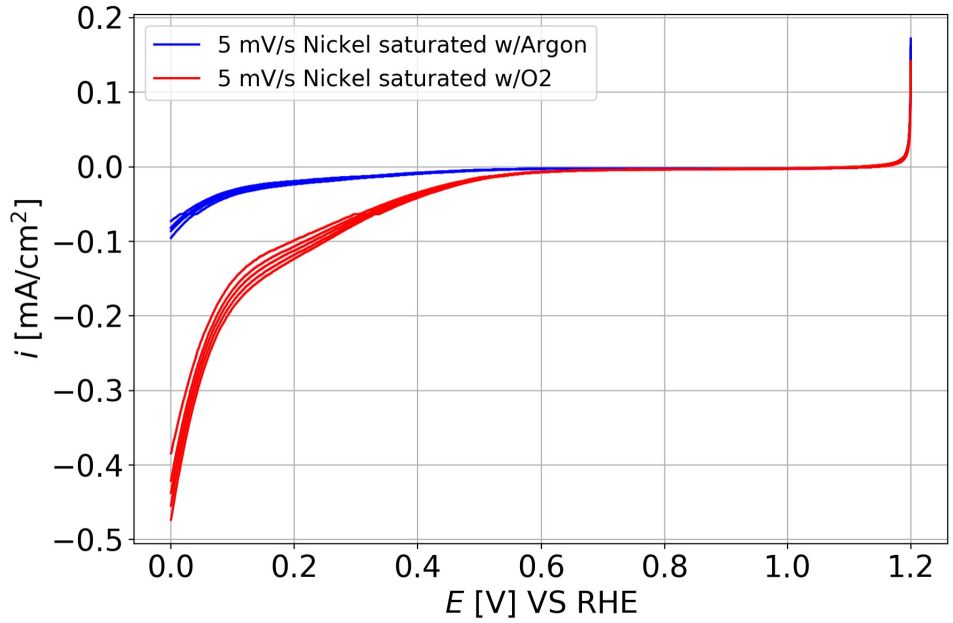

Figure E.2: LSVs for Ni at 5 mV/s saturated with Ar gas or O_2 gas.

F Electrochemical impedance spectroscopy measurements

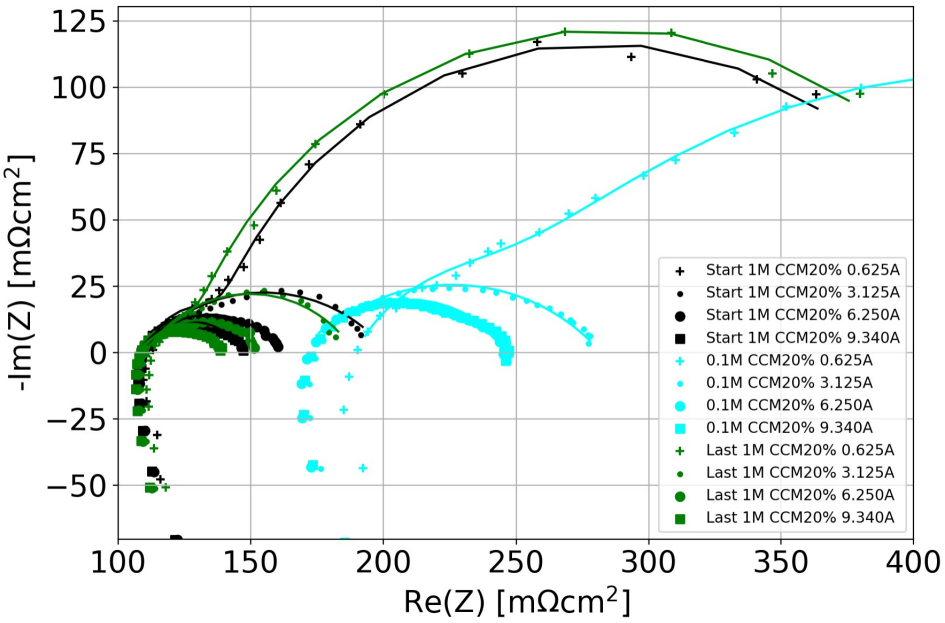

Figure F.1: EIS plots of 1M and 0.1M CCM20% at all the different applied currents

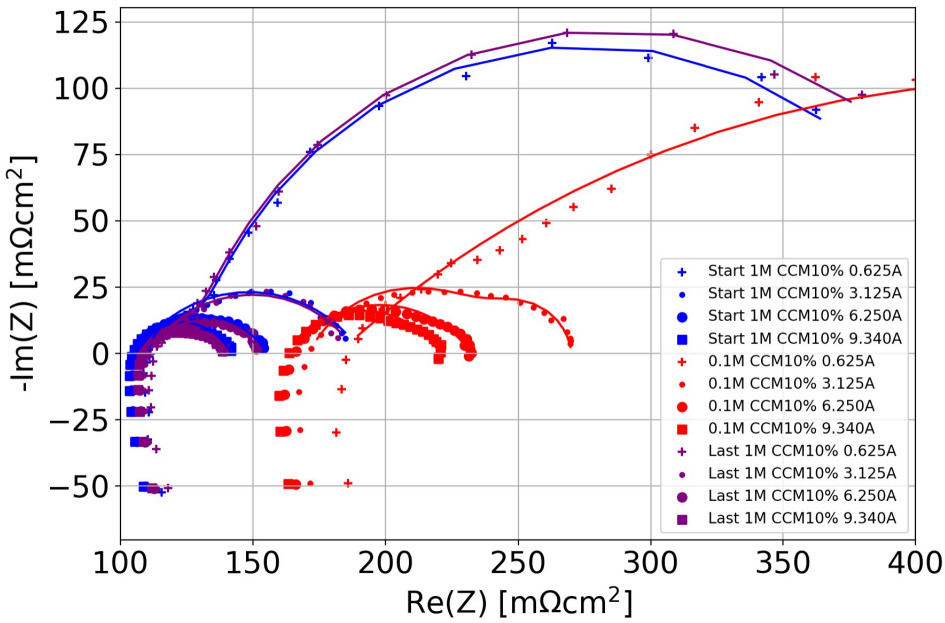

Figure F.2: EIS plots of 1M and 0.1M CCM10% at all the different applied currents

Table F.1: EIS fitting data obtained from EC-lab software tool for all the impedance measurements. The First 1M CCM measurements are given first and the Last 1M CCM measurements are given at the bottom for each of the CCMs.

KOH [M]	***I*** [A]	$\mathbf{R_s}$ [mΩ]	$\mathbf{R_{CT1}}$ [mΩ]	$\mathbf{R_{CT2}}$ [mΩ]	**Y1** [F $s^{(n-1)}$]	**Y2** [F $s^{(n-1)}$]	**n1**	**n1**
CCM20%								
1	9.34	17.6	3.2	2.8	5.74	0.17	0.754	1
1	6.25	17.2	8.6	3.94e-9	2.424	57.19e-6	0.623	0.999
1	3.125	17.3	8.8e9	14.9	57 873	3.78	0.340e-2	0.574
1	0.625	17.9	46.7	3.9	2.028	0.203	0.855	0.960
0.1	9.34	22.4	4.9	12.3	-6.696e-6	0.626	31.36e-6	0.612
0.1	6.25	27.1	12.3	0.964e-6	0.672	91.67e-9	0.612	1
0.1	3.125	0.249e-3	18.0	27.17	1.196	15.54e-6	0.544	0
0.1	0.625	30.3	8.0	62.6	0.237	1.907	0.753	0.623
0.01	0.625	100.6	103.5	118.5	1.908e-3	0.134	0.901	0.626
1	9.34	18.1	2.1	3.1	0.221	6.51	0.984	0.738
1	6.25	18.2	2.0	5.2	0.199	4.384	1	0.737
1	3.125	18.1	0.714e-12	13.7	28.6e-39	3.881	0.503	0.603
1	0.625	16.1	32.1	798.4	2.078	40.75	0.938	0.798
CCM10%								
1	9.34	14.0	6.05	2.65	1.618	0.327	0.708	0.054
1	6.25	0.32	8.1	16.4	2.236	6.287e-3	0.658	29.56e-12
1	3.125	16.97	3.754e-3	13.6	-8783	2,932	1	0.635
1	0.625	17.8	2.8	47.4	0.185	1.911	1	0.844
0.1	9.34	22.7	9.3	3.2	0.782	0.093	0.641	15-03e-9
0.1	6.25	26.2	11.0	1.554e-6	0.82	0.093	0.624	0.429
0.1	3.125	27.4	4.0	11.9	2.359	0.349	0.997	0.715
0.1	0.625	30.0	7.8	59.1	0.131	1.661	0.832	0.666
0.01	0.625	103.3	98.9	135.5	1.257e-3	0.123	0.942	0.631
1	9.34	13.7	3.5	5.1	0.145	3.15	2.059e-3	0.652
1	6.25	4.97	7.3	12.4	3.418	0.598	0.633	0.173
1	3.125	17.4	12.6	0.25	3.289	0.492	0.653	0.333
1	0.625	18.2	2.1	50.8	0.328	1.877	0.957	0.832

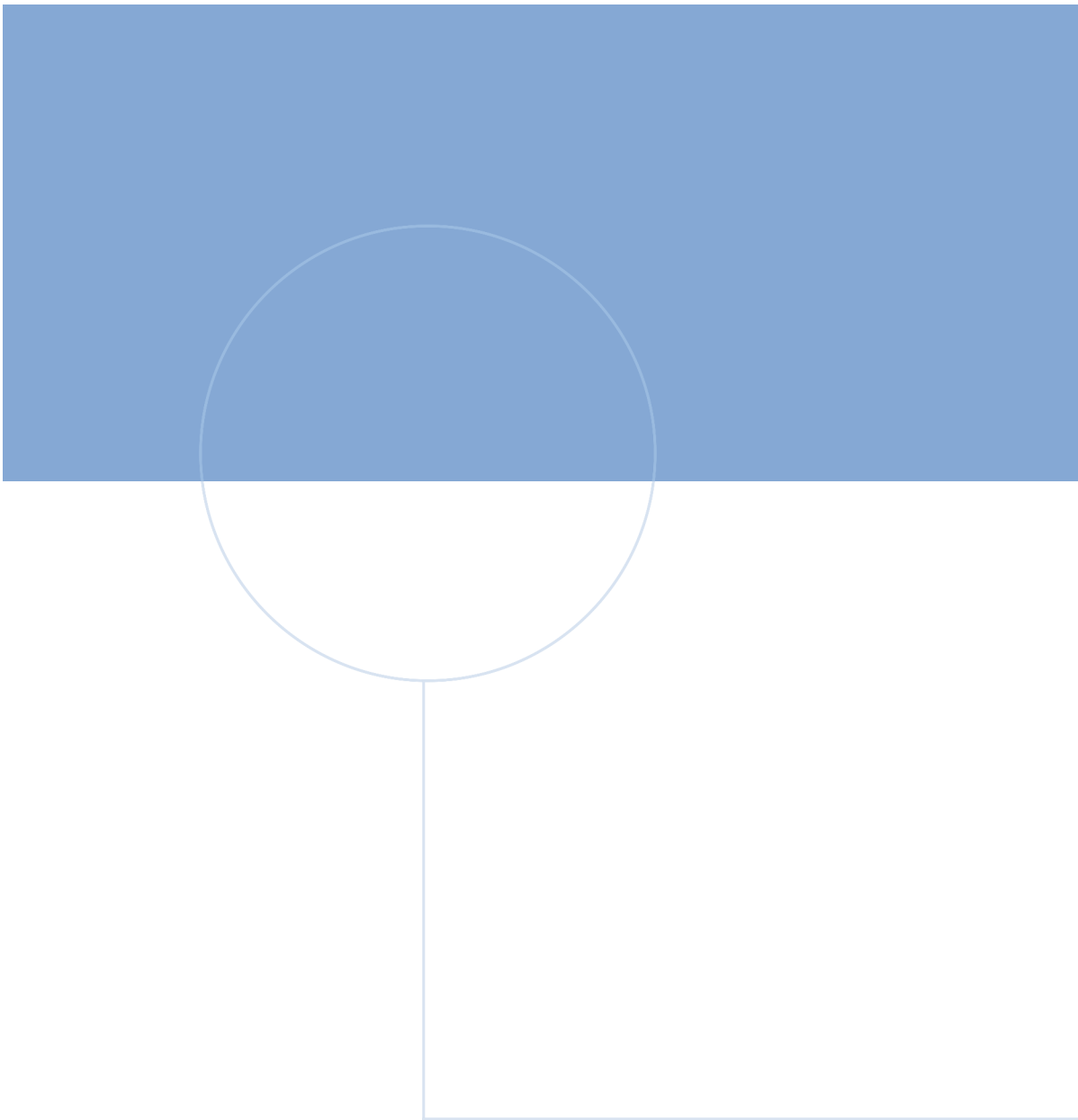

NTNU

Norwegian University of
Science and Technology